



University of Kentucky
UKnowledge

Theses and Dissertations--Chemical and
Materials Engineering

Chemical and Materials Engineering

2012

NANOPARTICLE ADDITIVES FOR MULTIPHASE SYSTEMS: SYNTHESIS, FORMULATION AND CHARACTERIZATION

Vinod Kanniah

University of Kentucky, vinodkanniah@gmail.com

[Right click to open a feedback form in a new tab to let us know how this document benefits you.](#)

Recommended Citation

Kanniah, Vinod, "NANOPARTICLE ADDITIVES FOR MULTIPHASE SYSTEMS: SYNTHESIS, FORMULATION AND CHARACTERIZATION" (2012). *Theses and Dissertations--Chemical and Materials Engineering*. 8. https://uknowledge.uky.edu/cme_etds/8

This Doctoral Dissertation is brought to you for free and open access by the Chemical and Materials Engineering at UKnowledge. It has been accepted for inclusion in Theses and Dissertations--Chemical and Materials Engineering by an authorized administrator of UKnowledge. For more information, please contact UKnowledge@lsv.uky.edu.

STUDENT AGREEMENT:

I represent that my thesis or dissertation and abstract are my original work. Proper attribution has been given to all outside sources. I understand that I am solely responsible for obtaining any needed copyright permissions. I have obtained and attached hereto needed written permission statements(s) from the owner(s) of each third-party copyrighted matter to be included in my work, allowing electronic distribution (if such use is not permitted by the fair use doctrine).

I hereby grant to The University of Kentucky and its agents the non-exclusive license to archive and make accessible my work in whole or in part in all forms of media, now or hereafter known. I agree that the document mentioned above may be made available immediately for worldwide access unless a preapproved embargo applies.

I retain all other ownership rights to the copyright of my work. I also retain the right to use in future works (such as articles or books) all or part of my work. I understand that I am free to register the copyright to my work.

REVIEW, APPROVAL AND ACCEPTANCE

The document mentioned above has been reviewed and accepted by the student's advisor, on behalf of the advisory committee, and by the Director of Graduate Studies (DGS), on behalf of the program; we verify that this is the final, approved version of the student's dissertation including all changes required by the advisory committee. The undersigned agree to abide by the statements above.

Vinod Kanniah, Student

Dr. Eric A. Grulke, Major Professor

Dr. Stephen E. Rankin, Director of Graduate Studies

NANOPARTICLE ADDITIVES FOR MULTIPHASE SYSTEMS:
SYNTHESIS, FORMULATION AND CHARACTERIZATION

DISSERTATION

A dissertation submitted in partial fulfillment of the
requirements for the degree of Doctoral of Philosophy in the
College of Engineering
at the University of Kentucky

By
Vinod Kanniah

Lexington, Kentucky

Director: Dr. Eric A. Grulke, Professor of Chemical Engineering

Lexington, Kentucky

2012

Copyright © Vinod Kanniah 2012

ABSTRACT OF DISSERTATION

NANOPARTICLE ADDITIVES FOR MULTIPHASE SYSTEMS: SYNTHESIS, FORMULATION AND CHARACTERIZATION

Study on nanoparticle additives in multiphase systems (liquid, polymer) are of immense interest in developing new product applications. Critical challenges for nanoparticle additives include their synthesis, formulation and characterization. These challenges are addressed in three application areas: nanofluids for engine lubrication, ultrathin nanocomposites for optical devices, and nanoparticle size distribution characterization.

Nanoparticle additives in oligomer mixtures can be used to develop extended temperature range motor oils. A model system includes poly(α -olefin) based oligomers with a modest fraction of poly(dimethylsiloxane) oligomers along with graphite as nanoparticle additive. Partition coefficients of each oligomer are determined since the oligomer mixture phase separated at temperatures less than $-15\text{ }^{\circ}\text{C}$. Also, the surface of graphite additive is quantitatively analyzed and modified via silanization for each oligomer. Thus, upon separation of the oligomer mixture, each functionalized graphite additive migrates to its preferred oligomers and forms a uniform dispersion.

Similarly, nanoparticle additives in polymer matrices can be used to develop new low haze ultrathin film optical coatings. A model system included an acrylate monomer as the continuous phase with monodisperse or bidisperse mixtures of silica nanoparticles deposited on glass and polycarbonate substrates. Surface (root mean squared roughness, Wenzel's contact angle) and optical properties (haze) of these self assembled experimental surfaces were compared to simulated surface structures. Manipulating the size ratios of silica nanoparticle mixtures varied the average surface roughness and the height distributions, producing multimodal structures with different packing fractions.

In both nanofluid and nanocomposite applications, nanoparticle additives tend to aggregate/agglomerate depending on various factors including the state of nanoparticles (powder, dispersion). A set of well-characterized ceria and titania nanoparticle products from commercial sources along with in-lab synthesized nanoparticles were studied via fractal theory. Fractal coefficients were obtained through two-dimensional images (from electron microscopy) and particle size distributions (from electron microscopy and dynamic light scattering). For some arbitrary collections of aggregated nanoparticle materials, the fractal coefficients via two-dimensional images correlated well to the average primary particle size. This complementary tool could be used

along with conventional nanoparticle characterization techniques when not much is known about the nanoparticle surfaces to characterize agglomeration or aggregation phenomena.

KEYWORDS: Phase behavior, Surface modification, Surface roughness, Haze, Fractal theory

Vinod Kanniah
Student's Signature

Date

NANOPARTICLE ADDITIVES FOR MULTIPHASE SYSTEMS:
SYNTHESIS, FORMULATION AND CHARACTERIZATION

By

Vinod Kanniah

Dr. Eric A. Grulke
Director of Dissertation

Dr. Stephen E. Rankin
Director of Graduate Studies

Date

To My Parents

Acknowledgement

First and foremost, I would like to express my sincere thanks to my advisor Dr. Eric A. Grulke on guiding me to be an independent researcher by working through self taught and providing the opportunity to work on diverse projects related to chemistry, materials and polymer science. I would also like to thank my Ph.D. committee (Dr. Stephen E. Rankin, Dr. Barbara L. Knutson, Dr. Mark S. Meier and Dr. Paul M. Bummer) for their time and effort to comment and review my research work.

I would like to thank all my friends and acquaintances at Lexington, KY along with Ms. Monica, Venkat N. Rajagopalan, my lab mates (Dr. Peng Wu, Binghui Wang, Natalia Mandzy, Chris G. Laine and Joseph Alexander) and student researchers (Molly Beavers, Callie Williams and Matthew Park) for their help and support in my research work at the University of Kentucky. I thank Dr. Jack Goodman (UKMSF) for assistance with the MALDI TOF, Dr. Thomas Dziubla (Chemical Engineering Department) for SEC, Mr. Brian L. Wajdyk (CeNSE) for AFM and CAER for TG-MS analysis.

Finally, I would like to thank Valvoline, ASHLAND Inc., (along with U.S. Army TARDEC division), Vision Dynamics Corporation LLC (along with DOE SBIR division) and US EPA Start award for the financial support for this work.

TABLE OF CONTENTS

Acknowledgement	iii
List of Figures	ix
List of Tables	xii
Chapter 1 Introduction	1
1.1 Nanoparticle additives for Nanofluids	2
1.2 Nanoparticle additives for Polymer Nanocomposites.....	7
1.3 Nanoparticle size distribution characterization.....	10
1.4 Dissertation overview.....	12
Chapter 2 Partition coefficient for a mixture of two lubricant oligomers	14
2.1 Highlights.....	14
2.2 Introduction.....	14
2.2.1 Partition coefficients.....	15
2.2.2 Phase equilibria	17
2.3 Experimental.....	17
2.3.1 Materials.....	17
2.3.2 Cloud point curve.....	20
2.3.3 Size exclusion chromatography.....	20
2.3.4 MALDI TOFMS	22
2.3.5 Overall phase composition: FT-IR	22
2.4 Results & Discussion.....	22
2.4.1 Cloud point curve (CPC).....	23
2.4.2 Quantitative analysis for PAO6 n-mers.....	25
2.4.2.1 SEC column calibration	28
2.4.2.2 Identification of PAO6 n-mer peaks	30
2.4.2.3 Poly(α -olefin) in separated phases	35
2.4.3 Quantitative analysis for PDMS oligomers.....	37
2.4.3.1 Identification of PDMS n-mer peaks	37
2.4.3.2 Laser power for spectral quality.....	39

2.4.4 Overall material balance	42
2.4.4.1 FT-IR peak selection.....	42
2.4.4.2 Material balance evaluations	44
2.4.5 Partition coefficients.....	46
2.4.5.1 Modeling K_{PAO6}	46
2.4.5.2 Modeling K_{PDMS}	49
2.5 Conclusion.....	52
2.6 Nomenclature	52
Chapter 3 Graphite functionalization for dispersion in a two phase lubricant oligomer mixture	54
3.1 Highlights.....	54
3.2 Introduction.....	54
3.2.1 Lubricant nanofluids.....	55
3.2.2 Graphite dispersion.....	56
3.2.3 Surface group analysis	57
3.3 Experimental.....	58
3.3.1 Materials.....	58
3.3.2 Functionalization.....	58
3.3.3 Characterization.....	61
3.4 Results & Discussion	62
3.4.1 Morphology.....	62
3.4.2 Surface groups - qualitative	64
3.4.3 Surface groups - quantitative	66
3.4.4 Surface density of hydroxyl groups.....	74
3.4.5 Partitioning of functionalized graphite	77
3.5 Conclusion.....	79
3.6 Nomenclature	79
Chapter 4 The effects of surface roughness on low haze ultrathin polymer nanocomposite films..	80
4.1 Highlights.....	80
4.2 Introduction.....	80

4.2.1 Surface properties	82
4.2.1.1 RMS roughness	82
4.2.1.2 Contact angle.....	83
4.2.2 Optical property	84
4.2.2.1 Haze	84
4.3 Experimental.....	85
4.3.1 Film morphologies	85
4.3.1.1 Simulation of film morphologies	85
4.3.1.2 RMS estimate for simulated surfaces	85
4.3.2 Measurement methods	85
4.3.2.1 Roughness of experimental surfaces.....	85
4.3.2.2 Analysis of peak height distributions.....	86
4.3.2.3 Haze (theoretical and experimental).....	86
4.3.2.4 Roughness factor and contact angle	87
4.3.3 Materials	88
4.3.4 Nanocomposite film recipes.....	90
4.4 Results & Discussion.....	93
4.4.1 Simulated surface morphologies.....	93
4.4.1.1 Effect of RMS and aspect ratio on Haze.....	95
4.4.2 Morphology of dual sized silica nanocomposite films.	99
4.4.2.1 Silica nanoparticles.....	99
4.4.2.2 Film surface roughness	101
4.4.2.3 Analysis of height distributions.....	104
4.4.2.4 Nanocomposite films on glass and polycarbonate.....	107
4.4.2.5 Wenzel's contact angle vs. r	108
4.4.3 Comparison of nanocomposite and simulated surfaces.	110
4.5 Conclusion.....	112
4.6 Nomenclature	112
 Chapter 5 Fractal analysis as a complimentary technique for characterizing nanoparticle size distributions	 114

5.1 Highlights.....	114
5.2 Introduction.....	114
5.2.1 Fractal analysis.....	118
5.2.1.1 2-D image analysis (box counting).....	118
5.2.1.2 Particle size distribution analyses.....	119
5.3 Experimental.....	120
5.3.1 Materials.....	120
5.3.2 Electron microscopy.....	123
5.3.2.1 Control test for box counting method.....	123
5.3.3 Dynamic light scattering.....	126
5.3.4 Zeta potential.....	126
5.4 Results & Discussion.....	126
5.4.1 Titania nanoparticles.....	126
5.4.2 Ceria nanoparticles.....	130
5.4.3 Effect of different surfaces on fractal parameters.....	136
5.4.4 Comparison of fractal analysis methods.....	140
5.4.4.1 Box counting method.....	140
5.4.4.2 Primary particle size distribution method.....	140
5.4.4.3 Hydrodynamic size method.....	141
5.5 Conclusion.....	143
5.6 Nomenclature.....	143
Chapter 6 Conclusions.....	144
6.1 Nanofluid additives for Nanofluids.....	144
6.1.1 Summary.....	144
6.1.2 Future research.....	145
6.2 Nanoparticle additives for Polymer Nanocomposites.....	145
6.2.1 Summary.....	145
6.2.2 Future research.....	146
6.3 Nanoparticle size distribution characterization.....	146
6.3.1 Summary.....	146

6.3.2 Future research	147
Appendix.....	148
Chapter 1: Supplementary information	148
Chapter 4: Supplementary information	151
References	153
Vita	160

List of Figures

Chapter 1

Figure 1.1 Research pathways to develop model 'universal base oil'. a) Characterization of oligomer phase behavior: A, B = oligomers chosen, b) Functionalization of nanoparticles (graphite) for dispersion in each oligomer phase: pretreatment to generate reactive site followed by coupling reactions. 6

Figure 1.2 Research pathway to develop model 'low haze ultrathin nanocomposite films'. Schematic of a bidispersed mixture nanocomposite (nanoparticle-acrylate monomer) film: MO_x1 = nanoparticle chosen. 9

Figure 1.3 Research pathway to develop 'complimentary characterization technique' for nanoparticle size distributions. a) Aggregation and agglomeration of primary particles, b) Process diagram on fractal analysis for nanoparticle characterization. 11

Chapter 2

Figure 2.1 (a) Phase volume ratio (r) Vs Temperature (b) Cloud Point Curve of PAO6-PDMS blend. 24

Figure 2.2 Raw chromatogram response curve of PAO6 and PDMS oligomers as obtained. 26

Figure 2.3 Differential distributions of PAO4, PAO6, and PDMS. PAO4 and PAO6 data from size exclusion chromatography and PDMS data from MALDI-TOF mass spectrometry. 27

Figure 2.4 Calibration curves with linear polystyrene standards. (a) molecular weights vs. retention times, b) peak area vs. sample mass, c) Peak t-test values. 29

Figure 2.5 Neat PAO6 oligomer data fit to (a) Gaussian area distribution, (b) Peak's t-test values. 34

Figure 2.6 PAO6 volume fractions in the top and bottom phases. 36

Figure 2.7 Cumulative frequency vs. molecular weight for neat PDMS n-mers. 38

Figure 2.8 Effect of the number of laser shots on PDMS n-mer detection. Cumulative molecular weight distributions of (a) Top phase, (b) Bottom phase. 40

Figure 2.9 PDMS volume fractions in the top and bottom phases. 41

Figure 2.10 FT-IR absorbance spectra of neat PDMS, neat PAO6 and a blend. 43

Figure 2.11 Partition coefficient estimates for PAO6 oligomer. 48

Figure 2.12 Partition coefficient estimates for PDMS oligomer. 51

Chapter 3

Figure 3.1 a) Reaction scheme for PAO6-philic and PDMS-philic graphite particles. b) Functionalization procedures for PAO6-philic and PDMS-philic graphite particles.	60
Figure 3.2 SEM images of a) as obtained graphite; b) citric acid treated graphite; c) PAO6-philic graphite; d) PDMS-philic graphite.	63
Figure 3.3 FT-IR absorbance spectra of a) neat PAO6 and neat PDMS, b) As obtained graphite, citric acid treated graphite, PAO6-philic graphite and PDMS-philic graphite.	65
Figure 3.4 TG curves of as obtained graphite and citric acid.	67
Figure 3.5 TG- DTG curves and TG-MS curves of citric acid treated graphite.	70
Figure 3.6 TG- DTG curves and TG-MS curves of PAO6-philic graphite.	71
Figure 3.7 TG- DTG curves and TG-MS curves of PDMS-philic graphite.	72
Figure 3.8 Images of the functionalized particles before and after partitioning in an equal volume PAO6: PDMS oligomer blend. (a) Temp. = 23°C and (b) Temp. = -18°C.	78

Chapter 4

Figure 4.1 Schematic diagrams of dual sized nanocomposite (silica-acrylate monomer) film characterization.	89
Figure 4.2 Two dimensional profiles of simulated surface morphologies. a) Tipped Pyramid, b) Pyramid, c) Inverse Pyramid, d) Plateau, e) Hills.	94
Figure 4.3 Effect of simulated surface morphology aspect ratio on RMS.	96
Figure 4.4 Effect of simulated surface morphology on Haze _T . a) Haze _T vs. RMS; b) Haze _T vs. aspect ratio.	98
Figure 4.5 Primary particle size distributions of silica nanoparticles. a) TEM of 100 nm silica. b) TEM of 10 nm silica. c) Comparison of particle size distributions by TEM and DLS.	100
Figure 4.6 RMS and Haze _T vs. 100 nm silica weight fraction.	102
Figure 4.7 AFM 3-D roughness profiles of nanocomposite surfaces. a) Hydrophilic (glass) and b) hydrophobic (polycarbonate) substrates. Nanocomposite recipes (A-D) of Table 1.	103
Figure 4.8 Peak deconvolution of AFM surface height distributions. a) Glass substrate, A-D. b) Polycarbonate substrate, A-D.	105

Figure 4.9 Effect of roughness parameter (r) on cosine of Wenzel's contact angle ($\text{Cos } \theta_w$) for tipped-pyramid simulated surface and experimental surfaces. 109

Figure 4.10 Comparison of experimental Haze_T to single and dual Gaussian models. 111

Chapter 5

Figure 5.1 a) Aggregation and agglomeration of primary particles, b) Process diagram on fractal analysis for nanoparticle characterization. 117

Figure 5.2 2-D TEM images of Titania nanoparticle samples (Sample ID: 1-3). 127

Figure 5.3 Effect of average primary particle size (from TEM) on: a) $D_f^{\text{BOX}}=\text{box}$ counting fractal dimension, b) $\Lambda^{\text{BOX}}=\text{box}$ counting lacunarity, c) $D_f^{\text{TEM}}=\text{TEM}$ fractal dimension and d) $\Lambda^{\text{TEM}}=\text{TEM}$ lacunarity of commercial Titania nanoparticle samples. 129

Figure 5.4 2-D TEM images of ceria nanoparticle samples (Sample ID: 4-6, 7-9, and 10-13). 131

Figure 5.5 Effect of average primary particle size (from TEM) on: a) $D_f^{\text{BOX}}=\text{box}$ counting fractal dimension, b) $\Lambda^{\text{BOX}}=\text{box}$ counting lacunarity, c) $D_f^{\text{TEM}}=\text{TEM}$ fractal dimension and d) $\Lambda^{\text{TEM}}=\text{TEM}$ lacunarity of commercial Ceria nanoparticle samples. 133

Figure 5.6 Effect of average primary particle size (from TEM) on: a) $D_f^{\text{BOX}}=\text{box}$ counting fractal dimension and b) $\Lambda^{\text{BOX}}=\text{box}$ counting lacunarity of in-lab synthesized Ceria nanoparticles . Effect of average primary particle size (from TEM) and average hydrodynamic aggregate size (from DLS) on c) $D_f^{\text{TEM/DLS}}=\text{TEM/DLS}$ fractal dimension and d) $\Lambda^{\text{TEM/DLS}}=\text{TEM/DLS}$ lacunarity of the same samples. 135

Figure 5.7 Effect of pH on Zeta potential of selected Ceria and Titania nanoparticle samples. 137

Figure 5.8 Effect of pH on a) Hydrodynamic aggregate size (from DLS) and b) Zeta potential of different surface chemistries on a particular in-lab synthesized Ceria nanoparticle sample (Sample ID: 5). 139

List of Tables

Chapter 2

Table 2.1 Material property data sheet of the oligomers.....	19
Table 2.2 Comparison of the three columns of mixed pore sizes used for quantitative analysis. ...	21
Table 2.3 Chemical composition of two poly(α -olefin)s.....	31
Table 2.4 Phase equilibria data via FT-IR analysis (preferred data in italic font).	45

Chapter 3

Table 3.1 Composition of weight loss based on TGA-MS: a) citric acid treated graphite, b) poly(α -olefin)-philic graphite, c) poly(dimethylsiloxane)-philic graphite.	73
Table 3.2 Coating morphology.....	75

Chapter 4

Table 4.1 Nanocomposite recipes. D_i = particle diameter; C_i = particle volume fraction; subscript L = large, subscript S = small.	92
Table 4.2 Peak deconvolution of height distributions. Peak modes with size range.	106

Chapter 5

Table 5.1 Sample descriptions of Ceria and Titania for fractal analysis.....	121
Table 5.2 Control test for 2-D image analysis (box counting method).	125
Table 5.3 Correlations and trends between D_{ave} , D_{hyd} and fractal coefficients.....	142

Chapter 1 Introduction

Nanoparticles, defined as particles having at least one dimension between 1 nm and 100 nm, are being considered for a wide variety of applications. When nanoparticles are added to a continuous phase, the resulting system may have different mechanical, optical, electrical, magnetic and thermal properties from those of neat continuous phase [1-6]. Nanofluids have nanoparticle additives dispersed in a continuous liquid matrix, whereas polymer nanocomposites have nanoparticle additives in a continuous polymer matrix [7]. Characterizations of these nanoparticle additives (particularly primary particle size) are needed to achieve liquids or solids in which the nanoparticle dispersion is well-controlled [8]. In general, uniform dispersion of nanoparticles, i.e., no agglomeration, is highly desired. However, in some applications, it is preferable to have agglomerated nanoparticles. One example would be nanocomposites for high heat transfer or electrical conductivity. In this case the preferred morphology would be agglomerated nanoparticles with very high electrical or thermal conductivity slightly above their percolation limit in the matrix [9]. The percolation limit is defined as the volume concentration at which the agglomerates form a continuous network throughout the solid, achieving high conductivity (primarily through the nanoparticle network) at low volume fractions of the discrete phase.

Support for this research has come from three different projects: nanofluids for improved heat transfer in mobility applications (funded by Valvoline and TARDEC), ultrathin polymer nanocomposite coatings for optical devices (funded by Vision Dynamics Corporation via several NSF and DOE SBIR awards), and characterization of nanoparticles for toxicology studies (funded by an EPA STAR award). This dissertation, Nanoparticle additives for multiphase systems: synthesis, formulation, and characterization, organizes the research done for these three problem-driven projects (nanofluids, polymer nanocomposites, and nanoparticle size characterization). The basic idea of this dissertation is to provide simple solutions to industrial problems by carefully exploring the techniques available in literature and the underlying fundamentals in each project.

Since this is a problem-driven research, Heilmeyer's catechism is answered for each project. George H. Heilmeyer, a renowned American engineer and businessman is credited for a set of questions for new product or process development projects [10]:

- What are you trying to do,
- How is it done today,
- What's new in your approach,
- Who cares,
- What difference will a successful project make,
- What are the risks/payoffs,
- How much will it cost, how long will it take, and
- What are the milestones to check for success?

Answers to this questionnaire create a basis for problem-driven research projects, which could lead to improved selection of research priorities and improved project planning. The Heilmeyer's matrix for each project is tabulated in Appendix. In general, research work also included proof of concept/principle as part of the overall plan.

1.1 Nanoparticle additives for Nanofluids

Nanoparticles are used as additives in nanofluids to reduce friction and wear for lubrication applications [9, 11-12]. These are two phase systems with the nanoparticle additives (discrete phase) dispersed in a continuous phase which is fluid. Nanofluids possess enhanced thermo physical properties such as thermal conductivity, thermal diffusivity, viscosity, and convective heat transfer coefficients compared to those of neat base fluids like oil or water [13]. Nanofluids with improved heat transfer have applications in moving mechanical components in metallurgy, machinery, automotives, railroads and thermal systems [7, 14]. Nanoparticles, such as multi-walled carbon nanotubes (MWCNT), fullerene, copper oxide, silicon dioxide, zinc oxide and silver, has been used with base fluids (DI water, ethylene glycol, oil, silicon oil, poly- α -olefin) to produce thermally conductive lubricating nanofluids [15]. Although a lot of research is done and reported on measuring the thermo physical properties of nanofluids, very little review is available on their preparation methods and stability mechanisms [13, 16] some of which are explained in this chapter.

Nanofluids are commonly prepared by a simple and economic two-step method which could be used on a large scale. The first step involves producing the desired nanoparticle additives as dry

powders by chemical or physical methods. In a second processing step, nanoparticles are dispersed into a fluid with the help of intensive magnetic force agitation, ultrasonic agitation, high-shear mixing, homogenizing, and ball milling [13]. The nanoparticles tend to aggregate because of their high surface area compared to micron sized particles and the surface energy of nanoparticles may not match the continuous phase in most cases [17]. It is necessary to functionalize the surface of nanoparticles with the aid of surfactants to achieve stable dispersions. However, the use of surfactants is limited only to low temperature applications (to avoid foaming, for example) [18] and hence several advanced but expensive one step methods of simultaneous production and dispersion of nanoparticles in continuous phases have been proposed in the literature. Some of these are a one-step physical vapor condensation method for copper based nanofluids [19], a vacuum-SANSS (submerged arc nanoparticle synthesis system) for copper based nanofluids in different dielectric continuous phases [20], a microwave irradiation method for copper [21] and silver [22] based nanofluids and a phase transfer method for graphene oxide nanosheet (GON) based nanofluids [23]. These processes are certainly not economically viable for large scale production and also have impurities in the form of residual reactants in the nanofluids. Hence, for most large scale nanofluid production and real time practical applications the traditional two-step method is preferred over the one step method.

Uniform dispersion or stable nanofluids are obtained by using appropriate surfactants as dispersant or by surface modification of nanoparticle additives. Surfactants have a hydrophobic tail portion and a hydrophilic polar head group that tends to increase the degree of contact between the continuous fluid phase and a nanoparticle additive. Selecting the right dispersant depends on the polarity of the continuous phase and the nature of nanoparticle additives. On the contrary, functionalization of nanoparticle additives is much preferred to achieve long term stability. It is usually not temperature limited and rarely leads to foaming. Its effect on thermal resistance between nanoparticle additives and continuous phase is small [18]. Functionalization of silica [24], titania [25], zinc oxide [26] and CNT [27] based nanofluids by silane grafting or coupling agents is relatively common. This method could be extended to other nanoparticle additives as well to achieve stable nanofluids.

Stability of nanofluids is often evaluated by simple sedimentation [28] or centrifugation [29] methods. Nanofluids are considered stable when the concentration or particle size of nanoparticle additives remains constant in the fluid over a long period of time before settling down to the bottom. Sedimentation photograph of nanofluids in test tubes taken by a camera is also a common method to observe the stability of nanofluids [16]. Zeta potential measurements are also reported as a measure of stability for some water based nanofluids. There is a significant electrical potential difference between the dispersion medium and the fluid layer near the dispersed particle [30-31]. Colloids (or nanofluids in this case) with high zeta potential (negative or positive) are electrically stabilized, while those with low zeta potentials (between -25 mV and +25 mV) tend to coagulate or flocculate. Quantitative methods based on spectral analysis have also been reported to measure the stability of nanoparticle additives if they have a characteristic absorption bands in the uv-vis wavelength range [28, 32]. Of all the stability evaluation techniques, the most simple and economic method for comparison purposes is the sedimentation photograph taken over different conditions or time periods.

The main objective of this work was to develop a 'universal base oil' for lubrication purposes that could be used in wide temperature ranges, typically from 160° C to as low as -80°C, while controlling its viscosity. Such universal base oils traditionally contain poly(α -olefins) based oligomers as the key component in formulations. But the pour point of poly(α -olefins) is not low enough to reach the low temperature specification of the desired universal base oil. Thus a model formulation containing a modest fraction of poly(dimethylsiloxane), which is still liquid at the low temperature specification, was investigated. Graphite was used as the nanoparticle additive to improve heat transfer properties, though determining the nanofluid heat transfer properties was beyond the scope of this dissertation. Since the model formulation oligomer mixture phase-separated at temperatures below -15° C, characterizing the oligomer mixtures was necessary to tailor these oligomers to prevent phase separation alongside achieving a continuous dispersion of nanoparticle additive (graphite) in this binary mixture. Figure 1.1 shows the research pathway in developing model universal base oil. The first step (Figure 1.1 a) was to characterize and be able to predict the phase separation of the oligomer mixture. The second step (Figure 1.1 b) requires creation of reactive sites on the graphite nanoparticle followed by coupling reactions to attach chemical groups that would cause the nanoparticles to partition to a specific phase when the

mixture separates. Pretreatment involves creating reactive surface groups on the nanoparticle additive. Functionalization involves coupling reaction between the reactive surface groups and silanes chosen based on the nature of the oligomers.

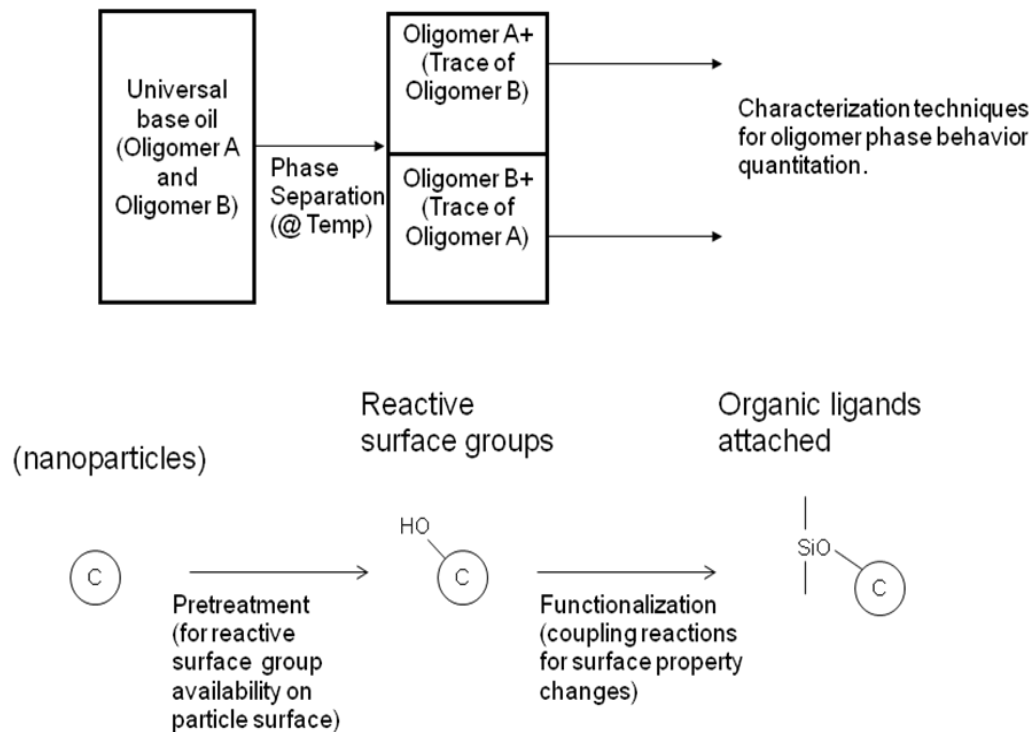


Figure 1.1 Research pathways to develop model 'universal base oil'. a) Characterization of oligomer phase behavior: A, B = oligomers chosen, b) Functionalization of nanoparticles (graphite) for dispersion in each oligomer phase: pretreatment to generate reactive site followed by coupling reactions.

1.2 Nanoparticle additives for Polymer Nanocomposites

Nanoparticles are also used as additives to improve mechanical properties (shear strength, stiffness, packing) of polymer-nanocomposites [33-35]. The exceptional properties of polymer nanocomposites are due to mechanisms such as: a) polymer chains are confined by the nanoscale particles, which are in the size range of the radius of gyration of polymer chains, b) the nanoparticle additives have unique properties (mechanical, optical, thermal and/or others) that are superior to macroscopic particles, and c) the arrangement of nanoscale additives in a polymer matrix [33, 36]. These three mechanisms may be achieved at much lower loading levels than other traditional fillers, thereby enhancing the desired bulk property of the final nanocomposite. Promising applications are achieved by tuning the nanoparticle additives and the polymer matrix based on their size dependent properties. These polymer nanocomposites have applications in coatings primarily anticorrosion [37-38], scratch resistant [39-40], flame retardant [40], shape memory materials [41], medical implant materials such as dental materials [42], and optical filters in optoelectronic systems [43-44].

Common challenges in developing polymer nanocomposites for coating applications have been: 1) abrasion resistance of coatings or adhesion characteristics of coating to substrate, 2) choosing the correct nanoparticle additives/polymer matrix pair based on substrate and properties desired and 3) uniform deposition of the nanocomposite over substrates to achieve desired thickness. Three common methods to process polymer nanocomposites are via melt compounding, *in situ* polymerization and the solvent method. For coating applications, the simplest processing technique is to mix nanoparticle additives into a polymer solution. Commonly used cost effective deposition techniques for optical coatings are via dip coating, spray coatings for large area substrates, and spin coatings for comparatively small area substrates.

The main objective of this work was to develop 'low haze ultrathin film' for optical product applications (hydrophobic coatings). It is done today by using a nanoparticle-acrylate monomer nanocomposite system. We propose a model nanocomposite (bidisperse mixtures of silica-acrylate monomer) system to control surface roughness (to improve hydrophobicity) and haze (optical transparency). Figure 1.2 shows the research pathway to proof of concept of low haze ultra thin films for a) hydrophobic and b) antireflective optical product applications. Figure 1.2 a) describes

the bidispersed mixtures of (100nm and 10 nm) silica along with an acrylate monomer to render surface roughness within an ultrathin film. A simple inexpensive spin coat deposition technique is used to obtain uniform coatings over different substrates (hard/flexible).

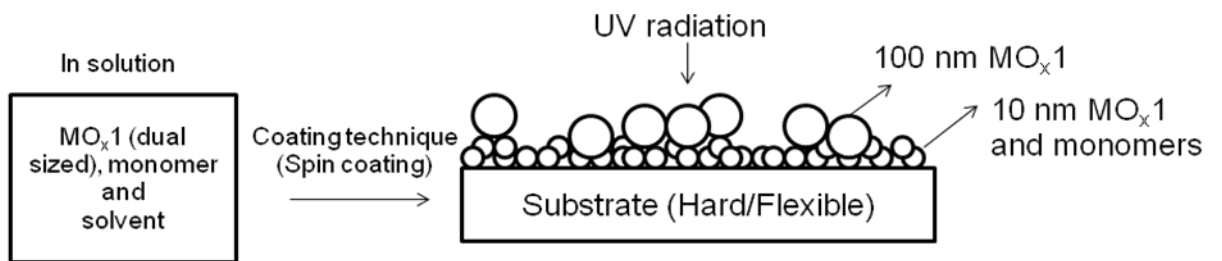


Figure 1.2 Research pathway to develop model 'low haze ultrathin nanocomposite films'.
 Schematic of a bidispersed mixture nanocomposite (nanoparticle-acrylate monomer) film: MO_x1 =
 nanoparticle chosen.

1.3 Nanoparticle size distribution characterization

Nanoparticles are traditionally characterized to measure size, shape, surface charge, surface area, surface porosity, composition and structure to predict aggregation/agglomeration behavior of nanoparticle systems [8]. These measurements are critically important for toxicity testing, which is gaining more attention around the world. Aggregation/agglomeration phenomenon is a crucial controlling factor in many engineering process and products development. Hence, a complimentary technique based on fractal theory (explained in chapter 5) is explored to characterize nanoparticle size distributions; this method is considered complimentary to traditional characterization techniques (electron microscopy or dynamic light scattering), and provides extra information about primary particle size distributions as well as their associations in various media.

The main objective of this work was to develop 'complimentary characterization technique' for nanoparticle size distributions that focused on agglomeration and aggregation effects. Size distributions are traditionally done by electron microscopy (for powders) and light scattering (for liquid dispersions) methods. A fractal based approach is proposed to characterize size distribution for quality control of nanoparticle production. This would also help describe aggregation/agglomeration phenomenon of nanoparticle systems when not much is known about their surface chemistry/properties. Similarly, the parameters obtained from this technique could be related to other surface based parameters. Figure 1.3 shows the research pathway to proof of concept for the fractal based characterization technique for nanoparticle size distributions. Figure 1.3 a) describes the aggregation and agglomeration phenomenon observed in powder and liquid states of nanoparticles. Figure 1.3 b) describes the development of fractal based characterization from 2-dimensional image analysis (box counting), hydrodynamic size distribution (dynamic light scattering) and primary particle size distribution (electron microscopy). Fractal based parameters were determined from each technique and related to aggregation, agglomeration phenomenon.

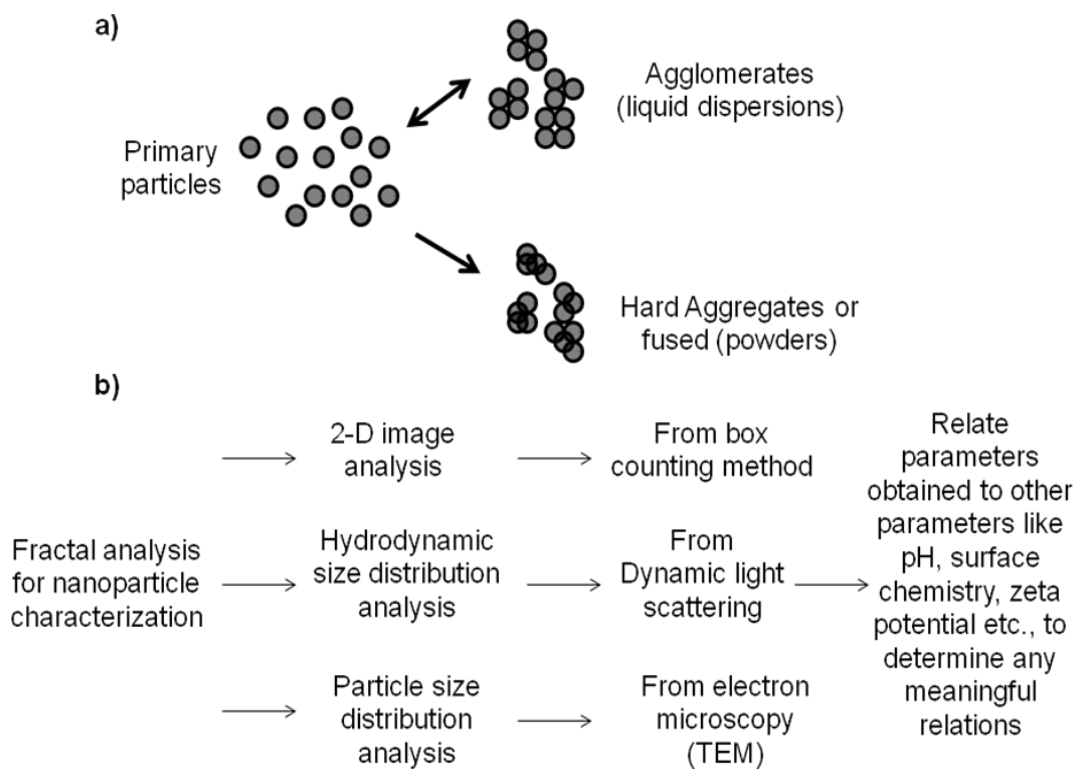


Figure 1.3 Research pathway to develop 'complimentary characterization technique' for nanoparticle size distributions. a) Aggregation and agglomeration of primary particles, b) Process diagram on fractal analysis for nanoparticle characterization.

1.4 Dissertation overview

The objective of this dissertation is to provide simple, cost-effective solutions for nanoparticle additive based applications, especially synthesis, formulation and characterization challenges. For each project (or following chapters in this case, brief highlights of findings is followed by a detailed introduction, experimental, results and discussion sections. Details on each instrument/equipment (principle and methods) are explained in each chapter as it is used.

Chapter 2 and 3 addresses issues with developing nanofluids for mobility vehicle applications. Chapter 2 describes the partitioning of lubricant oligomer mixtures which are one approach to expanding the use range of engine oils. A brief introduction to phase behavior methods is followed by characterization techniques chosen for quantitation: Gel permeation chromatography, Matrix assisted laser desorption/ionization based time of flight mass spectrometry (MALDI-TOFMS) and Fourier Transform Infrared Spectroscopy (FT-IR). Partition coefficients of each oligomer were determined experimentally and fitted to simple empirical equations. In Chapter 3, a method to disperse graphite (as nanoparticle additive for improved heat transfer) in the phase separating binary oligomer mixture is described. A brief introduction to lubricant nanofluids, graphite dispersion and surface group analysis is followed by morphology analysis (Scanning electron microscopy (SEM)) surface group characterization analysis (qualitative: FT-IR) and (quantitative: Thermo gravimetry with mass spectrometry (TG-MS)).

Control of the surface roughness of ultrathin nanocomposite films might improve interlayer adhesion, change the apparent interracial tension, and develop local property gradients in layered optical devices. Chapter 4 describes the effects of surface roughness on optical transparency (haze) of polymer nanocomposites. A brief introduction to ultrathin nanocomposite film development and their characterization techniques: Atomic force microscopy (AFM), Goniometer, Hazemeter for experimental surfaces is detailed. Along with surface and optical properties, height distributions and packing fractions of experimental surfaces is also explored. Simulated surfaces via MATLAB are compared to experimental self assembled surfaces.

Agglomeration of nanoparticles in fluids and nanocomposites are difficult to characterize: fractal analysis might be a new method for identifying and characterizing self-association of nanoparticles.

Chapter 5 describes an overview of fractal based nanoparticle characterization through image analysis, electron microscopy (TEM) and dynamic light scattering (DLS) based size distributions. Research outcomes for each of the projects (Chapter 2 through Chapter 5) followed by future work that could be pursued is reported at the end (Chapter 6).

Chapter 2 Partition coefficient for a mixture of two lubricant oligomers

This chapter is based on work published as: *Vinod Kanniah, Reg T. Forbus, S. M. Parker, Eric A. Grulke, Journal of Applied Polymer Science, 2011, Vol. 122, No.5, pp. 2915-2925 (Copyright: Wiley-Blackwell).*

Keywords: Oligomers, Phase separation, SEC, MALDI, FT-IR

2.1 Highlights

- Partition coefficients were measured for a two-phase mixture of poly(α -olefin) and poly(dimethylsiloxane).
- Phase compositions of poly(α -olefin) and poly(dimethylsiloxane) were determined by size exclusion chromatography and MALDI TOFMS, respectively.
- Poly(α -olefin) partition coefficients increased with increase oligomer chain length and were insensitive to temperature.
- Poly (dimethylsiloxane) partition coefficient decreased with oligomer chain length.
- Partition coefficient data could be used to develop oligomer mixtures with different cloud points.

2.2 Introduction

Alpha-olefin oligomers, often called poly(α -olefins), are commonly used as synthetic lubricant base stocks [45]. Poly(α -olefins) based on 1-decene oligomers (PAOs) have an extended range of operating temperatures relative to petroleum-based base oils and are a good starting point for developing universal base oil products. Synthetic oils have excellent properties, including high viscosity indexes, low pour points, and excellent shear stabilities. PAO commercial products with low kinematic viscosities are short-chain branched oligomers (dimers to heptamers) that have been hydrogenated to improve thermal stability [46]. Products with different kinematic viscosities are based on compositions with different sets of major n-mer components. For example, PAO-2 (kinematic viscosity of 1.8 mm²/s at 100 °C) has mostly dimer (99%) with some trimer while PAO-8 (kinematic viscosity of 7.9 mm²/s at 100 °C) has mostly tetramer (56%) and pentamer (27%) with some trimer (6%), hexamer (7%) and heptamer (4%) [46].

There are several approaches to extending base oil use over a wider temperature range. One approach would be to vary the oligomer distribution and branching by modifying the polymerization process. A second approach would be to add a modest fraction of a second lubricant that has improved low temperature properties. Oligomer blends of two chemically different materials provide an interesting option for varying lubricant properties for a variety of applications. This work describes the measurement of the phase equilibria of such mixtures, and the partition coefficients for the oligomers components between the two phases. The results can be used to tailor oligomers distributions so as to induce, or prevent, phase separation of binary oligomers mixtures over specific temperature ranges.

The specific model system, a mixture of 20 wt% of poly(dimethylsiloxane) (PDMS) in PAO6, had improved low temperature viscosities compared to PAO6 base oil product. PDMS oligomers have a high viscosity index (low variation with temperature) and a comparatively low pour point, generally lower than 193 K. In contrast to the PAO family of products, the specific PDMS oligomer products used in this study contained a sequential series of linear n-mers having between 20 to 40 separable components. Different PDMS oligomer products have different average molecular weights, i.e., contain different distributions of n-mers. The PAO6/PDMS mixture is homogeneous at room temperature but separates at lower temperatures into a PAO6-rich continuous phase with PDMS-rich droplets.

2.2.1 Partition coefficients

Phase equilibria for liquid–liquid systems are often based on fugacities or activity coefficients. At equilibrium, the fugacity of component 1 is the same in each of the two phases (a,b = Top and bottom phase, 1, 2 = Components of a blend, T = temperature, P = Pressure, x = mole fraction, f = fugacity):

$$f_{1a}(T, P, x_a) = f_{1b}(T, P, x_b) \quad \text{Eq. 2.1}$$

Fugacity could be written in terms of an activity coefficient (γ) as:

$$f_1(T, P, x_a) = x_{a1} \gamma_{a1}(T, P, x_a) f_1(T, P) \quad \text{Eq. 2.2}$$

For simple fluids, the activity coefficient is defined using mole fraction as the concentration variable. However, volume fractions are usually more convenient for modeling polymer phase equilibria. The partition coefficient, K (the ratio of component concentrations (Φ) in each phase) is equivalent to the activity coefficient ratio. Thus, the partition coefficient and activity coefficient for polymeric systems are related as:

$$\Phi_{1a} \gamma_{1a}(T, P, \Phi_a) = \Phi_{1b} \gamma_{1b}(T, P, \Phi_b) \quad \text{Eq. 2.3a}$$

$$K_1 = \Phi_{1a} / \Phi_{1b} = \gamma_{1b}(T, P, \Phi_b) / \gamma_{1a}(T, P, \Phi_a) \quad \text{Eq. 2.3b}$$

There has been some prior work on the partition coefficients for homologous series of oligomers related to polymer fractionation or changing solvents for polymerization and processing [47-51]. Much of this research has focused on using supercritical fluids (such as carbon dioxide) or fluids near their critical points, where the solvency properties can be manipulated to control phase separation. For these systems, researchers have used a simple empirical model to describe the partitioning of individual components between the solvent-rich and the polymer-rich phases [52]:

$$\ln(K_i) = \ln\left(\frac{w_i^s}{w_i^p}\right) = -\sigma \cdot n + \ln \xi \quad \text{Eq. 2.4}$$

where the partition coefficient, K_i , is based on the weight fraction of component i distributing between the solvent-rich (w_i^s) and polymer-rich phases (w_i^p), σ is a 'separation' factor that describes the dependence of K_i on the oligomer's chain length (degree of polymerization), n , and ξ is a constant. For a relatively poor polymer solvent such as carbon dioxide, the oligomer component partition coefficients may decrease by several orders of magnitude as chain length increases and σ is a constant [52]. However, for liquid solvents [53] or for samples with very broad distributions [54], σ may vary with chain length. In this study, the partition coefficients are based on volume fractions rather than weight fractions.

2.2.2 Phase equilibria

Liquid–liquid equilibria of binary mixtures are usually expressed in terms of phase diagrams. In general, there are three ways of representing phase behavior namely, cloud point curve (CPC), coexistence curve (CC) and partition coefficient (K). The determination of the cloud point curve for a system requires that a single phase mixture be cooled or heated until the liquid becomes turbid or swells, i.e., reaches cloud point, indicating the appearance of another phase. All the methods known for cloud point determination require some amount of the second phase to be present so that the change can be observed [55]. The observed temperature may not be precise, and cloud point temperatures are usually confirmed by more than one technique. Also, cloud point curves can depend on chain length and system pressure [56-57]. Coexistence curve describes the composition of each phase after separation for a known initial composition, but is relatively tedious to obtain compared to cloud point curves. The simplest techniques for cloud point curves of polymer blends are turbidity and phase volume ratio measurements [58], which will be used here.

The volume fractions of n-mers in each phase (Eq. 2.3b) were determined by measuring the phase's total oligomer content and volume, and measuring the relative amount of every n-mer. MALDI TOF mass spectrometry [59] was used to determine the relative distributions of poly(dimethylsiloxane) n-mers while size exclusion chromatography [60] was used to determine the relative distributions poly(α -olefin) n-mers. Total oligomer contents were measured using FT-IR [61]. The reported data were shown to satisfy the overall material balances for each oligomer as well as the individual balances for every n-mer.

2.3 Experimental

2.3.1 Materials

The oligomer components of this study were poly(dimethylsiloxane) (CAS Reg # 42557-10-8, SK96-10, trimethylsilyl endgroups, GE Silicones, USA) and poly(α -olefin) (CAS Reg # 68037-01-4, Chevron Phillips Chemical Company LP, USA). Poly(dimethylsiloxanes) is commercially available with trimethyl, hydroxyl and hydrogen endgroups. The trimethyl end group products were chosen specifically to provide better compatibility with the poly(α -olefin) base oils. The properties of the two oligomer systems are listed in Table 2.1. Surface tension of the fluids was determined by the pendant drop technique using a goniometer. Refractive index was found using a refractometer with

a sodium vapor lamp source. Dynamic viscosity of the fluids was determined using concentric cylinder arranged rheometer. All the neat fluids were Newtonian in the shear range of 1-1000 s⁻¹ averaged over 15 data points within the temperature range 283 K - 393 K.

Molecular weight of poly(dimethylsiloxane) additive to be used in a modest fraction in the model system has high molecular weight than poly(α -olefin). This implies low vapor pressure i.e., low evaporative losses in engine from the additive. Kinematic viscosity of both the oligomers was nearly matched. The difference in surface tension of the oligomers chosen was very low. Pour point of poly(dimethylsiloxane) was much lower than poly(α -olefin). Also, absolute value of poly(α -olefin)'s activation energy of was higher than poly(dimethylsiloxane) suggesting a larger variation in viscosity with temperature than poly(dimethylsiloxane) via Arrhenius equation (for dynamic viscosity modeling).

Table 2.1 Material property data sheet of the oligomers.

Properties	PDMS	PAO6	In house laboratory technique/Reference
CAS Reg #	63148-62-9 (42557-10-8)	68037-01-4	-
Density, Kg/m ³ @ 295 K	932.7 ± 1.243	816.6 ± 1.455	density measurements
Avg. Mol. Wt., kg/kmol	1776	~553	[62] for PAO6
Monomer, kg/kmol	74	140	
Average # of repeating units	24	4 (2 to 7)	
Molar volume, m ³ /kmol	0.525	0.97	
Kinematic viscosity, cSt	10	6	supplier MSDS
Surface Tension, mN/m @ 295 K	20.3 ± 1.8×10 ⁻¹	29.3 ± 1.5×10 ⁻¹	Drop Size Analyzer 10, KRUSS, USA
Refractive Index, @ 295 K	1.399	1.457	Refractometer Na D illumination
Dynamic Viscosity, Pa.s 283 K - 393 K $\mu = \mu_0 e^{(-E_\mu/RT)}$; R=8.314 J/mol.K	$\mu_0=4 \times 10^{-5}$ ± 2×10 ⁻⁶ E _μ =-13400 ± 110	$\mu_0=3.7 \times 10^{-8}$ ± 8×10 ⁻⁹ E _μ =-34900 ± 530	Rheometer ATS Reologica, USA
Pour Point, K	173	211	supplier MSDS

2.3.2 Cloud point curve

The cloud point curve was determined through turbidity and phase volume ratio (r) measurements. Turbidity measurements involve cooling (or heating) the sample and recording the appearance (or disappearance) of turbidity with temperature. The samples were cooled in a refrigerated methanol bath maintained at 233 K. The cloud point temperature was that at which the mixture turned clear from turbid (tests were run in triplicate). The cloud point temperatures from turbidity experiments were compared to those of the phase volume ratio method. A homogenized sample with a known initial composition was separated at a specific temperature, and its corresponding phase volumes were measured. The extrapolation of phase volume curve to $r = 0$ gives the cloud point temperature. The exact time required for separation varied depending on the temperature, molecular weight and concentration of the oligomers. Hence, three samples of each composition were refrigerated for 48 hours to ensure complete phase separation and settling. The volume of the top phase was measured using a graduated pipette (with 0.1 ml precision). Care was taken to avoid intermixing of phases.

2.3.3 Size exclusion chromatography

Quantitative analysis of PAO6 was done using size exclusion chromatography. Three columns of mixed pore sizes (Styragel HR1, Styragel HR2 (Waters Inc., USA), PL Gel Mixed E (Polymer Labs Inc., USA)) were used for efficient retention (see Table 2.2). Tetrahydrofuran (density = 0.889 g/ml at 295 K, HPLC grade, Fischer Scientific Inc., USA) was the standard eluent solvent for this instrument. A differential refractive index detector (Model 2410, Waters Inc., USA) was used. An auto sampler (SIL-20A HT, Shimadzu Inc., USA) was used to the samples. Column conditions used were: volumetric flow rate of 1 ml/min, column temperature of 313 K, injection volume of 20 μ l and RI detector sensitivity of 128.

PDMS/PAO6 blends of 0.179 volume fraction ($v/(v+v)$) PDMS were phase separated at three temperatures (233 K, 243 K, 258 K). After centrifuging, samples of the top and bottom phases were drawn via syringe and diluted with THF. Care was taken to prevent intermixing of phases during sampling. The total cycle time was set to 10 minutes greater than the sample elution time to ensure that the columns were completely flushed before the next injection.

Table 2.2 Comparison of the three columns of mixed pore sizes used for quantitative analysis.

	Styragel HR1	Styragel HR2	PL Gel Mixed E
Source	Waters Inc., USA	Waters Inc., USA	Polymer Labs Inc., USA
Column type (stationary phase)	Styrene divinyl benzene formulation	Styrene divinyl benzene formulation	Styrene divinyl benzene formulation
Column dimension (length × inner diameter)	300 mm × 4.6 mm	300 mm × 7.8 mm	300 mm × 7.5 mm
Effective Mol.Wt. range	100-5000	500-20000	< 30000

2.3.4 MALDI TOFMS

Matrix Assisted Laser Desorption/ Ionization Time of Flight Mass Spectrometry (MALDI TOFMS) experiments were performed to determine the molecular weight distribution of PDMS oligomer. MALDI mass spectra were obtained in a linear mode on a Bruker Daltonics autoflex time-of-flight mass spectrometer (Billerica, MA), using a DHB matrix. DHB (2, 5 dihydroxybenzoic acid) matrix was used for analysis of polymer mixtures containing PDMS and PMMA using MALDI TOFMS [59]. The matrix and conditions of Yan et al [59] appear to give relative signal intensities adequate for quantitative measurements of the various oligomers. A thin film technique of sample preparation was used. DHB matrix dissolved in 50 wt % methanol-water mixture was deposited on the sample carrier. Once the solvents evaporated, the analyte solution samples were then deposited over the dry matrix. Analyte samples were made to a concentration of 1mg/ml in dichloromethane (DCM). Instrument conditions were: voltage extraction – IS1 20 kV, IS2 18.65 kV, lens 8.25kV, pulsed ion extraction – 50ns, matrix suppression – gating, medium, and up to 650 Da. Neat PDMS samples and samples from PDMS-rich phases gave almost reproducible data when hit by varying laser shots (100 to 200). However, samples from PAO6-rich phases required 200 laser shots for consistent results. All data reported for partition coefficient estimates used 200 laser shots since the absolute intensity of MALDI signal is affected by laser and matrix crystallization conditions. The data obtained was thus optimized for these samples based on good signal to noise ratio (i.e., signal stands out of the background) and good mass resolution (i.e., narrow peak width).

2.3.5 Overall phase composition: FT-IR

FT-IR was used to determine the total PDMS and PAO6 concentrations in each phase of separated mixtures. A NEXUS 470 FTIR spectrometer with an ATR accessory, a ZnSe window and a DTGS KBr detector were used.

2.4 Results & Discussion

Cloud point curves were measured to establish the extent of separation based on temperature and composition. Different measurement techniques were used for each oligomer family as no single tool could detect both materials simultaneously. For example, their molecular weight ranges overlapped, so that size exclusion chromatography data would need to be deconvoluted based on two different curve shapes. FT-IR was used to measure of the total amount of oligomer in the

separated phases. This approach provides n-mer volume fraction data confirmed by material balances. The n-mer partition coefficient data of each oligomer family were compared to Eq. 2.4, which has been used to model n-mer partitioning data for other applications such as polymer fractionation and polymerization solvent replacement.

2.4.1 Cloud point curve (CPC)

Cloud point curve and phase volume ratio for a volume fraction of PDMS oligomer ($=0.179$ ($v/v+v$)) in the blend is shown in Figure 2.1. Figure 2.1(a) corresponds to the phase volume ratio and Figure 2.1(b) to the cloud point curve of the system. As the temperature is lowered, the amount of PDMS miscible with PAO6 decreased. Phase volume ratio of the oligomer mixture showed the extent of separation possible at those temperature and composition. The cloud point temperature obtained by extrapolating the phase volume ratio to temperature was close to temperatures obtained through turbidity method, verifying the measurements as reasonable values.

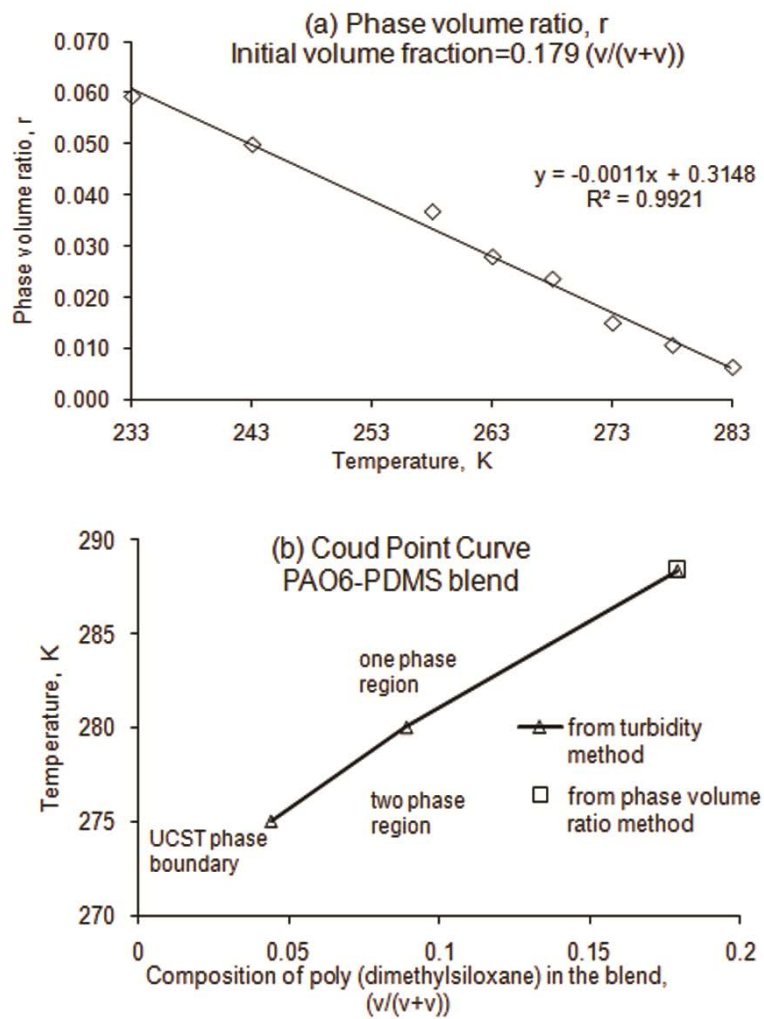


Figure 2.1 (a) Phase volume ratio (r) Vs Temperature (b) Cloud Point Curve of PAO6-PDMS blend.

2.4.2 Quantitative analysis for PAO6 n-mers

PAO6 n-mers were easily detected by size exclusion chromatography (SEC) column due to the large difference between their refractive index and that of the solvent ($n_d = 1.4570$ (PAO6) vs. $n_d = 1.4072$ (THF)). PDMS oligomers went undetected by refractive index detectors ($n_d = 1.3999$ (PDMS)) (Figure 2.2) as well as UV-Vis and fluorescence detectors. Even though the manufacturer's specification of average molecular weight differed (Table 2.1), the apparent molecular weight distribution of two oligomer systems overlapped. PAO6 branched oligomers eluted with apparent molecular weights of ~580 Da to ~1400 Da. The linear PDMS oligomers had a molecular weight range from ~600 Da to ~3300 Da (from MALDI TOF). These ranges overlap (as shown in Figure 2.3), greatly complicating the interpretation of the SEC data. The use of a specific analytical tool: SEC for PAO6 n-mers and MALDI TOF for PDMS n-mers eliminated potential interferences, but required the use of an overall material balance to select the most accurate measurements.

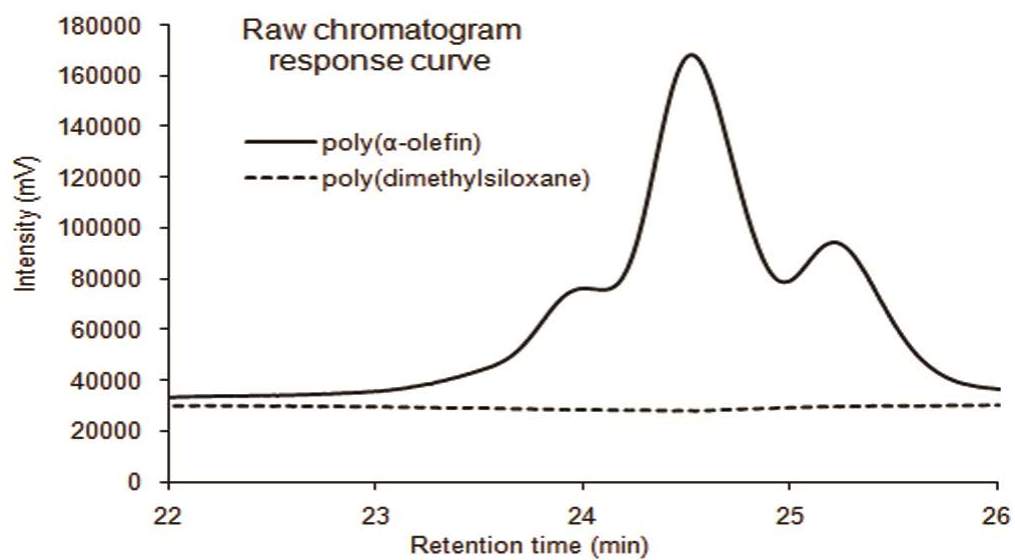


Figure 2.2 Raw chromatogram response curve of PAO6 and PDMS oligomers as obtained.

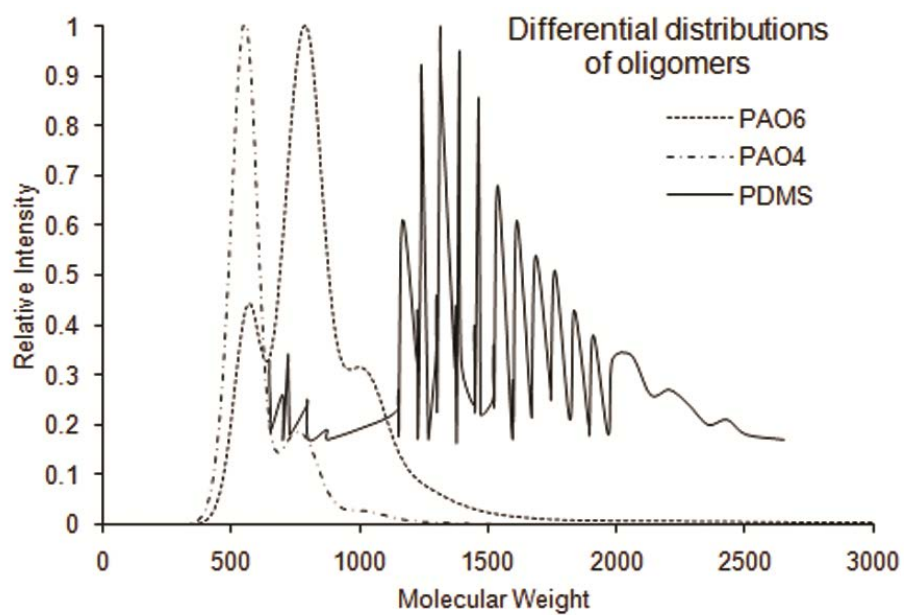


Figure 2.3 Differential distributions of PAO4, PAO6, and PDMS. PAO4 and PAO6 data from size exclusion chromatography and PDMS data from MALDI-TOF mass spectrometry.

2.4.2.1 SEC column calibration

The SEC column was calibrated using 9 linear polystyrene standards ($580 < M_w < 19880$). The log (M_w) vs. retention time plot was linear ($R^2 = 0.994$, Figure 2.4a) as was the plot of peak area vs. oligomer mass ($R^2 = 0.996$, Figure 2.4b). Several statistical models were evaluated (lognormal, modified Gaussian, exponentially modified Gaussian), but the Gaussian area was chosen based on its simplicity and fit to the data. Gaussian Area or Normal distribution (Equation 2.5) has 3 parameters: area under the curve, A_0 (peak area); mean, A_1 (peak center) and the standard deviation, A_2 (peak width).

$$y = \frac{A_0}{\sqrt{2\pi}A_2} \exp\left[-\frac{1}{2}\left(\frac{x - A_1}{A_2}\right)^2\right] \quad \text{Eq. 2.5}$$

The maximum percent variation allowed for parameter estimates were set to A_0 (25%), A_1 (1%), and A_2 (25%) respectively. These functions were converged numerically through least squares minimization to obtain parameter estimates. When a specific distribution model is selected, the student t-test parameter can be used to evaluate the quality of fit, specifically, the location of the center of the peak and the peak area. For the linear polystyrene standards, the t-test values for peak centers and peak areas greatly exceed the 95% confidence value (Figure 2.4c), particularly for molecular weights less than 3000 Da. The high t-test value for peak centers is due, in part, to the low tolerance permitted for coefficient A_1 in the fitting procedure.

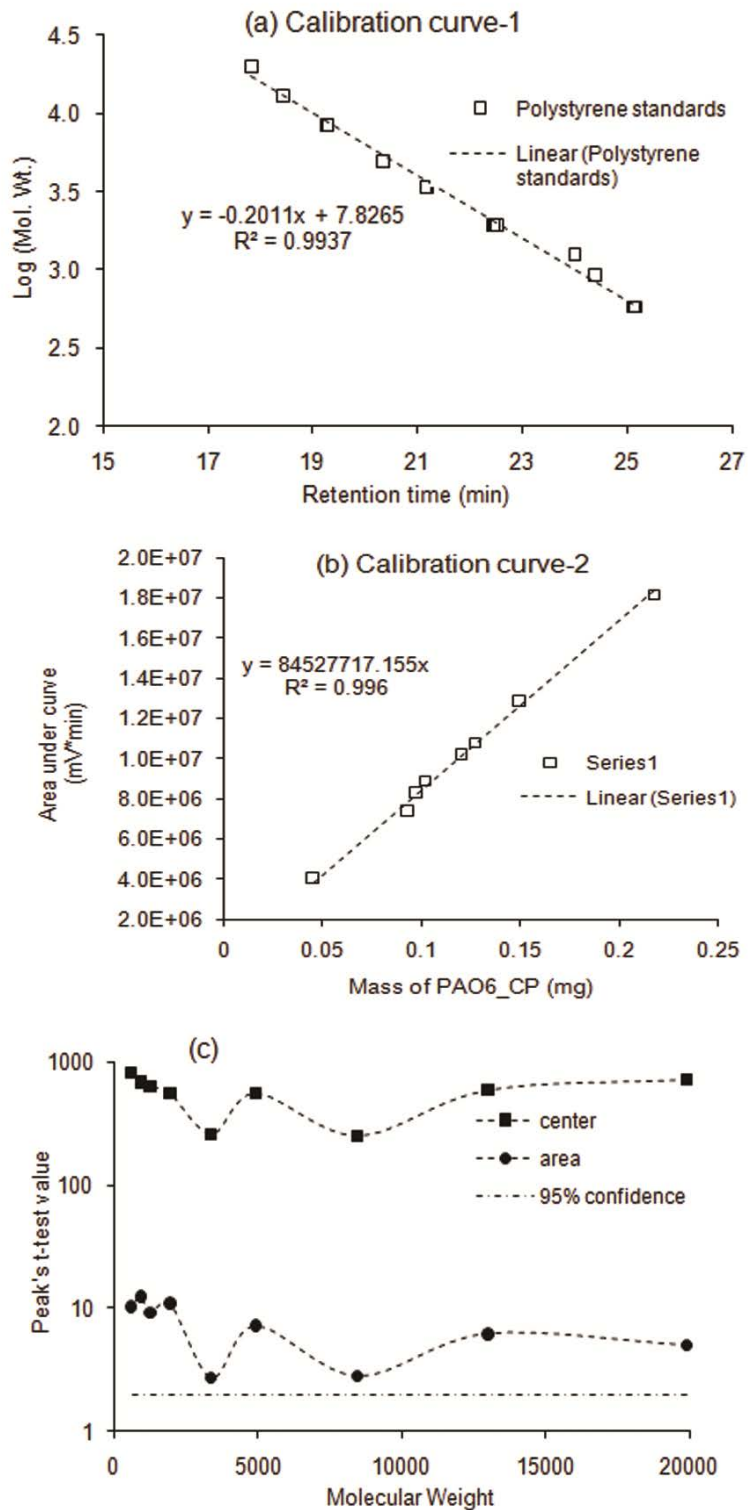


Figure 2.4 Calibration curves with linear polystyrene standards. (a) molecular weights vs. retention times, b) peak area vs. sample mass , c) Peak t-test values.

2.4.2.2 Identification of PAO6 n-mer peaks

The low molecular weight PAO family of lubricants is produced by polymerizing 1-decene to oligomers with a BF_3 catalyst system followed by hydrogenation [46]. NMR data show that an extra branch exists for such oligomers, which is thought to be caused by a skeletal rearrangement of the oligomers [63]. A typical composition of PAO6 is shown in Table 2.3 [62]. Trimer, tetramer and pentamer are its major components (94 wt %), and hexamer, heptamer and dimer are its minor components (< 6 wt %). Commercial PAO6 samples would be expected to have the same major components (trimer, tetramer and pentamer); therefore, the major peaks should be the same, even with typical lot-to-lot variations.

Table 2.3 Chemical composition of two poly(α -olefin)s.

Component (nominal Mw)	PAO6 peak center ^a	PAO6 wt % ^a	PAO6 wt % [62]	PAO4 peak center ^b	PAO4 wt % ^b	PAO4 wt % [62]
Dimer (280)	-	-	0.1	-	-	0.6
Trimer (420)	582	22.5	33.9	548	84.9	84.4
Tetramer (560)	792	55.1	43.5	759	15.1	14.5
Pentamer (700)	1018	17.5	17.4	-	-	0.5
Hexamer (840)	1224	4.19	3.8	-	-	-
Heptamer (980)	1413	0.74	1.3	-	-	-

^a= data in Figure 2.6; ^b=analysis of data in Figure 2.3.

SEC chromatographs of neat PAO6 were deconvoluted using commercial software (Peak Fit Version 4.12) to determine the percent area contributed by each peak (Figure 2.5a). Three major peaks and two minor peaks were observed (Table 2.3), and were assumed to be trimer, tetramer, pentamer, hexamer and heptamer in their elution order. A small lead peak (dimer) was not detected. The hydrogenated n-mers should have actual molecular weights that are nearly integer multiples of the monomer value, i.e., 280, 420, 560, 700, 840 and 980 for dimer through heptamer. However, the apparent molecular weights (peak centers) of the PAO6 oligomers were higher than their nominal molecular weights. This peak assignment correctly describes another poly(α -olefin), PAO4, as shown in Table 2.3.

SEC separations are based on the hydrodynamic radii of the macromolecules, which will vary with the chemical composition of the chain and its configuration (linear, branched, star, for example) [64] (and literature cited therein). A number of factors could cause PAO6 oligomers to have higher than expected hydrodynamic radii. A molecular dynamics study of the effective dimensions of oligomers in size exclusion chromatography showed that the effective hard-sphere radii (the 'retention radii') of molecules < 5,000 Da were larger than their radii of gyration [65]. Furthermore, different polymers had different retention radii, which were attributed to the asphericities of their individual configurations. Trimers, tetramers and pentamers based on 1-decene have branch lengths that are similar in size to the chain backbone, and can be categorized as star-type molecules. Size exclusion chromatography data of some star-type oligomers (2000 Da < Mn < 5500 Da) shows much higher (40-100%) apparent molecular weights [66]. Since this is a homologous sequence of oligomers polymerized by the same catalyst, there is likely to be a consistent relationship between the apparent molecular weight and the actual molecular weight. A power law relation was used as an empirical model:

$$Mw_{app} = a \cdot (Mw_{n-mer})^b \quad \text{Eq. 2.6}$$

where Mw_{app} is the apparent molecular weight by SEC analysis, a is a constant, Mw_{n-mer} is the expected molecular weight of the n-mer and b is the exponent. For the five n-mers observed in Table 2.3, the constant value is 0.65, the exponent is 1.12, and the correlation had an R^2 value >

0.999. This correlation is consistent with the known n-mers of PAO6 and with the typical apparent M_w values for branched molecules in size exclusion chromatography.

Figure 2.5(b) shows the t-test values (ratio of the parameter estimate to its average standard error) for the PAO6 n-mer peak centers and peak areas. The dash-dot line on the graph is the t-test value of an infinite number of data points for which 95% of all populations would have the same mean. The peak center t-test values are an order of magnitude higher than the peak area t-test values. Since the peak area t-test values for the hexamer and heptamer were below the 95% significance line, only the trimer, tetramer and pentamer were considered for partition coefficient analysis.

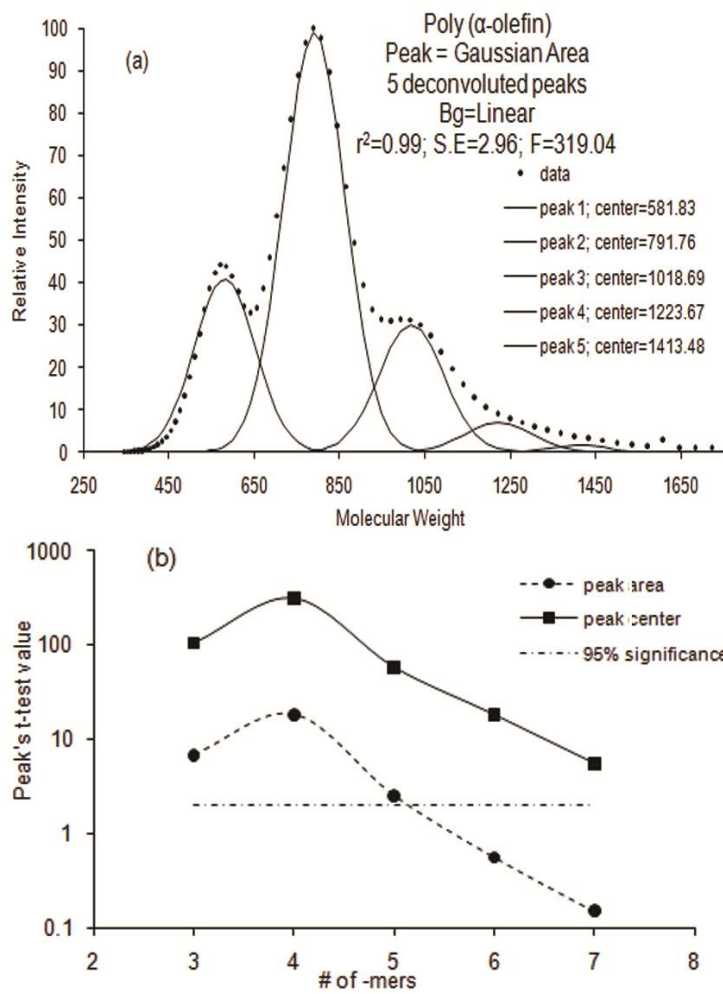


Figure 2.5 Neat PAO6 oligomer data fit to (a) Gaussian area distribution, (b) Peak's t-test values.

2.4.2.3 Poly(α -olefin) in separated phases

The molecular weight distribution of PAO6 in separated phases from a blend of initial volume fraction of 0.179, at 258 K is shown in Figure 2.6. These distributions show the relative oligomer amounts in each phase; the volume fraction of oligomer is determined using the material balance. The bottom phase (rich in PDMS) was enriched in the trimer and lean in the pentamer. The top phase (rich in PAO6) was enriched in the pentamer, and lean in the trimer.

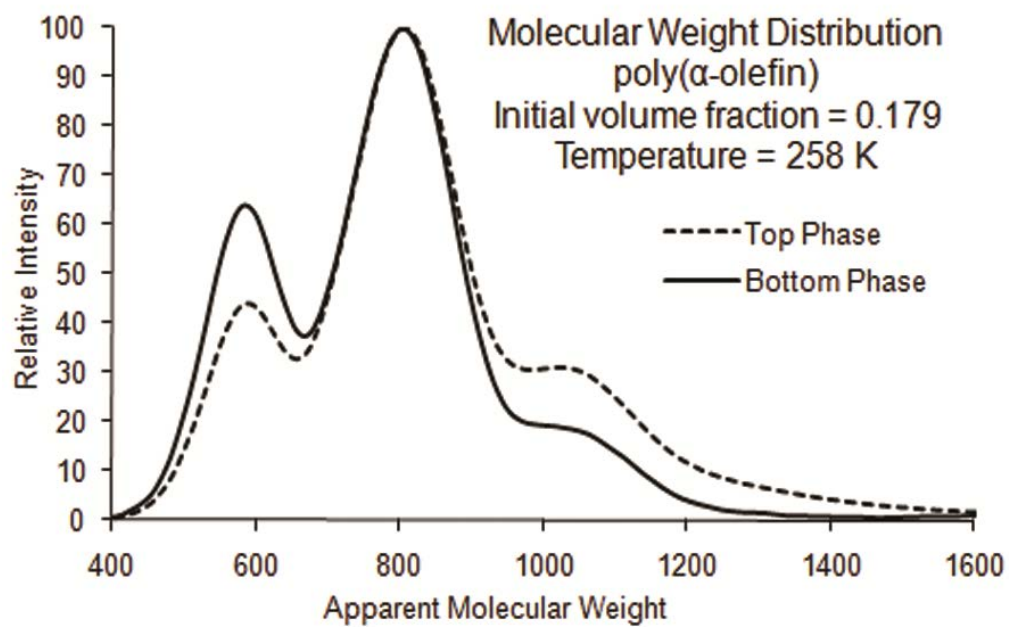


Figure 2.6 PAO6 volume fractions in the top and bottom phases.

2.4.3 Quantitative analysis for PDMS oligomers

2.4.3.1 Identification of PDMS n-mer peaks

The PDMS repeating unit has a molecular weight of 74.08; MALDI-TOF analysis data of PDMS samples with sequential oligomers having the same end groups should have ~74 Da spacing between each sequential n-mer pair. The PDMS sample selected for this study had the molecular weight differential between oligomers that was closest to the theoretical value, and had few 'missing' n-mers in the sequence. Samples from other suppliers were considered, but either had some n-mers missing from the sequence or presented other deviations from the expected molecular weight series.

Figure 2.7 shows peaks from a MALDI-TOF analysis of neat PDMS. The nominal molecular weight of PDMS oligomers with trimethyl silyl endgroups is the degree of polymerization (chain length) times 74.08 plus the molecular weight of the endgroups (88.1 Da). Overlaid on the peaks of Figure 2.7 are a set of bars spaced by 74.08 Da covering the range, 600 Da < Mw < 3000 Da. For sequential oligomers such as this PDMS sample, MALDI-TOF will provide precise differences between the molecular weights of nearby n-mers. Because of the nature of the analysis, additional molecular fragments may be generated, making the peak position different from the precise molecular weight of the n-mer. This set of bars is displaced from the expected n-mer molecular weights ($Mw = n * 74.08 \text{ Da}$) by 55 Da, but it matches peaks over the entire range. The standard deviation between the peak molecular weight and the nominal molecular weight was $\pm 1.06 \text{ Da}$ over the range, 600 to 3300 Da. This differential distribution was used to compute the sample's average molecular weight (1781 Da), which compares well to the manufacturer's reported value (1790, Table 2.1).

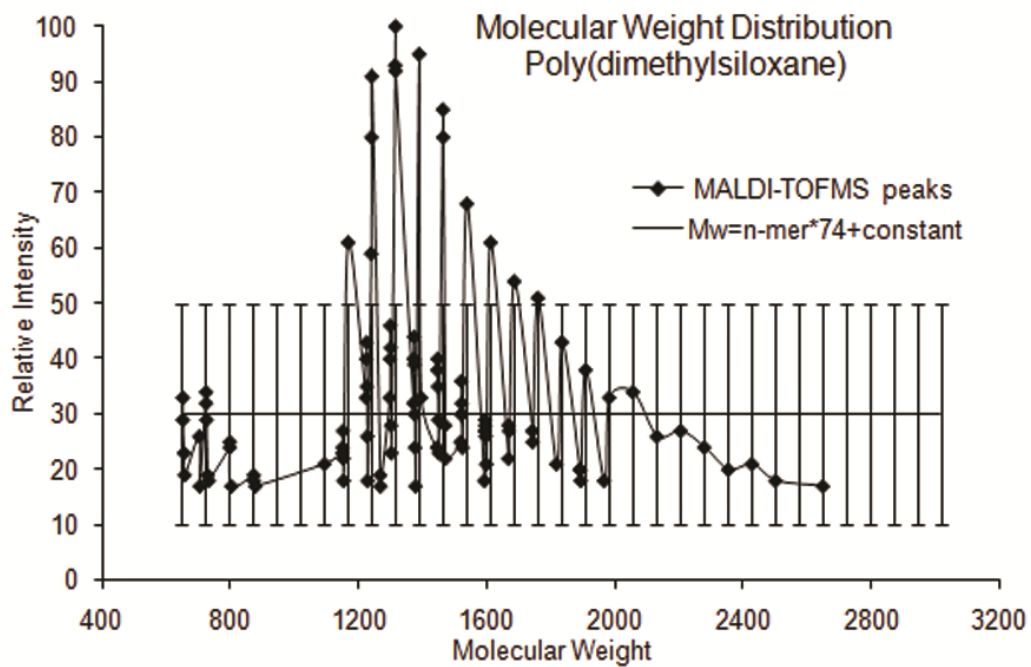


Figure 2.7 Cumulative frequency vs. molecular weight for neat PDMS n-mers.

2.4.3.2 Laser power for spectral quality

Figures 2.8a and 2.8b show the cumulative frequency curves for PDMS oligomer in the top and bottom phases for three replicate samples analyzed with different numbers of laser shots. Trials 1 and 2 were each analyzed with 100 laser shots, while trial 3 used 200 laser shots. While replicate data sets for the 200 laser shot method are not shown, this technique provided very consistent data and the method was used for the PDMS analysis. Figure 2.9 describes the volume fraction of PDMS in the top and bottom phases at 258 K. Less accurate data sets were obtained for PDMS oligomer in the top phase, which typically contained about 8 vol % PDMS compared to 84 vol % PDMS in the bottom phase.

The matrix method [59] has been shown to properly analyze PDMS n-mers in the range, $6 < n < 40$. Oligomers with different chain lengths have similar ionization/desorption probabilities even in the presence of a third polymer. This method provides relative differential distributions of oligomers [59], which, when combined with overall material balances, can be used to determine individual component concentrations in a solution with the assumption of no volume changes on mixing. Other researchers [67-68] have also reported that the MALDI-TOF MS method does not demonstrate sensitivity differences for high mass oligomers. However, for PDMS n-mer chains less than 12 repeating units long [68], there appears to be some sample loss when MALDI-TOF results are compared directly with supercritical fluid chromatography [69]. This reduction does not seem to be associated with PDMS oligomer fragments undergoing metal-catalyzed reactions during the laser ablation process [69]. Since these losses for n-mers with $n \leq 12$ should be similar sample-to-sample, relative differential distributions should not be much affected and were used in combination with material balances to determine PDMS n-mer concentrations in each phase.

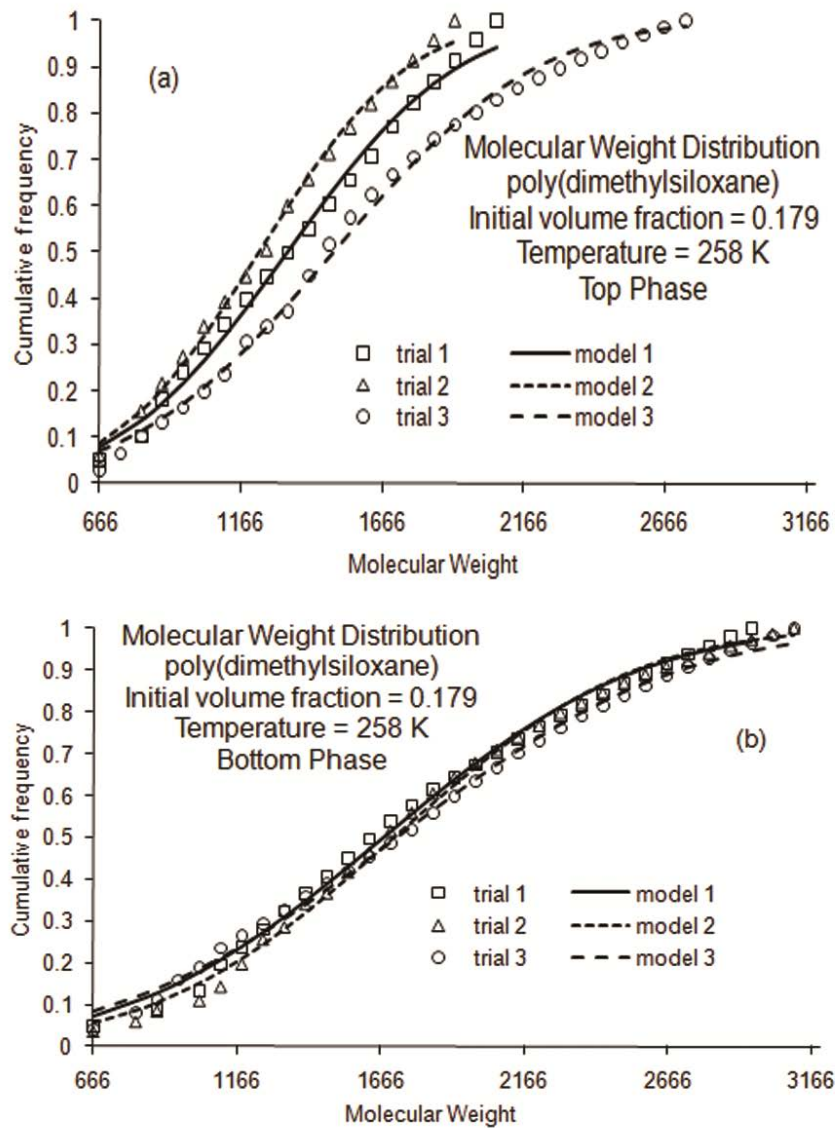


Figure 2.8 Effect of the number of laser shots on PDMS n-mer detection. Cumulative molecular weight distributions of (a) Top phase, (b) Bottom phase.

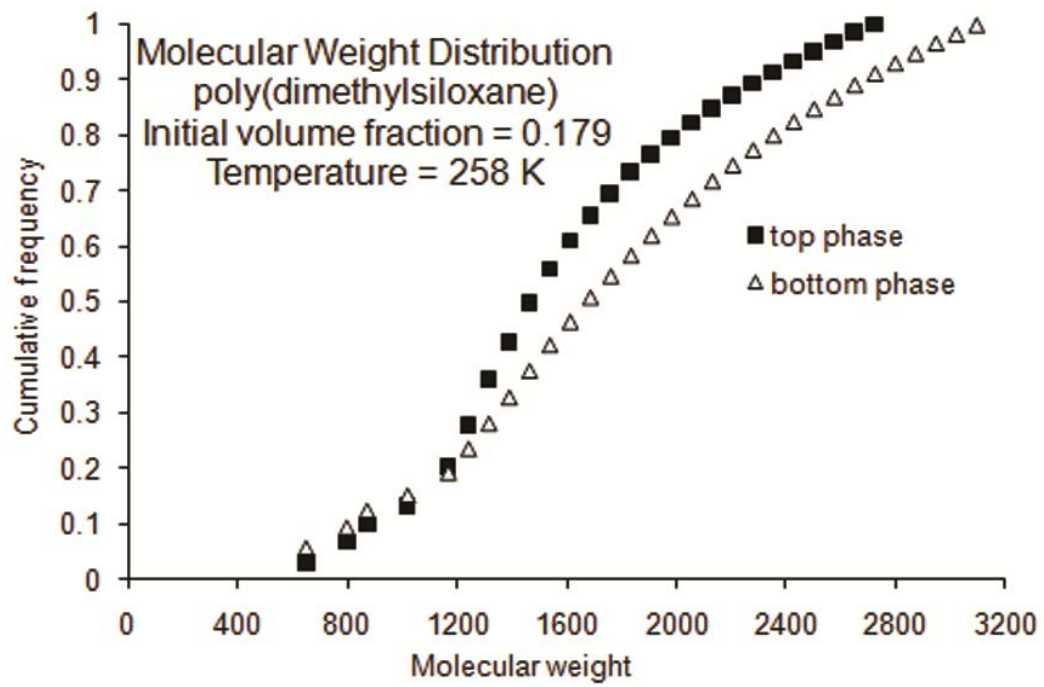


Figure 2.9 PDMS volume fractions in the top and bottom phases.

2.4.4 Overall material balance

2.4.4.1 FT-IR peak selection

The peaks for quantitative analysis of PDMS and PAO6 in separated phases were selected to have minimal interference with each other. The FT-IR absorbance spectra of neat PDMS and neat PAO6 liquids are shown in Figure 2.10, plotted as absorbance vs. wavenumber (cm^{-1}). The solid line spectrum corresponds to PAO6 and the dash line spectrum to PDMS. A blend of the oligomers with 0.179 volume fraction of PDMS is shown as dash dot line. Two distinct peaks were chosen each for oligomer (PDMS: 1257 cm^{-1} - A, 1040 cm^{-1} - B) and (PAO6: 1462 cm^{-1} - C, 2852 cm^{-1} - D). PAO6 oligomer peak at 2852 cm^{-1} , corresponds to the stretching vibration of methyl groups ($-\text{CH}_3$) or methylene groups ($-\text{CH}_2-$). The peak at 1462 cm^{-1} corresponds to the bending vibration of $-\text{CH}_2-$ groups [70]. PDMS has a sharp peak near 1040 cm^{-1} corresponding to symmetrical Si-O-Si stretching [71], while the narrow peak at 1257 cm^{-1} corresponds to asymmetric C-Si-O stretching [72]. Peaks were selected with a high response for the target molecule and a low or non-changing baseline of the other type of molecule. Baselines were established for each peak, and both peak height and peak area were considered for quantitative analysis.

Three spectra were obtained for each volume fraction to check repeatability. It was evident that peak area was better than peak height for quantitative analysis of these oligomers. The calibration curves were nonlinear for either peak area or peak height as the measurand and second order polynomial fits provided the best R^2 (>0.99). Peak A was the best for PDMS oligomer and Peak C was taken to be the best choice for PAO6 oligomer calibration curve.

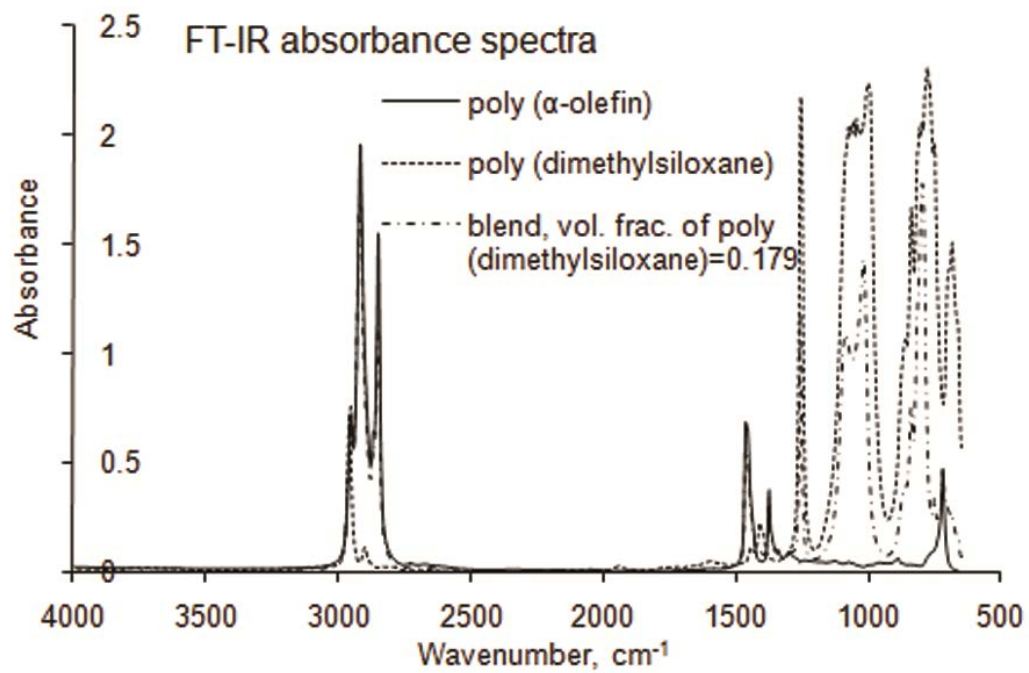


Figure 2.10 FT-IR absorbance spectra of neat PDMS, neat PAO6 and a blend.

2.4.4.2 Material balance evaluations

Phase separated samples (top and bottom) at 233 K, 243 K and 258 K were analyzed via FT-IR. The volume fractions of PDMS oligomer in the demixed samples were obtained through FT-IR quantitation at 1257 cm^{-1} (Peak A for PDMS oligomer through 2nd degree polynomial fit) and 1462 cm^{-1} (Peak C for PAO6 oligomer through linear fit) respectively. The volume fractions of PAO6 oligomer in the samples were then determined by subtracting PDMS oligomer volume fractions from one. All the volume fractions are reported with a 95% confidence interval (± 2 standard deviations) determined through three repetitions in Table 2.4. The most accurate experimental data (analyses of the leanest component in the phase) are shown in italic print, i.e., these data closed the material balance within 5%. For example, the best volume fraction data for the top phase is PDMS oligomer, while the best volume fraction data for the bottom phase is PAO6 oligomer.

Overall and component material balances are needed to determine partition coefficients for the various mixture components. A material balance check was performed for all the three temperatures (233 K, 243 K and 258 K) data to evaluate the accuracy of the characterization techniques chosen. The oligomer volumes in the separated phases were computed by multiplying the volume fractions in each phase with the phase volumes. The difference between the volumes of oligomer used in the mixture to those measured in the separated phases was best (the raw data was evenly distributed about zero) when volume fractions measured by FT-IR were used.

Table 2.4 Phase equilibria data via FT-IR analysis (preferred data in italic font).

Phases	PAO6 (v/v+v)	PDMS (v/v+v)
	Temperature 258 K	
Top	0.746 ± 0.094	<i>0.141 ± 0.008</i>
Bottom	<i>0.083 ± 0.035</i>	0.91 ± 0.331
	Temperature 243 K	
Top	0.834 ± 0.038	<i>0.135 ± 0.004</i>
Bottom	<i>0.084 ± 0.016</i>	0.918 ± 0.083
	Temperature 233 K	
Top	0.876 ± 0.011	<i>0.125 ± 0.005</i>
Bottom	<i>0.087 ± 0.029</i>	0.983 ± 0.191

2.4.5 Partition coefficients

2.4.5.1 Modeling K_{PAO6}

Partition coefficient estimates were based on the data sets with the best closure of overall and oligomer material balances. Figure 2.11 shows partition coefficient estimates for PAO6 n-mers phase separated at three different temperatures, 233 K, 243 K, and 258 K. The partition coefficient, K_{PAO6} , increases as the degree of polymerization increases but is not sensitive to temperature over this temperature range. The fitting coefficients of Eq. 2.4 are $\sigma = 0.395 \pm 0.026$ and $\ln(\xi) = 0.712 \pm 0.118$, with an R^2 value of 0.975. The partition coefficient data for the hexamer are also shown, even though the values of their peak areas by SEC do not meet the quality criteria. In this case, hexamer partition coefficients appear to conform to the simple model. The heptamer data do not conform to Eq. 2.4, but there were wide variations in the partition coefficient values (consistent with the low quality of the peak area data).

Consider the phase equilibria concentrations at a specific temperature, $T=243$ K. Over 99% of the PAO6 n-mers in the mixture are in the top phase. Assuming an extrapolated partition coefficient for the hexamer (Figure 2.10), over 99.8% of this n-mer is in the top phase. By contrast, 79% of the PDMS in the mixture is in the top phase, with the remainder in the bottom phase.

There have been a few articles on the partitioning of oligomers into supercritical carbon dioxide that have developed simple [52] and equation of state models [73-74]. In general, supercritical carbon dioxide is not a good solvent for polymeric oligomers and longer chain lengths have significantly lower solubilities. For example, the partition coefficients for styrene oligomers in carbon dioxide can decrease several orders of magnitude as molecular weight increases from 1000 Da to 2000 Da [52]. The partition coefficients are not particularly sensitive to temperature changes, as the carbon dioxide phase fluid density is not particularly sensitive to temperature. Eq. 2.4 is appropriate for a linear combination of independent, quasi-binary systems of supercritical carbon dioxide with individual oligomers. Eq. 2.4 also seems to be a satisfactory model for the partitioning of the PAO6 n-mers in the mixture.

Eq. 2.4 suggests that the trimer and tetramer have lower values for the partition coefficient. Therefore, a PAO sample enhanced in these components, and depleted in pentamer and hexamer,

should be more soluble than PAO6 in a PAO/PDMS mixture. This hypothesis was easily tested, as PAO4 (Table 2.3) has ~84% trimer, 14% tetramer, and very little higher n-mers. Mixtures of PAO4 in PDMS did not phase separate at temperatures down to 233 K, showing that this simple correlating tool might be helpful in developing mixtures of oligomers with specific phase separation characteristics.

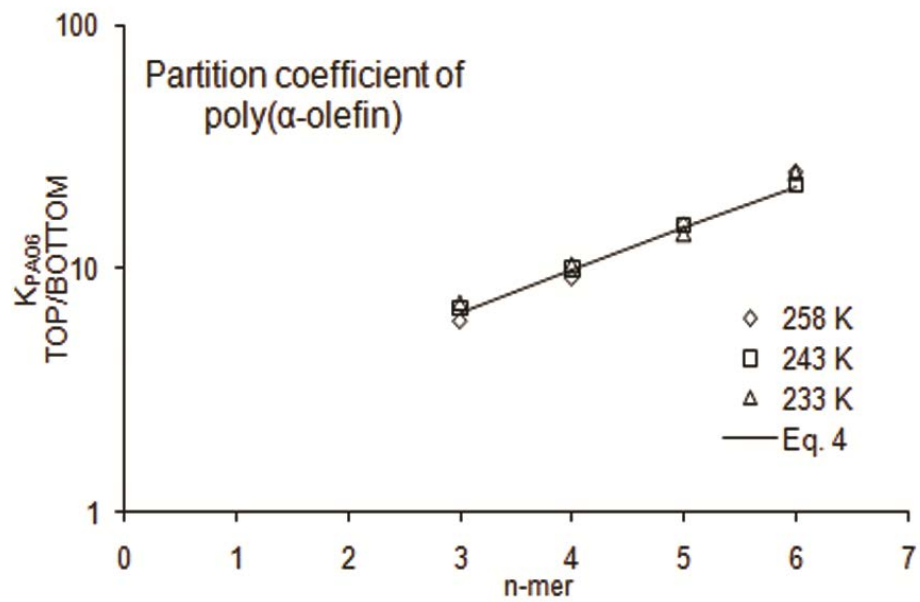


Figure 2.11 Partition coefficient estimates for PAO6 oligomer.

2.4.5.2 Modeling K_{PDMS}

There are examples of supercritical fluid/oligomer partition coefficients that no longer follow a straight line on a log-linear plot of K_i vs. X_i . These include polystyrene in better solvents (ethane and propane) [52] and poly(vinylidene fluoride) in carbon dioxide (a polar polymer in a polar solvent) [73]. Figure 2.12 shows the partition coefficient, K_{PDMS} , of PDMS oligomers components versus molecular weight at 258 K. The n-mer partition coefficients go through a maximum and then decline with as chain length increases for $n \geq 17$. Equation 2.4 is not a good model for this behavior, even for longer chain lengths. The presence of a modest maximum in oligomer partition coefficients has occurred with other systems, such as the phase behavior of PVDF oligomers in carbon dioxide near the critical point [74]. Bonavoglia et al [74] modeled their data with the Sanchez-Lacombe equation of state by allowing the interaction parameter (normally considered to be a constant) to vary with chain length. While empirical, this approach demonstrated that additional terms would be needed in the fitting parameter in order to describe the data.

As K_{PDMS} is computed directly from volume fractions, it is convenient to use the Flory-Huggins approach to model the partitioning between PAO6 and PDMS n-mers. Flory-Huggins theory has been applied to several polydisperse binary and quasi-binary polymer systems, but has been applied to only a few phase-separated polydisperse binary polymer mixtures, e.g., a phase-separated mixture of gelatin and dextran [75]. This system had moderate levels of two polymers in a common solvent. This literature used 5 wt% of each monomer in the mixture for which the n-mer lengths ranged from 500 to 1000. They found that the degree of fractionation (equivalent to the partition coefficients reported here) was a function of n-mer length and that the scaling was well-described by a model similar to Eq. 4 and Flory-Huggins theory. The conventional Flory-Huggins equations for phase separation, written for an n-mer, are:

$$\ln \left(\frac{\phi_{n,\text{pdms}}^T}{\phi_{n,\text{pdms}}^B} \right) = N \cdot \left[\frac{1-N}{N} \cdot \left[\left(1 - \phi_{n,\text{pdms}}^B \right) - \left(1 - \phi_{n,\text{pdms}}^T \right) \right] + \chi \cdot \left[\left(1 - \phi_{n,\text{pdms}}^B \right)^2 - \left(1 - \phi_{n,\text{pdms}}^T \right)^2 \right] \right]$$

Eq. 2.7

Where $\phi_{n,\text{pdms}}$ is the volume fraction of oligomer n-mer in the jth phase, N is estimated using the degree of polymerization, n, (or the molar volume ratio of the n-mer to the 'solvent' phase) and χ_n is

the interaction parameter. The left hand side of Eq. 2.7 is the volume fraction partition coefficient, $K_{in,pdms}$. In this case, Eq. 2.7 can only be considered a correlating tool, as both oligomer systems appear to have chain length-dependent partition coefficients. The values of χ_n for both oligomers show minima with chain length. Components with low values of χ_n usually are interpreted as having better solubility in phase-separating systems. Among the PAO6 n-mers, the tetramer has the lowest value for the interaction parameter, suggesting that it would be most soluble in PDMS. Among the PDMS n-mers, chains with $16 < n < 22$ appear to have a local minima in the interaction parameter, suggesting that this range of n-mers would be most soluble in PDMS. The first of these hypotheses was easily tested, as PAO4 (Table 2.3) has ~84 % of the tetramer. In this case, the Flory-Huggins model does not scale in an analogous fashion to Eq. 2.4, and a more complex model will be needed.

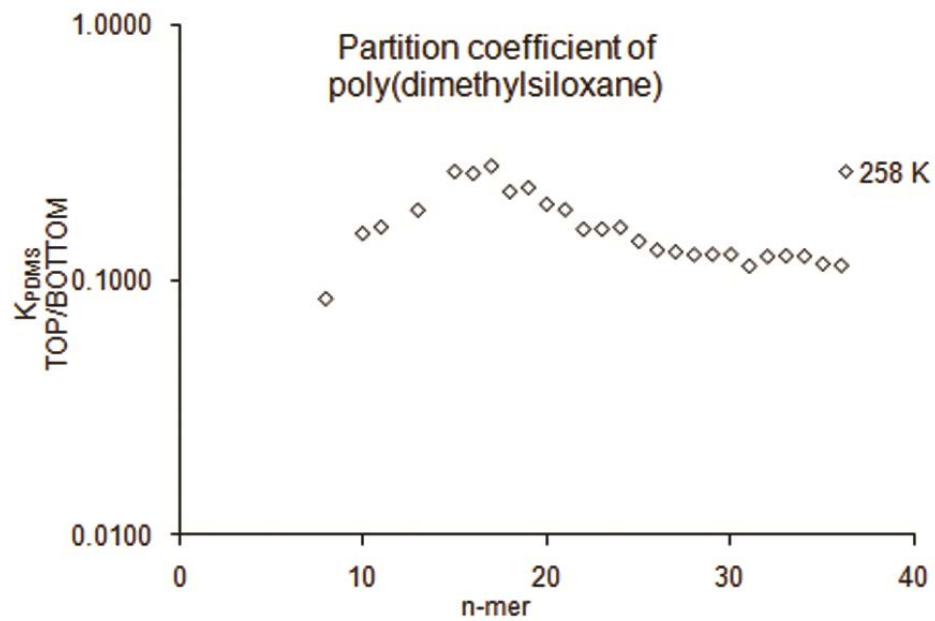


Figure 2.12 Partition coefficient estimates for PDMS oligomer.

2.5 Conclusion

Partition coefficient estimates for individual oligomer components were determined by separate analytical methods for PAO6 (SEC-DRI) and PDMS (MALDI TOFMS), which are linked using overall material balance measurements (FT-IR). Partition coefficients of PAO6 components increased with increasing oligomer components and were relatively independent of temperature. Partition coefficients of PDMS components decreased with increasing oligomer components. For both oligomers, components with high molecular weights were preferentially excluded from the phase rich in the other polymer. The partition coefficient data can be used to develop oligomers with different distribution of component chain lengths that would have different cloud points. This could be done by controlling the oligomer chain lengths during polymerization, fractionating existing commercial materials, adding monodisperse components or via combinations of these methods.

2.6 Nomenclature

$j=a, b$	= Top and bottom phase
$i=1, 2$	= Components of a blend
f	= Fugacity
K	= Partition coefficient
n	= Chain length
N	= Molar volume ratio, often estimated by degree of polymerization (Eq. 6)
P	= Pressure
p	= Polymer (subscript)
r	= Phase volume ratio (bottom/top)
s	= Solvent (subscript)
T	= Temperature
w	= Weight fraction
x	= Mole fraction
χ	= Interaction parameter
Υ	= Activity coefficient
Φ	= Volume fraction
σ	= Separation factor
ξ	= Constant

PAO6	= Poly(α -olefin) oligomer
PDMS	=Poly (dimethylsiloxane) oligomer
MALDI	= Matrix Assisted Laser Desorption/Ionization
TOFMS	= Time of Flight Mass Spectrometer
FT-IR	= Fourier Transform Infrared Spectrometer
ATR	= Attenuated Total Reflectance
SEC	= Size Exclusion Chromatography
DRI	= Differential refractive index detector
THF	= Tetrahydrofuran solvent
DCM	= Dichloromethane solvent
A ₀ , A ₁ and A ₂	= Area, Center and Width: 3 parameters of Gaussian distribution
M _n	= Number based Molecular weight in Daltons (Da)

Chapter 3 Graphite functionalization for dispersion in a two phase lubricant oligomer mixture

This chapter is based on work published as: *Vinod Kanniah*, Binghui Wang, Ying Yang, Eric A. Grulke, *Journal of Applied Polymer Science*, DOI:10.1002/app.35574 (Copyright: Wiley-Blackwell).

Keywords: Dispersions, Oligomers, Thermogravimetric analysis, Hexagonal graphite, Functionalization

3.1 Highlights

- Graphite nanoparticles were functionalized to disperse into each phase of a two phase oligomer mixture.
- A simple and scalable citric acid pretreatment created hydroxyl and carboxyl groups on graphite.
- Different silanes were coupled to the surface citric acid: these surface layers had different water absorption.
- Each functionalized graphite nanoparticle partitioned to the appropriate phase upon separation.

3.2 Introduction

Nanofillers are inorganic nanoparticles, fibers, nano-clays, carbon based material, and other polymers that have one dimension of 100 nm or less. When nanofillers are added to polymer matrices, the resulting composite may have much different mechanical, optical, electrical, magnetic and thermal properties than the neat polymer [1-6]. Nanofluids have nanofillers dispersed in a continuous liquid phase, and may also have significantly different properties than the neat liquid based on the characteristics of fillers added [7]. When the continuous phase is lubricating oil and the nanofiller are thermally conductive solid, the nanofluid has the potential to improve local heat transfer while reducing friction and providing protection from wear. Nanofluids with improved heat transfer have applications in moving mechanical components in metallurgy, machinery, automotives, railroads and thermal systems. Nanoparticles, such as multi-walled carbon nanotubes (MWCNT), fullerene, copper oxide, silicon dioxide and silver, has been used with base fluids (DI

water, ethylene glycol, oil, silicon oil, poly- α -olefin) to produce thermally conductive lubricating nanofluids [15]. This introduction addresses practical factors for developing lubricant nanofluids for improved heat transfer, explains the choice of graphite as the particulate additive, and explains how the surface density of functional groups was estimated.

3.2.1 Lubricant nanofluids

Developing lubricating nanofluids for improved heat transfer remains a significant challenge. Commercial lubricating oils are complex mixtures of base oils and additives intended to reduce friction and protect metal surfaces from wear and corrosion, transfer heat from critical parts and suspend particulate impurities, among other things. As the additives are often dissimilar chemically from the base oils, phase separation is a potential issue that needs to be prevented in oil formulation. A recent article on nanofluids for heat transfer has recognized the importance of colloid stability, phase diagrams and rheology [76]. Should liquid-liquid phase separation occur, it is likely that conventionally dispersed nanoparticles would partition selectively into one phase, reducing the heat transfer properties of the other. Furthermore, there is increasing demand to develop universal base oils that could work over wide temperature ranges.

One approach for developing universal base oils is to combine oligomer lubricants with operating temperature characteristics that complement each other. This approach was explored using a model system, an oligomer mixture with high thermal conductivity nanoparticles for enhanced heat transfer. Graphite was chosen as filler in a dispersion medium of two phase mixture: poly(α -olefin) and poly(dimethylsiloxane). Poly(α -olefin) is commonly used in synthetic lubricant composition as a synthetic lubricant base stock [45]. Poly(dimethylsiloxane) oligomers typically have very low viscosities down to their pour points (generally lower than $-80\text{ }^{\circ}\text{C}$) and have good shear and thermal stability. A 50:50 blend of poly(α -olefin):poly(dimethylsiloxane) oligomers was chosen for this study as it had lower pour points than the neat poly(α -olefin) oligomer. Phase separation occurs at temperatures less than $-15\text{ }^{\circ}\text{C}$. A detailed analysis on the partitioning of this oligomer mixture is reported elsewhere [77]. Oligomer blends of two chemically different materials provide an interesting option for varying lubricant properties for a variety of applications. A critical challenge for such mixtures is controlling their emulsion stability and achieving multiple properties at the same time, thermal conductivity and viscosity in this case.

3.2.2 Graphite dispersion

Graphite particles are dispersed in different media for commercial applications because of their excellent thermal, electrical, mechanical and magnetic properties. Graphite has good thermal conductivity along its basal planes, but much lower thermal conductivity perpendicular to these planes, i.e., across its 'edges' [78]. For high heat transfer coefficients during flow, nanoparticles must be above their percolation limit. In this respect, either disk-like or rod-like particles reach their percolation limits at much lower volume fractions than spherical particles. Uniform dispersions are usually preferred, and can be assisted with functional groups on the nanoparticle surfaces. However, high densities of functional groups on the graphite surface can reduce heat transfer by reducing particle-to-particle interactions.

Commercial graphite is chemically inert and comes in varying sizes. Nano-sized graphite particles can be made using different grinding and milling techniques, but graphite's low coefficient of friction makes these processes slow and inefficient. Bead milling of graphite in fluids can be used to achieve dispersions with long-term stability. The graphite dispersion in this work was achieved by creating reactive groups on the carbon surface, followed by either chemical coupling or use of commercial dispersants. Ultrasonication was used to improve particle dispersion. Functionalization alters the surface of the particle and governs particle dispersion whereas ultrasonication prevents agglomeration and controls particle morphology. Until recently, the only practical functionalization methods reported for graphite involved strong acids or oxidants, similar to the methods used to functionalize carbon nanotubes. Strong acids like H_2SO_4 and strong oxidizing agents like KMnO_4 have been used to create high polarity functional groups on carbon materials [79]. These surface oxidation methods are exothermic and also require extensive post-treatment clean-up, including heating, filtration and washing. Citric acid, a weak organic acid, has been used to create hydroxyl and carboxyl groups on the surface of carbon nanotubes and carbon black [80-81]. It is reportedly used in the functionalization of silica [82-85], titania [86-88] and other metal oxide nanoparticles as well. Citric acid treatment doesn't require complex post treatment. Citric acid has also been used as an acid stabilizer in nanoparticle (alumina, cerium oxide, iron oxide, gold) synthesis [89-92].

3.2.3 Surface group analysis

The number density of functional groups on the nanoparticle ($\#/nm^2$) is a critical characterization of the actual surface “seen” by the solvent. TG experiments, in which water is a leaving group, have been used to estimate the number density of hydroxyl groups on metal oxide nanoparticles. At elevated temperatures, surface hydroxyl groups will undergo condensation, forming a water leaving group and an oxygen bonded to several metal atoms. The number of hydroxyl groups per unit mass of nanoparticles is:

$$\#_{OH} = \frac{2(a/18)N}{b} \quad \text{Eq. 3.1}$$

Where N is the Avogadro's number, a is the weight loss of water during thermal condensation and b is the nanoparticle weight. The specific surface area (SSA) of nanodisks (nm^2/g) can be calculated by Eq.3.2:

$$SSA = \frac{2\pi(rh + r^2)}{\pi r^2 h \rho} = \frac{2(h + r)}{rh\rho} \quad \text{Eq. 3.2}$$

Where r , h and ρ are the radius, thickness and density of nanoparticles. The surface density of hydroxyl groups is equal to the ratio of $\#_{OH}$ and SSA .

Thus the objectives of this work are summarized as:

1. To determine the conditions for controlled etching of graphite (create hydroxyl and carboxyl groups on its surface),
2. To measure the number density of hydroxyl groups before and after functionalization (extent of reaction taking place),
3. To find functionalization pathways to attach coupling agents that enhance the dispersion of graphite nanoparticles in each phase mixture, and
4. To develop functionalized graphite that selectively partition into either poly(α -olefin) or poly(dimethyl siloxane) at phase separation conditions.

3.3 Experimental

3.3.1 Materials

The oligomer base fluid mixture chosen for this study is poly(dimethylsiloxane) (CAS # 42557-10-8, SK96-10, trimethylsilyl endgroups, GE Silicones, USA) hereafter PDMS and poly(α -olefin) (CAS # 68037-01-4, Chevron Phillips Chemical Company LP, USA) hereafter PAO6. Graphite disks (hexagonal graphite with (002) reflection peak and an interlayer spacing of 0.337 nm) [93] were obtained from GrafTech International. Analytical grade granular citric acid monohydrate ($C_6H_8O_7 \cdot H_2O$, Formula Weight=210.14) were obtained from Mallinckrodt Chemicals Inc, USA. N-octadecyltrichlorosilane (CAS # 112-04-9, Molecular Weight=387.93) and amino propyl terminated poly(dimethylsiloxane) (CAS # 106214-84-0, Molecular Weight=3000) were obtained from Gelest Inc, USA. Heptane, toluene and distilled water were analytical grade from Fischer Scientific Inc, USA.

3.3.2 Functionalization

The reaction scheme followed to achieve PAO6-philic and PDMS-philic graphite particles is shown in Figure 3.1(a) and a detailed description in Figure 3.1(b). The first step of the functionalization process was generation of hydroxyl and carboxyl groups on the graphite surface. Two g of citric acid monohydrate was added to 10 ml of distilled water to form an aqueous solution. 100 mg of graphite nanodisks (Sample A) was dispersed into this citric acid solution through ultrasonication at 200 W for 10 min. The dispersion was dried naturally into paste. This paste was heated in the oven at 300 °C (decomposition of citric acid takes place around 250 °C, Figure 3.4) for 30 min. Then it was washed with water (twice) and ethanol (once) to remove any unreacted citric acid. At this temperature, citric acid is liquid and the graphite surface is exposed to a high molar concentration of the oxidizing specie to form a covalent bond through condensation reaction.

Silanes can react directly with the hydroxyl and carboxyl groups created on the nanoparticle surfaces. Hydrogen chloride is a convenient leaving group for this reaction. For synthesizing PAO6-philic graphite, 0.01 moles n-octadecyltrichlorosilane was dissolved in heptane. Sixty mg of Sample B was added into this beaker and stirred at 300 rpm. The mixture was refluxed at 80 °C for 12 h. The product was rinsed with heptane twice to remove the unreacted silanes and dried at 110 °C for 1 h to remove the solvents (Sample C). For synthesizing PDMS-philic graphite, amino propyl

terminated PDMS with 0.004 moles amine groups was dissolved in toluene. 60 mg of Sample B was added into this beaker and stirred at 300 rpm. The mixture was refluxed under 110 °C for 12 h. The product was rinsed with toluene twice to remove the unreacted silanes and dried at 110 °C for 1h to remove the solvents (Sample D).

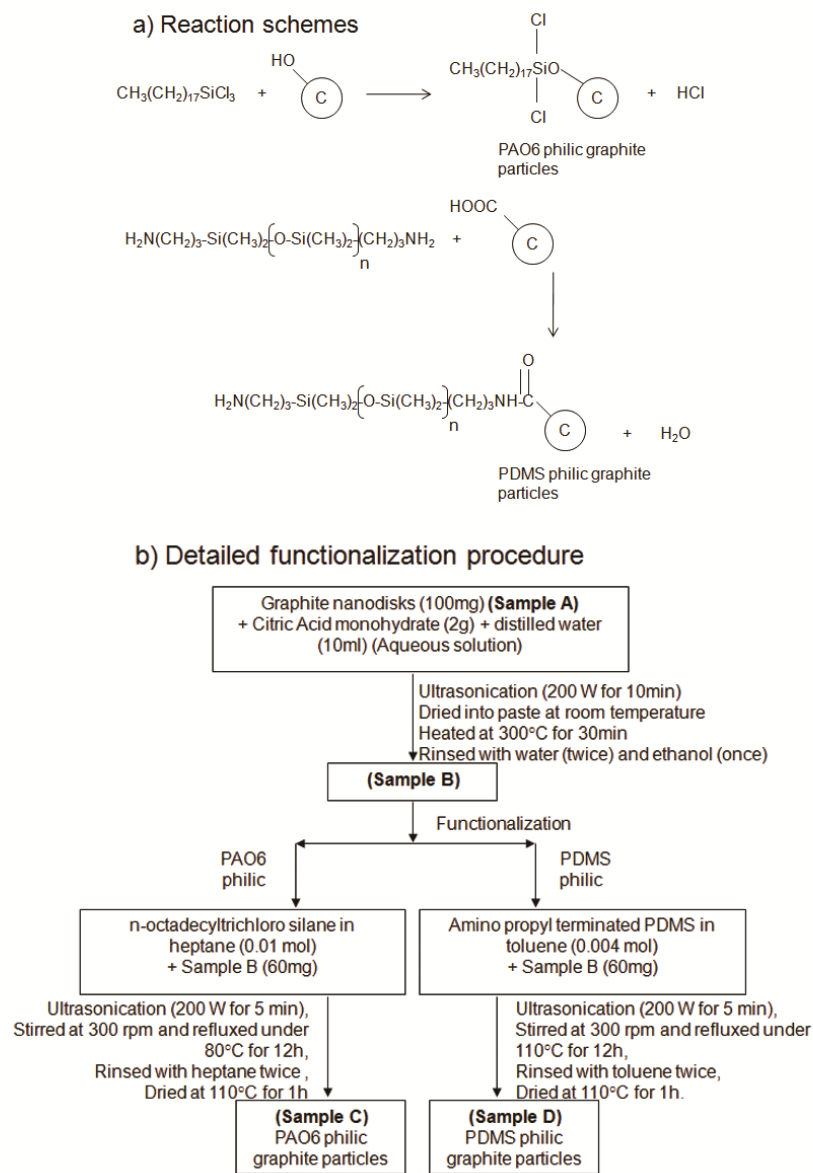


Figure 3.1 a) Reaction scheme for PAO6-philic and PDMS-philic graphite particles. b) Functionalization procedures for PAO6-philic and PDMS-philic graphite particles.

3.3.3 Characterization

Particle morphology, surface functionality, and dispersion are characterized through: Scanning Electron Microscopy (SEM), Fourier Transform Infrared Spectroscopy (FT-IR), Thermo Gravimetric analysis system attached to a Mass Spectrometer (TG-MS) and partitioning images. Since graphite is nonspherical disk-like particles, it is difficult to get accurate particle size distribution information from traditional light scattering devices. Particle morphology of the graphite particles was evaluated using SEM (Model name: Hitachi 3200). The graphite particles were dried at 120 °C for 30 min and placed on a conductive carbon tab which was then put over the specimen stub. The samples were blown under dry air for 3 min before being sputter-coated by Au/Pd. A NEXUS 470 FT-IR spectrometer with an ATR accessory suitable for liquid and powder samples was used to identify the types of chemical bonds on a molecule. The window material was ZnSe with a DTGS KBr detector. Potassium bromide (KBr) was used as pellet packing material for powdered samples. Being purely ionic, KBr displays no absorption peaks over the infra-red region. All the graphite samples and KBr were heated in vacuum oven at 120 °C for 2 h to remove moisture. Three mg of graphite particles and 600 mg KBr were mixed. 100 mg of the mixture was pressed to make pellets. The pellets were also then heated at 120 °C for 5 min to remove excess moisture if any. The pellets were then scanned through 400 cm^{-1} to 4000 cm^{-1} wavelength range.

TG-MS is used to determine the degradation temperature and number density of hydroxyl groups on the surface of nanoparticles before and after functionalization. TG was operated using a continuous flow of helium at 100 ml/min metered at standard conditions of: 10 °C per minute to 100 °C, hold 30 min at 100 °C, 10 °C per minute to 800 °C. Empty pan baseline was subtracted from each TG run to eliminate any baseline variation resulting from buoyancy effects. For mass spectrometry, 0 to 50 amu were scanned using both Faraday and SEM detectors. Partitioning of functionalized graphite was observed by using equal volume two phase mixtures of PAO6 and PDMS. 10 mg of the functionalized graphite particles were dispersed in 6 ml of two phase mixture. The sample was ultrasonicated at 200 W for 3 min and then set inside a refrigerating unit at -18 °C for an hour. Images were taken before and after cooling.

3.4 Results & Discussion

3.4.1 Morphology

Figure 3.2 shows the images so obtained of a) neat graphite, b) citric acid treated graphite, c) PAO6-philic graphite and d) PDMS-philic graphite. The neat graphite disks (Fig. 3.2a, length scale = 20 μm) had an average diameter and thickness of 2.9 μm and 50 nm respectively. These disks dispersed uniformly on the conductive carbon tab, suggesting that there were not strong particle-to-particle interactions. The citric acid treated graphite (Fig. 3.2b, length scale = 10 μm) showed agglomerates with typical dimensions of $\sim 20 \mu\text{m}$, about an order of magnitude larger than the individual graphite particles. Since polar groups have been generated on these nanoparticle surfaces, they tend to self-associate rather than interact with the non-polar carbon tab. The PAO6-philic (Fig. 3.2c, length scale = 5 μm) and PDMS-philic graphite (Fig. 3.2d, length scale = 10 μm) also appear to self-associate, but do not form compact agglomerates as did the citric acid treated sample. The two silane coupling agents, one with alkyl chain and the other with an amine-terminated chain with dimethyl siloxane segments, appear to provide coatings that have altered the surface characteristics. Also, there is a possibility of morphology change due to heat treatment during sample preparations as well.

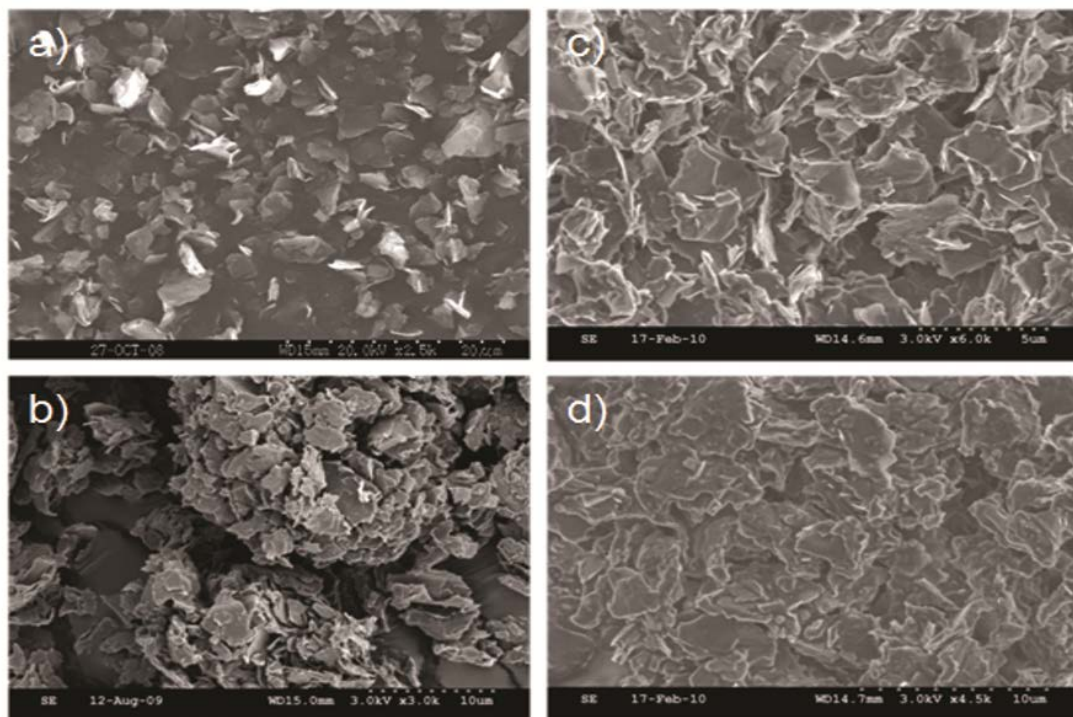


Figure 3.2 SEM images of a) as obtained graphite; b) citric acid treated graphite; c) PAO6-philic graphite; d) PDMS-philic graphite.

3.4.2 Surface groups - qualitative

Fourier Transform Infrared Spectroscopy (FT-IR) was used to certify the functional groups created through qualitative analysis. FT-IR absorbance spectra of neat PAO6 and neat PDMS oligomers are shown in Figure 3.3(a). Neat PAO6 oligomer has double peaks at 2840 and 2910 cm^{-1} , corresponding to the stretching vibration of methyl groups ($-\text{CH}_3$) or methylene groups ($-\text{CH}_2-$). The peak at 1450 cm^{-1} corresponds to the bending vibration of $-\text{CH}_2-$ and the peak at 720 cm^{-1} corresponds to this group's rocking vibration [70]. Neat PDMS has a sharp peak near 800 cm^{-1} corresponding to asymmetric stretching vibration of Si-CH_3 [94]. The sharp peak near 1100 cm^{-1} corresponds to symmetrical Si-O-Si stretching [71], while the narrow peak at 1245 cm^{-1} corresponds to asymmetric C-Si-O stretching [72]. The double peaks at 2890 and 2950 cm^{-1} correspond to the stretching vibration of the methyl groups ($-\text{CH}_3$) attached to each silicon atom in the dimethylsiloxane group.

The spectra of neat graphite, citric acid treated graphite, PAO6-philic graphite and PDMS-philic graphite is shown in Figure 3.3(b). Neat graphite has only modest absorbance in this IR range, with no sharp peaks. Citric acid treated graphite showed $-\text{OH}$ stretching at $\sim 3300 \text{ cm}^{-1}$, which is absent in neat graphite. The peak at 1630 cm^{-1} corresponds to carboxyl groups created by citric acid. PAO6-philic graphite showed a distinct peak at $\sim 2850 \text{ cm}^{-1}$ that corresponds to $-\text{CH}_3$, $-\text{CH}_2$ stretching. The broad peak from 1050 cm^{-1} to 1300 cm^{-1} likely corresponds to asymmetric stretching of C-O-Si , generated by the coupling agent's covalent bonds to the graphite surface [95]. The peak near 3400 cm^{-1} corresponds to hydroxyl groups (not associated to absorbed water since the sample preparation likely minimized water content). This was not expected; rather, we anticipated that the chloro groups on the silane would attach to the surface of the nanoparticles [96]. The presence of hydroxyl groups will be discussed as part of the TG-MS results.

PDMS-philic graphite had a narrow peak at 800 cm^{-1} (asymmetric stretching of Si-CH_3), a sharp peak near 1140 cm^{-1} (symmetrical Si-O-Si), and a narrow peak at 1263 cm^{-1} (asymmetric C-Si-O stretching). These peaks also appear in the FT-IR spectrum of neat PDMS. The peak near 3400 cm^{-1} for hydroxyl groups also appears, as not all surface hydroxyl groups reacted with the coupling agent.

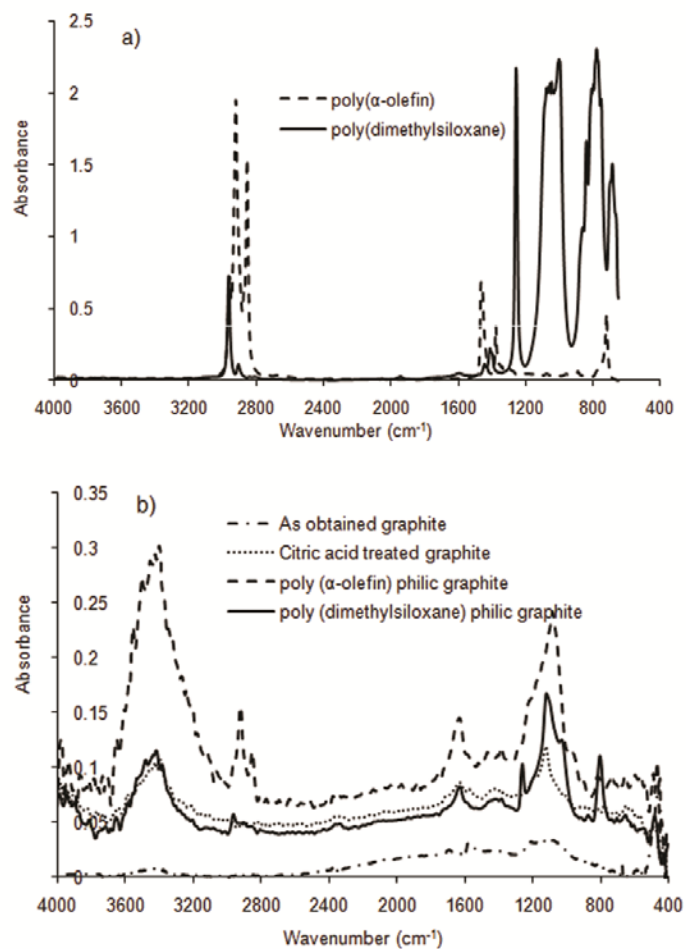


Figure 3.3 FT-IR absorbance spectra of a) neat PAO6 and neat PDMS, b) As obtained graphite, citric acid treated graphite, PAO6-philiic graphite and PDMS-philiic graphite.

3.4.3 Surface groups - quantitative

The TG-MS data were taken under a helium purge. Under these conditions, the stoichiometry of the decomposition products should closely mirror the stoichiometry of the surface groups (citric acid adducts and silane coupling agents). Figure 3.4 shows TG curves of percent weight loss with temperature for neat graphite and citric acid. Neat graphite did not have any significant weight loss until 800 °C because of its high thermal stability. Citric acid melts at ~153 °C and decomposes before it boils, typically in the range of 250 °C. The TG curve for citric acid shows that it is essentially lost at temperatures above 300 °C. Evaluation of differential weight loss curves (TG-DTG) and volatile components identified by mass spectroscopy (TG-MS) can lead to quantitative evaluation of surface groups on nanoparticles. Inverse (negative) peaks in the differential weight loss curves show the temperature range over which the weight loss is occurring, while Figures 3.5, Figure 3.6, Figure 3.7 show such curves for citric acid treated graphite, PAO6-philic graphite and PDMS-philic graphite, respectively. Based on TG-MS, a detailed composition of weight loss for a) neat graphite, b) citric acid treated graphite, c) PAO6-philic graphite and d) PDMS-philic graphite is reported in Table 3.1.

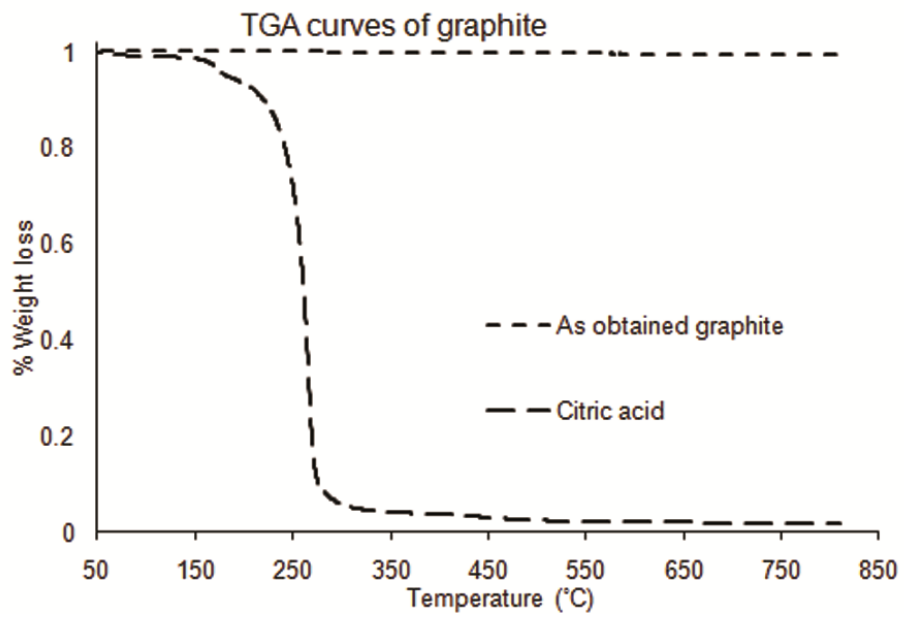
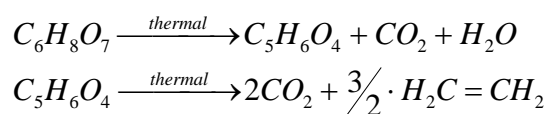


Figure 3.4 TG curves of as obtained graphite and citric acid.

Neat graphite had a minimal weight loss (0.64%), possibly from dehydration and other decomposition reactions, between 100 °C and 750 °C. Citric acid treated graphite (Fig. 3.5a) showed several weight loss events. Absorbed water was lost between 50 °C to 100 °C, with the center of the differential peak at 75 °C. The corresponding mass spectrometric peak (Fig. 3.5b) for atomic mass 18 verifies that water was lost (2.58% weight loss). Additional water is lost between the ranges 100 °C to 300 °C (1.27% weight loss), which was likely due to dehydration reactions. The major weight loss occurred between 300 °C to 750 °C, with the center of the peak near 540 °C. There are a number of possible decomposition products that would depend on the degradation mechanism. If citric acid followed a pathway that generated itaconic acid (plus water and carbon dioxide as intermediate products), which further decomposed to form more carbon dioxide plus ethylene, the observed products would be:



This mechanism is consistent with the atomic mass units observed (18 amu (water), 28 amu (ethylene), and 44 amu (carbon dioxide)). The total amount of weight lost to decomposition products was 15.7%.

The silane coupling agent for PAO6-philic graphite had a long alkane chain (C₁₈). One possible degradation pathway could involve decomposition to ethylene (C₂H₄, amu 28) and/or ethane radicals (CH₃CH₂•, amu 29). If this were the case, then the ratio of ethylene:ethane radicals would be 8:1 based on the octadecane chain. Water could be lost as a dehydration product of hydroxyls on the silicon atom of the silane. For PAO6-philic graphite (Fig. 3.6), the amount of weight loss through desorption of water was 1.27%, less than citric acid treated graphite. This finding is consistent with a functionalization procedure that has created hydrophobic surfaces. However the amount of water formed by dehydration of hydroxyl groups increased to 1.71%. This was not expected since the silane was expected to couple with surface hydroxyl groups. But other researchers using TG to study functionalized titania have also reported higher than expected levels of hydroxyl groups [96]. It could be from the hydrolysis of remaining methoxyl groups in the silane attached on the surface of nanoparticles. A significant weight loss of 25.6% was observed at 520

°C. This peak with amu 29 corresponds to the formation of ethylene free radical ($\text{CH}_3\text{CH}_2\cdot$) from the decomposition of alkane chain created.

For PDMS-philic graphite (Fig. 3.7), the amount of weight loss through desorption of water was 1.28%. This is less than the citric acid treated graphite but the same as PAO6-philic graphite. This means we created hydrophobic surfaces by attaching PDMS chains. There were some dehydration reactions and decomposition of CO-NH at the temperature from 100 °C to 300 °C which led to 2.47% weight loss. It may arise from the decomposition of amide containing tail of the silane. At 530 °C there is a broad peak in DTG and a very sharp decrease of mass (35.6%) in TG-MS associated with the decomposition of PDMS chains. It was the formation of cyclic species from the depolymerization of PDMS [71, 97]. TG-MS results shows there was formation of water (amu 18), CO (amu 28) and CO₂ (amu 44). There is a modest trace of ammonia, but no significant peak associated with its detection.

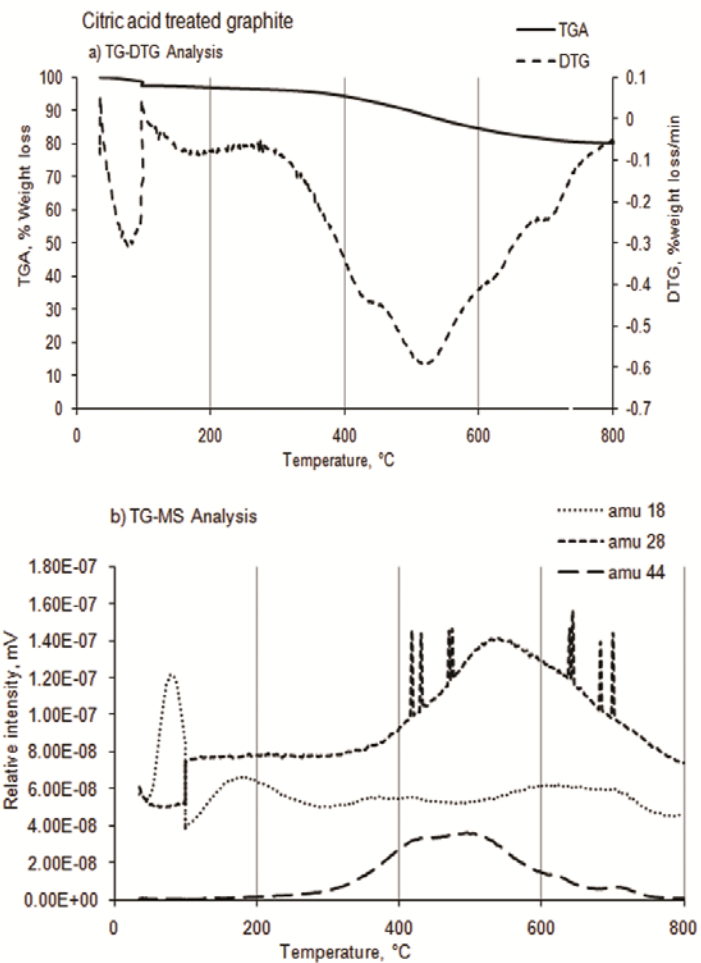


Figure 3.5 TG- DTG curves and TG-MS curves of citric acid treated graphite.

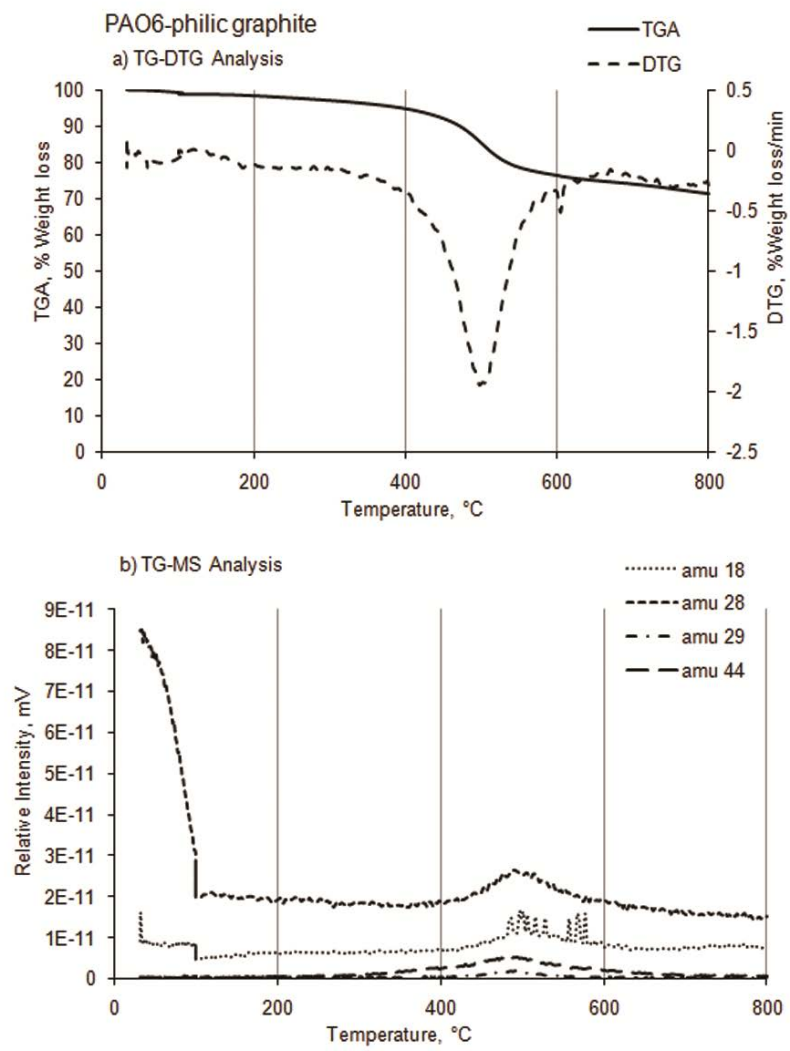


Figure 3.6 TG- DTG curves and TG-MS curves of PAO6-philic graphite.

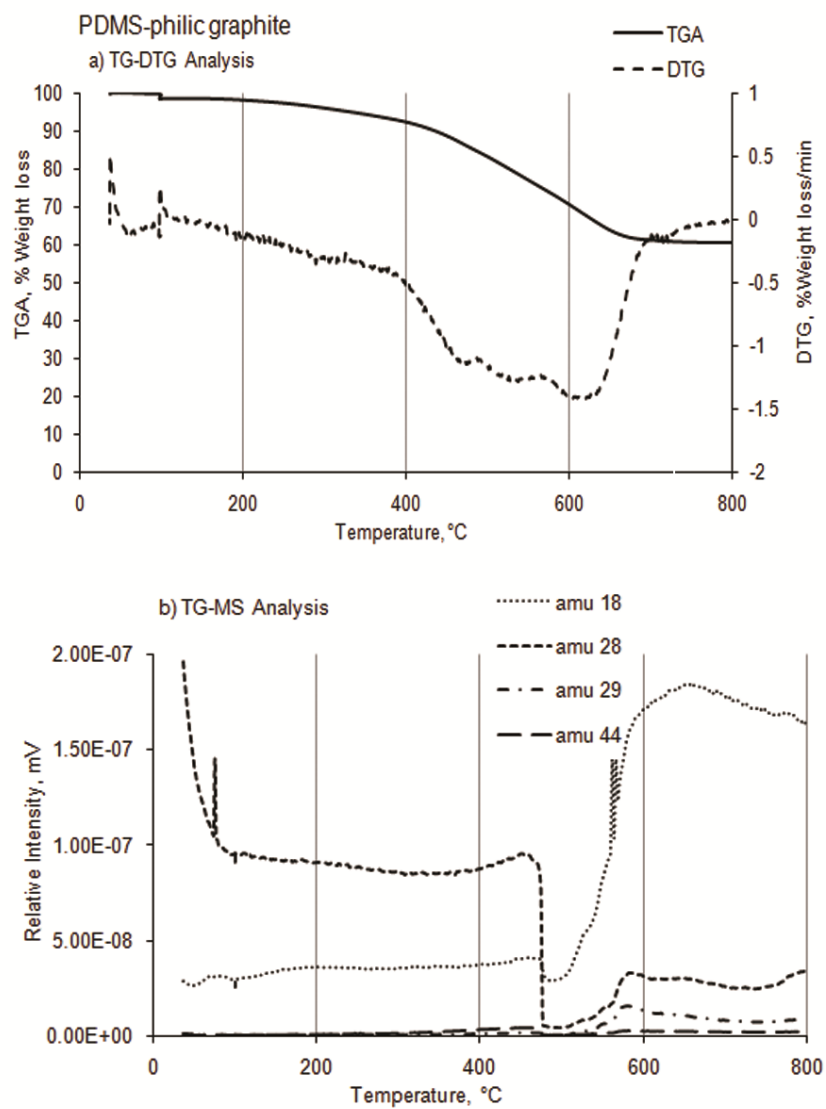


Figure 3.7 TG- DTG curves and TG-MS curves of PDMS-philic graphite.

Table 3.1 Composition of weight loss based on TGA-MS: a) citric acid treated graphite, b) poly(α -olefin)-philic graphite, c) poly(dimethylsiloxane)-philic graphite.

Temp (°C)	DTG peak (°C)	Reaction	TG-MS peak	% Weight loss
a) Plain graphite				
100-300		Dehydration		0.27
300-750		Other decomposition		0.37
b) Citric acid treated graphite				
<100	75	Desorption of water	water (amu 18)	2.58
100-300		Dehydration	water (amu 18)	1.27
300-750	540	Citric acid decomposition	water (amu 18) ethylene (amu 28) CO ₂ (amu 44)	15.7
c) Poly(α-olefin)-philic graphite				
<100	75	Desorption of water	water (amu 18)	1.27
100-300		Dehydration	water (amu 18)	1.71
300-750	520	Decomposition of alkane	ethylene (amu 28) ethane free radical (amu 29) CO ₂ (amu 44)	25.6
d) Poly(dimethylsiloxane)-philic graphite				
<100	50	Desorption of water	water (amu 18)	1.28
100-300		Dehydration Decomposition of CO-NH	water (amu 18) ethylene or N ₂ (amu 28)	2.47
300-750	530 620	Decomposition of PDMS chains [71, 97]	Not evaluated. (amu > 50)	35.6

3.4.4 Surface density of hydroxyl groups

Measuring the surface density of hydroxyl groups is important for tailoring functionalization strategies to meet application needs as well as for post-functionalization characterization of the nanoparticle surface. For many applications, the user will want to know what surface groups are available for attachments or chemical interactions as well as the number of such sites per unit area. After functionalization, it is important to know what surface chemistries have been constructed and which surface groups may still be available for interacting with solvents or other molecules in solution. Key steps of this process are identifying which chemical groups are present, determining at what conditions, i.e., temperature, specific groups are degraded, determining what the decomposition products might be, and then relating specific portions of the weight loss curves to these steps.

For citric acid treated graphite, the total weight loss of water by dehydration reaction is from 100 °C to 300 °C in TG curve. The total weight loss is 1.27%, which is higher than the weight loss of neat graphite (0.27%). Thus, the surface density of hydroxyl groups on citric acid treated graphite and neat graphite are 57.4 /nm² and 10 /nm² respectively (From Eq. 3.1 and Eq. 3.2). This clearly indicates more hydroxyls formed on the surface of graphite nanodisks through citric acid treatment. It is likely that not all of the citric acid carboxyl groups are coupled to the graphite surface. The citric acid coating thickness can be estimated using the weight loss data of Table 3.1 and the density of solid citric acid (1.665 g/cm³) through the simple relation, mass=volume×density. For graphite nanodisks with surface coating, the average original height of graphite disks increases by twice the coating thickness whereas the average original radius of graphite disks increases by the coating thickness. Using the difference in weight loss accompanied with the difference in volume, the coating thickness is determined by direct calculation assuming a uniform thickness on all disk surfaces for each treatment steps (Table 3.2). The citric acid layer is 15.7 wt% of the functionalized particle weight, and has an estimated thickness of 6 nm determined from the mass volume relation. Therefore, it should be difficult to observe in the SEM photomicrograph (Figure 3.2). The molecular diameter of citric acid is in the order of ~0.7 nm [98]; a shell thickness of 6 nm suggests that about 8 monolayers of citric acid are on the particle surface. This estimate is consistent with a partially crosslinked shell of citric acid. The citric acid shell sorbs water at typical lab conditions (~ 16.4 wt%) suggesting that it is fairly hydrophilic.

Table 3.2 Coating morphology.

Coating	Wt% on NP	Wt % of citric acid, (coating thickness, nm)	Wt % of silane (coating thickness, nm)	Total coating thickness, nm	% Water uptake (from Table1)	Surface density of hydroxyl groups, /nm ² (from TGA)	# of monolayers
Citric acid	~16 (15.7)	16 (6nm)	-	6	16.4 (2.58/15.7)	57.4	~8 (6/0.72)
PAO6-philic	~26 (25.6)	16 (6nm)	10 (9nm)	15	5 (1.27/25.6)	87	~3 (9/2.62)
PDMS-philic	~36 (35.6)	16 (6nm)	20 (21nm)	27	3.6 (1.28/35.6)	147	-

PAO6-philic graphite released more water of dehydration, ~1.7%. The surface density of hydroxyl groups calculated from this weight loss is 87 /nm² which is more than the surface density of citric acid treated graphite (57.4 /nm²). This was unexpected since the silane molecule should substitute some hydroxy groups on the surface. Rather, they underwent hydrolysis themselves. This phenomenon was observed in the TG analysis of functionalized titania in literature as well [96] The coating thickness can be estimated using the method described previously. The citric acid treated graphite with the PAO6-philic silane coating is 25.6 wt% of the functionalized nanoparticle weight. Subtracting the loading of the citric acid, the weight loss of alkane chain is 10% (Table 3.2). If we assume that the Si-(O)₃-X group remained on the surface while the alkane part (CH₃(CH₂)₁₇, Molecular Weight=253) decomposed, then the surface density of alkane chains on the surface is 21 /nm² (Eq. 3.2). Closely packed hydroxyl groups on a flat surface would have a surface density of 10-12 (-OH)/nm². If a trifunctional silane group reacted completely, then the surface density of its alkane chains should be ~ 4/nm². Since the surface density of hydroxyl groups on the citric acid treated graphite is 57 /nm², the citric acid coating must be multilayered and contain unreacted hydroxyl groups.

We assume that the silanes react with the outer surface of the citric acid shell. The densities of the citric acid and silane shells are taken to their solid and liquid densities, respectively. Based on these assumptions, the citric acid contributes 6 nm and the PAO6-philic silane contributes an additional 9 nm to the coating (total thickness of 15 nm). However, the silane layer sorbs a much smaller fraction of water (5 wt%) than the citric acid layer, suggesting that it is less hydrophilic. Also, the 6 nm thick citric acid surface coating corresponds to 31 citric acid molecules (mass× *N* /Molecular Weight). The theoretical hydroxyl surface density is 124 /nm² (since 4 hydroxy groups are present in each citric acid molecule) as opposed to the experimentally (from weight loss) determined hydroxyl surface density of 57.4 /nm². This suggests that not all hydroxyl groups on the citric acid-treated surface reacted with silanes. The citric acid coating is probably crosslinked with only half of the actual hydroxyls being available for coupling reaction.

For PDMS-philic graphite, the dehydration weight loss occurred over a temperature region (100 °C – 300 °C) in which the coating was also decomposing. So calculating the surface density of hydroxy groups based on this weight loss gives an overestimate (147 /nm²). Also, above the

dehydration temperature, prior work on the degradation of PDMS in the absence of oxygen has shown that multimer siloxanes are formed, with a six member ring being preferred [71]. At a heat rate of 10 °C/min, the maximum rate of PDMS decomposition occurred at 611 °C [71], similar to 620 °C in this work. The citric acid along with PDMS-philic coating was 36% of the functionalized nanoparticle weight. Unlike PAO6-philic graphite, the decomposition of PDMS chains involves complex mechanism and some compound with Si-O bond may not decompose. It is thus hard to determine the amount of PDMS chains created on the surface. The total coating thickness estimate of 27 nm would include 6 nm attributable to citric acid and 21 nm attributable to the silane. This composite coating absorbed even less water (3.6 wt%) than the PAO6-philic coating. The differences in water sorption by each of these coatings are significant, and suggested that sorption of small molecules might be an effective way to investigate the solvency properties of coatings on nanoparticles.

The number of citric acid, octadecyltrichlorosilane and poly(dimethylsiloxane) molecules per nm² over neat graphite are ~31, ~13 and ~4 in their 6 nm, 9 nm and 21nm coating over graphite. Citric acid has a corresponding sphere diameter of 0.72 nm [98] and octadecyltrichlorosilane has an extended molecule length of 2.62 nm [99]. Thus, the number of monolayers of citric acid molecules on graphite is $\sim 8(6/0.72)$ and octadecyltrichlorosilane chains on graphite is $3(9/2.62)$ (Table 3.2).

3.4.5 Partitioning of functionalized graphite

Partitioning of functionalized graphite particles before and after partitioning in an equal volume PAO6: PDMS oligomer blend at (a) Temp. = 23 °C and (b) Temp. = -18 °C is shown in Figure 3.8. For both Fig. 3.8(a) and Fig. 3.8(b), the left tube has PAO6-philic graphite and the right tube has PDMS-philic graphite particles. At room temperature, the oligomer blend remains miscible as in Fig 3.8(a). In Fig. 3.8(b) as the temperature is reduced to -18 °C: PAO6-philic graphite partitions towards PAO6 in top phase and PDMS-philic graphite partitions towards PDMS in bottom phase. The functionalized nanoparticle disperses uniformly and individually in the PAO6-PDMS blend: there were no agglomerates. This was accomplished by tailoring the silane levels in the coupling reactions to the available hydroxyl groups on the surface. This confirms that the functionalization provides some control over phase separation at low temperatures.

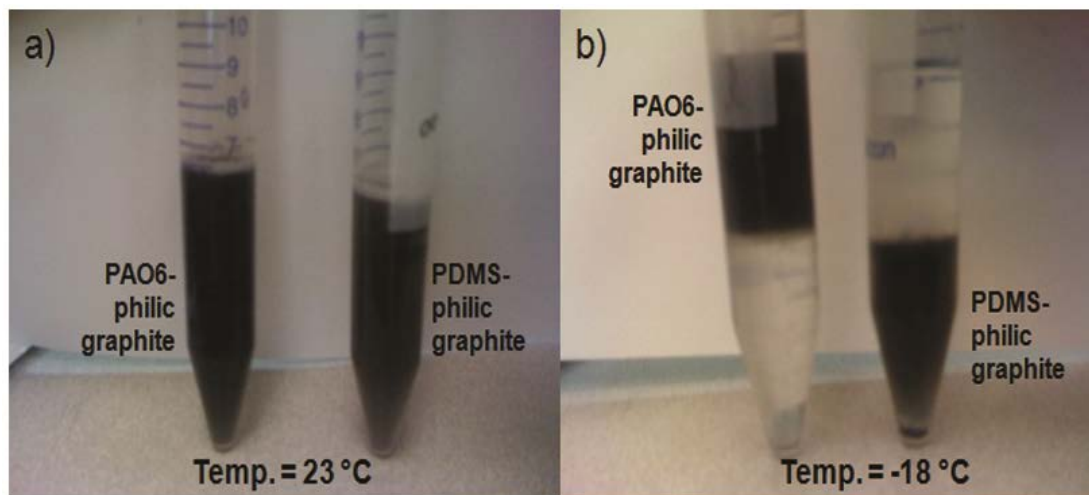


Figure 3.8 Images of the functionalized particles before and after partitioning in an equal volume PAO6: PDMS oligomer blend. (a) Temp. = 23°C and (b) Temp. = -18°C.

3.5 Conclusion

Graphite nanoparticles were functionalized to disperse into each phase of a two phase mixture. A simple and scalable citric acid pretreatment method was used to create hydroxyl and carboxyl groups on graphite surface for functionalization. The etching and silanization processes were not necessarily optimized. The citric acids etch resulted in a 6 nm layer on the graphite surface, greater than a monolayer of this weak acid. Silane levels were tailored to the available hydroxyl groups on the surface, as estimated from TG measurements. Both the PAO6-philic graphite and the PDMS-philic graphite are visible in the blend at room temperature (which is miscible) and partition into the appropriate phase when phase separation occurs at low temperature. All three coatings showed different levels of water absorption, suggesting a method for evaluating the solvency properties of coatings on nanoparticles.

3.6 Nomenclature

N	= Avogadro's number
# _{OH}	= Number density of hydroxyl groups on nanoparticles
a	= Weight loss of water during thermal decomposition
b	= Weight of nanoparticles
SSA	= Specific Surface Area of nanoparticles (nanodisks in this case)
r,h	= Radius and thickness of nanoparticles (nanodisks in this case)
ρ	= Density of nanoparticles
amu	= Atomic Mass Unit
PAO6	= Poly(α -olefin) oligomer
PDMS	= Poly (dimethylsiloxane) oligomer
FT-IR	= Fourier Transform Infrared Spectroscopy
SEM	= Scanning Electron Microscopy
TG	= Thermo Gravimetry
TG-MS	= Thermo Gravimetry Mass Spectrometer
DTG	= Differential Thermo Gravimetry curves

Chapter 4 The effects of surface roughness on low haze ultrathin polymer nanocomposite films

This chapter is based on work submitted as: *Vinod Kanniah*, Thad Druffel, Eric A. Grulke, under review, *Thin Solid Films* (Copyright: Elsevier).

Keywords: RMS, Roughness factor, Haze, Contact angle

4.1 Highlights

- Bidisperse nanoparticle mixtures created structured surfaces on thin films.
- Monodisperse discrete phases created unimodal structure distributions.
- Bidisperse discrete phases created multimodal structure distributions.
- Multimodal structures had maximum heights $\leq 1.5 D_{\text{large}}$ over our variable range.
- Simplified Rayleigh scattering theory linked roughness to haze and contact angle.

4.2 Introduction

Researchers around the world are working to develop hydrophobic/hydrophilic coatings for different applications by modifying surfaces at the nanoscale [100-107]. These efforts mimic those structures found in nature, for example the lotus leaf, which evolved to a surface that efficiently removes dirt. These surface structures offer very significant improvements to surfaces in cleanability and surface drag, especially for products such as eyeglass lenses, displays for consumer electronics, architectural windows, cockpit windows etc., However, some applications require high optical transparency, which can be compromised by high surface roughness. The phenomenon is a combination of a physical and chemical modification of the surface whilst both can be modified somewhat independent of each other. Surface chemistry modifications can provide long-range property change while increased surface roughness can lead to greater hydrophobicity [104, 108]. However, a number of possible systems recently reported in the literature have significant deficiencies, such as: 1) poor adhesion between the applied coating and the substrate, 2) poor mechanical strength of nanoscale three-dimensional structures (example: nanorods grown at angles to the surface to trap air), and 3) less distinct surface structures after chemical manipulation of a rough surface (such as polymer functionalization or surface etching).

Assuming that such technical challenges can be overcome, innovations will still depend on: 1) controlling the surface and the mechanical properties of the ultrathin film, 2) scale-up of complex deposition processes that make them hard to implement for high volume production, and 3) insufficient theoretical understanding of the effects of film morphology on optical properties.

Kim et al [109] generated a composite surface by superimposing large and small particles with radii following a Gaussian distribution on a random Gaussian surface with the centers of large particles sitting on the mean plane of rough surface and the centers of small particles sitting on the superimposed surface of large particles and rough surface. Although they did not deconvolute the probability density functions for roughness on composite surfaces, their results indicate both dual and trimodal type height distributions. Packing fraction and void fraction of bimodal type packing of non-interacting particles is studied by Brouwer [110]. Designed, three-dimensional surface morphology systems might be used in a number of applications. These include: improved adhesion (tissue engineering and self-assembled monolayer stacks), higher surface area for catalysis or photoelectrochemical conversion, changes in apparent contact angle (toward superhydrophobic surfaces), controlled haze levels, and engineered gradients in optical properties near layer interfaces. The focus of this project was to compare recent theoretical methods to simulated and experimental surfaces for transparent ophthalmic lens applications.

The system for the experimental thin film case study consisted of: 1) a uv-cured acrylate polymer and 2) two sizes of silica nanoparticles, each with a monomodal primary particle size distribution. Similar nanocomposite systems, based on unimodal primary particle size distributions, have been used as lens coatings with controlled refractive indices for optical devices [34-35]. The elastic moduli of such ultrathin films have a maximum near 60 volume % of the discrete (nanoparticle) phase [35]; this is similar to the maximum random packing limit for unimodal spheres (62.5 volume % [110-111]). Nanocomposite films on polymer substrates can fail by ductile mechanisms rather than brittle mechanisms as their moduli and thermal expansion coefficients better match those of the substrate [34]. The particular system in this work, silica nanoparticles in a methyl methacrylate matrix, has the advantage of similar refractive indices of the continuous and discrete phases so that haze is primarily due to the surface morphology rather than scattering from the nanoparticles themselves. Mixtures with two different nanoparticle sizes were intended to provide an additional

method for controlling surface morphology and roughness. When the smaller sphere size does not interfere with the packing of the larger one, the total bimodal packing increases, and the void fraction decreases [110]. When the diameter ratio of the large to small sphere size exceeds 7, this condition is approached [111] and the mixture will have maximum random packing limits greater than 62.5 volume %. Such mixtures should have improved mechanical properties due to their lower void fractions. We have used a size ratio of 10:1 in this work as it meets the conditions for high packing densities and there are experimental and theoretical packing estimates for this particular ratio.

We simulated different morphological structures with varying roughness and estimated their haze and water contact angle values. Experimental data on ultrathin optical coatings with controlled surface chemistries and surface morphologies were compared to theoretical methods for comparison to the haze values.

4.2.1 Surface properties

4.2.1.1 RMS roughness

The surface roughness was quantified using RMS roughness (RMS), which is the root mean square average of the profile height deviations taken within the evaluation length and measured from the average height as

$$RMS = \sqrt{\frac{1}{n} \sum (z_i - z_{ave})^2} \quad \text{Eq. 4.1}$$

Where RMS, n, z_i , and z_{ave} are the root mean square roughness, sample size, height of each data point and average height. RMS is the deviations of the peaks and valleys and is the preferred quantity for roughness for optical and philic/phobic properties in coating technologies. The RMS value is much more sensitive to the magnitude of the peaks and valleys than other methods due to the presence of the squared amplitude term in the definition.

4.2.1.2 Contact angle

Contact angle is a fundamental measure of wetting, described as the angle at which a liquid/vapor interface meets the solid surface. The contact angle is specific for any given system and is determined by the interactions across the three interfaces (vapor/liquid, liquid/solid and vapor/solid). Hydrophobicity/philicity are measured by the contact angle of pure water on a clean solid surface, where angles less than 90° are considered hydrophilic and angles greater than 90° are hydrophobic. It is commonly evaluated by the contact angle, θ_y given by Young's Equation [112]

$$\cos \theta_y = \frac{\gamma_{SV} - \gamma_{SL}}{\gamma_{LV}} \quad \text{Eq.4. 2}$$

Where γ_{SV} , γ_{SL} , γ_{LV} are the interfacial free energies per unit area of solid-vapor, solid-liquid and liquid-vapor interfaces, respectively. The above Young's equation was derived assuming smooth surfaces. A century later, Wenzel proposed a model (homogeneous wetting state) for the contact angle measurements of a surface with roughness as [113]

$$\cos \theta_w = r \frac{\gamma_{SV} - \gamma_{SL}}{\gamma_{LV}} = r \cos \theta_y \quad \text{Eq. 4.3}$$

Where r is a roughness factor defined as the ratio of actual surface area of a rough surface to that of a smooth surface having the same geometric shape and dimensions. Wenzel's model assumes a greater interaction between the solid-vapor and solid-liquid phases due to the increased surface area of the solid. Since r is always larger than unity in this equation, it enhances both the hydrophilic/hydrophobic properties of the surfaces [114]. There exists a critical value of r , in which a surface can be influenced into a super hydrophobic or super hydrophilic regime. The roughness factor, r , is influenced both by the shape of the surface as well as the amplitude of the irregularities and is best predicted by the RMS as discussed above.

Surface tension is a property of liquid that allows it to resist an external force and can be measured directly using a surface tensionometer. The surface tension of solids cannot be measured directly

because of the viscoelastic constraints of the bulk phase, which necessitates the use of indirect methods, like critical surface tension from Zisman plots [115]. In this case, a critical surface tension (γ_{sv}) is determined from the contact angles made by the solid substrates with a chosen series of liquids of known surface tension. This value is obtained by extrapolating the plot of the cosine of the contact angle, $\cos \theta_y$, versus surface tension to unity ($\cos \theta_y = 1$) [116].

4.2.2 Optical property

4.2.2.1 Haze

Three essential criteria of transparency are total transmittance (after absorption and reflections), haze (wide angle scattering) and clarity (small angle scattering). For homogeneous materials with smooth surfaces, incident light will either reflect from the surface or be transmitted or absorbed in the bulk material. The reflections from a smooth surface are reflected back at the angle of incidence and the material appears glossy. If the surfaces are rough, the surface structure scatters the incident light resulting in wide and narrow angle scattering. Wide angle scattering reduces contrast and results in a milky or cloudy appearance called haze whereas narrow angle scattering influences the resolution of fine details called clarity. According to ASTM D 1003 standards (Standard Test Method for Haze and Luminous Transmittance of Transparent Plastics), haze is the percentage of transmitted light that deviates from the incident beam by more than 2.5 degree on the average. In this work, we have emphasized haze measurements for optical properties, as it was the most convenient property for characterization and comparison purposes.

Haze can be quantified as a function of RMS of random rough surfaces based on a simplified Rayleigh scattering theory as [117].

$$Haze_T = 1 - \exp\left(-\left[\frac{2\pi}{\lambda}\right] \cdot RMS \cdot C \cdot |n_i \cdot \cos\theta_i - n_t \cdot \cos\theta_t|\right)^2 \quad \text{Eq. 4.4}$$

Where $Haze_T$, λ , RMS, n_i , n_t , θ_i , θ_t and C are the transmittance haze, wavelength, root mean square roughness of the surface, refractive index of incident material, refractive index of transmitted material, angle of incidence, angle of transmission and correction factor respectively. Low haze is achieved in the visible wavelength range (380-760 nm) when surface roughness is less than 80 nm

or higher than a few micrometers [103]. Thus there is a roughness scale at which transparency and wetting properties contradict each other [118].

4.3 Experimental

4.3.1 Film morphologies

4.3.1.1 Simulation of film morphologies

3-dimensional morphological surfaces were created using MATLAB Version: R2008a. Five different surfaces were created and named according to their shapes: Tipped Pyramid, Pyramid, Inverse-Pyramid, Plateau and Hills. Each surface was reproduced on a 5x5 grid leading to 25 structures of each on an (x,y) scale of 100nm x 100nm. The z axis scale was varied 5 times (5, 10, 20, 50, 75 and 100 times the original z value) whilst keeping the lengths of the (x,y) scales the same to obtain 6 different aspect ratios (= Height/base length) for each surface arrangement. In the order, tipped pyramid, pyramid, inverse-pyramid, and plateau, this set of surfaces might represent the transition of a new surface with no wear (tipped pyramid) to a surface with significant wear (plateau). The 'hills' structure has curved surface, perhaps corresponding to less severe wear than the 'plateau'.

4.3.1.2 RMS estimate for simulated surfaces.

The average height of a 3-dimensional surface was obtained by averaging 2-dimensional data. More details are provided in supplementary material. The 2-dimensional deviations of each point on the surface were obtained by subtracting each point from the average height. RMS values for the simulated surfaces were determined by using the simulated heights, z_i , in Eq. 1 and integrating across the square surface matrix. MATLAB code on RMS determination of a 3-dimensional surface is shown in supplemental material.

4.3.2 Measurement methods

4.3.2.1 Roughness of experimental surfaces

Agilent Technology AFM model no. 5500 was used. Tapping mode (or Non Contact mode) with a small area scanner with a magnification range of $10 \times 10 \mu\text{m}^2$ and lower was used for surface profile studies. The scan size was maintained at $5 \times 5 \mu\text{m}^2$ (and 512×512 pixels) for all the substrates. Cantilevers were bought from Budget Sensors with a frequency ~ 150 kHz, force constant, -5N/m , and tip diameter < 20 nm. Gwyddion V2.16, a software tool, was used to process the data

obtained from AFM and obtain meaningful statistical parameters. The data cleaning steps included: plane level to bring inclination angle $\theta=\pm 2^\circ$, correct lines to correct and match height medians, and fix zero to set the average height of the data and set the minimum to zero. Once the data was processed, the statistical parameters were determined for each experimental surface.

4.3.2.2 Analysis of peak height distributions

Raw data of height distributions obtained from AFM were analyzed using statistical software (PeakFit Version 4.12). Data preparation step involved zeroing any negative data responses, normalizing the area under curve, auto baseline correction and smoothening the curve for noise reduction. The data was then deconvoluted based on a Gaussian area model (Eq. 4.5) where A_0 (peak area), A_1 (peak center) and A_2 (peak width) are the three fitting parameters. The maximum percent variation allowed was set to default for parameter estimates. These functions were converged numerically through least squares minimization to obtain parameter estimates.

$$y = \frac{A_0}{\sqrt{2\pi}A_2} \exp\left[-\frac{1}{2}\left(\frac{x - A_1}{A_2}\right)^2\right] \quad \text{Eq. 4.5}$$

4.3.2.3 Haze (theoretical and experimental)

The wavelength of light (λ) was considered constant (550 nm was the wavelength used in our experiments). RMS (Eq.4.1), the angle of incidence (zero), the angle change from transmission (2.5 degrees), and refractive indices of the materials (n_1 =refractive index of air and n_2 =refractive index of material) were used with Eq. 4.4 to obtain theoretical transmitted haze values for different surface morphologies.

Experimental haze was determined using Haze Guard Plus obtained from BYK-Gardner, USA. Three parameters, haze, clarity and transmission, were measured on cleaned substrates to ensure baseline check before applying a coating on the surface. All the parameters were determined thrice for each substrate to ensure repeatability. Haze measurements were the most distinct property for characterization and hence reported here. Clarity and transmission were relatively insensitive to

changes in surface roughness for this system (recall that there should be little scattering caused by the silica nanoparticles themselves due to the close refractive indices).

4.3.2.4 Roughness factor and contact angle

Roughness factor, r , is determined for each surface morphology. For experimental surfaces, AFM data were analyzed using Gwyddion software to get an apparent surface area for the rough surface, which was divided by the smooth surface area. For theoretical surfaces, this can be calculated directly.

As explained earlier, surface tension values of solid substrates (γ_{SV}) could be determined only from indirect methods (like the Zisman plot). Six different solvents, water, glycerol, formamide, ethylene glycol, polyethylene glycol 200, and N,N-dimethyl formamide, were used to measure surface tension. The critical surface tension of a liquid on the substrate is obtained by extrapolating the plot of the cosine of Young's contact angle, $\cos \theta_y$, versus surface tension to unity ($\cos \theta_y = 1$). Measurements were made for a polyacrylate film.

The Young's contact angle was determined using a Goniometer in sessile drop mode. The Goniometer used was Model DSA10, KRUSS, USA. γ_{LV} is the surface tension of water (=72.86 mN/m to study hydrophobic/hydrophilic property of surfaces generated) and γ_{SV} is the interfacial surface energy between the solid and air. Care was taken to ensure that water droplet diameter was maintained the same (~ 1.5 μm) for all the measurements. Five replicates of drop measurements on each sample were taken to ensure accuracy and repeatability.

Young's contact angle (left hand side of Eq. 4.2) was measured using the goniometer. The liquid-vapor surface tension (γ_{LV}) for water is known, as is γ_{SV} for the polyacrylate (39.1 mN/m, measured from Zisman's plot, as composition of the acrylate monomer is larger than the nanoparticle in nanocomposite recipe) so the solid-liquid interfacial energy can be calculated. With θ_y and the roughness factor, known, Wenzel's contact angle, θ_w , can be calculated from Eq. 4.3. AFM measurements provided roughness factors for the real films, and Eq. 4.4 was used to estimate the roughness on the simulated surfaces.

4.3.3 Materials

A nanocomposite (silica-acrylate monomer) model system for roughness generation was spin-coated onto substrates. The acrylate monomers produce a cross-linked polymer binder that, with careful control of concentration, led to films with protruding nanoparticles. Two different size nanoparticles were used to produce surface roughness. Figure 4.1 gives a pictorial understanding on the interdependence of surface parameters (RMS and contact angle) and optical parameters (haze) commonly reported in literature. The top subfigure describes dual sized nanoparticles (100 nm and 10 nm silica) deposited on the substrate. Polymer is not shown but the final nanocomposite films had ~ 30 volume percent silica; the nanoparticles are coated with the polymer, which fills in interstitial space. After deposition of the spinning solution, the polymer was cured with UV light and the solvent evaporated. The polymerized composite is now ready to be characterized for surface and optical properties. The middle subfigure shows typical average height and RMS values. Contact angle is estimated using Wenzel theory and transparency through haze, clarity and transmittance.

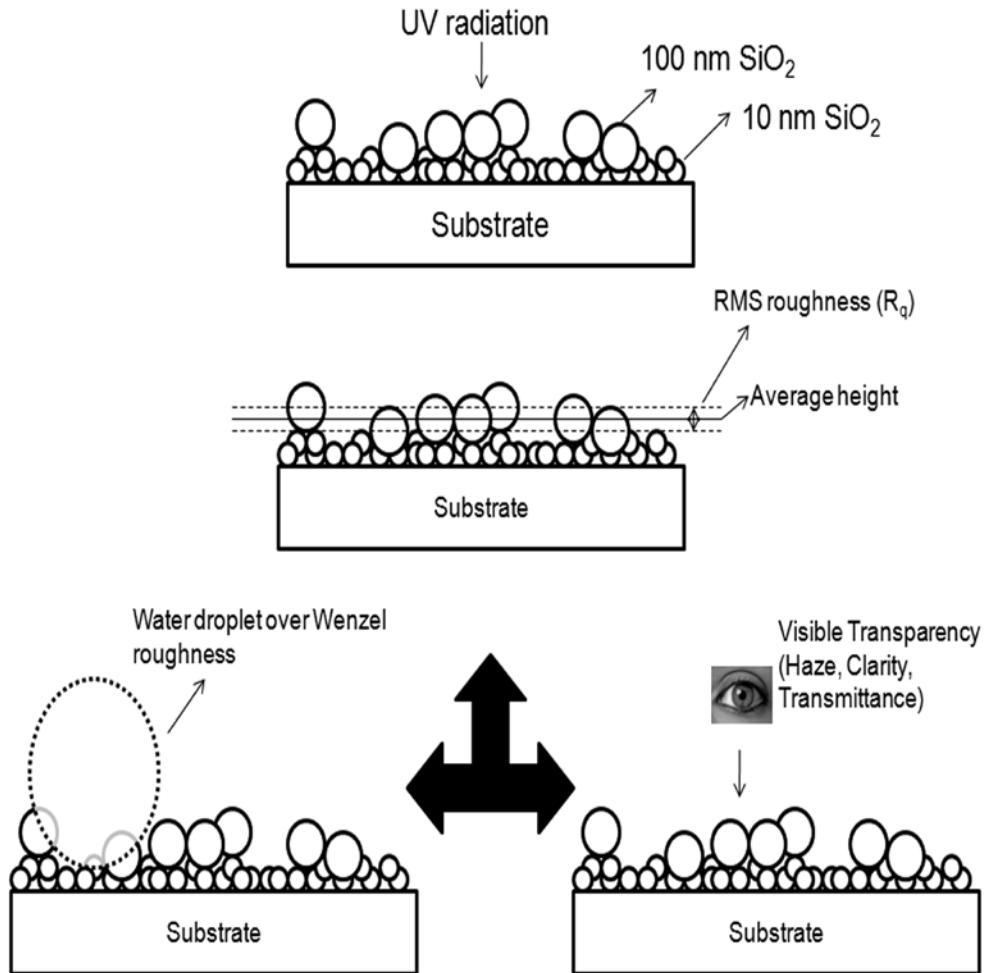


Figure 4.1 Schematic diagrams of dual sized nanocomposite (silica-acrylate monomer) film characterization.

Two different substrates: glass (rigid and hydrophilic) and polycarbonate (flexible and hydrophobic) was chosen to study as base substrates. Precleaned microscopic glass slides, Fisherbrand® were obtained from Fisher Scientific and polycarbonate slides from McMaster-Carr Supply Co., USA. The glass substrates were washed with distilled water, then isopropyl alcohol multiple times and dried overnight at room temperature before the deposition process whereas polycarbonate slides were used as obtained. The deposition technique includes an in-house spin coating apparatus run approximately at 1000 rpm.

The acrylate monomer chosen is dipentaerythritol pentacrylate (DPEPA, product name: SR-399) obtained from Sartomer USA, LLC. It is viscous, abrasion resistance, flexible and has a fast UV curing response to form polymer films. 1-hydroxy cyclohexyl phenyl ketone obtained from Ciba Speciality Chemicals, Inc. was used as a UV curable photo initiator. Silica nanoparticles were chosen as nanofillers: these are simple and widely used nanoparticles in nanocomposites formulations. 10 nm and 100 nm SiO₂ particles in IPA dispersions (30 wt %, Product name: IPA-ST and IPA-STL) were obtained from Nissan Chemicals and their particle size distributions were confirmed through dynamic light scattering (DLS, Model: 90 Plus, Brookhaven Instrument, USA) and electron microscopy (TEM, JEOL 2010 F Transmission Electron Microscopy, Japan).

4.3.4 Nanocomposite film recipes

A typical nanocomposite film recipe consists of solids and solvent by mass. Solids include an organic functional acrylate monomer (SR-399) and 10nm and/or 100nm SiO₂ particles. The solvent chosen for the deposition process is 1-methoxy 2-propanol. The rate of evaporation of this solvent renders a uniform coating of the dispersed particles chosen over the substrates studied. A 3 wt% composition of silica nanoparticles in IPA solvent (Table 4.1 shows the volume fraction of silica nanoparticles in the nanocomposite films) and a 3 wt% composition of monomer in 1-methoxy 2-propanol solvent were prepared. The nanocomposite film materials (nanoparticles and monomer along with solvents) were mixed together thoroughly before been applied to a substrate via spin coating. Once a layer of film is deposited on a substrate, they were UV cured and left for a minute at room temperature for complete solvent evaporation prior to characterization. Since the volume ratio of silica nanoparticles to polymer was 0.30:0.70, the nanoparticles are not close packed and

the polymer may fill in some of the potential void spaces, reducing surface roughness. However, these films were robust mechanically.

Table 4.1 Nanocomposite recipes. D_i = particle diameter; C_i = particle volume fraction; subscript L = large, subscript S = small.

	Sample ID			
	A	B	C	D
D_L/D_S , particle diameter ratio	10	10	10	10
C_L/C_S , particle volume ratio	0	0.134	0.267	0.534
Total silica volume fraction	0.290	0.315	0.340	0.383
Random packing limit, bimodal particle mixtures	0.625	0.637 ^{Ref}	0.659 ^{Ref}	0.701 ^{Ref}

^{Ref} [110, 119-120],

4.4 Results & Discussion

4.4.1 Simulated surface morphologies

In order to understand the impact of irregular surface profiles, we first looked at ordered profiles in the models developed in the previous section. Two-dimensional profiles of different surface morphologies (a) tipped pyramid (or a fresh surface), b) pyramid (or a slightly worn surface), c) inverse pyramid (or a really worn surface), d) plateau (a sharp edge surface) and h) hills (a rounded profile surface)) generated are shown in Figure 4.2. These morphologies are shown at aspect ratios (z/x) of $\frac{1}{2}$, say for the inverse plateau, which is shown at an aspect ratio of $\frac{1}{4}$ for convenience. The plateau and hill morphologies have higher average heights and RMS values because their masses are distributed more evenly along the vertical axis. The inverse pyramid, pyramid, and tipped pyramid morphologies have lower average heights and RMS values. For the same value of the maximum height ($z_{\max} = 10$), the average heights align in the order, plateau, hill, inverse pyramid, pyramid, and tipped pyramid (7/5.5/4.5/3.1/3.0). The three-dimensional RMS values align in the order, plateau, inverse pyramid, hill, pyramid and tipped pyramid (3.75/3.35/3.1/2.41/2.38).

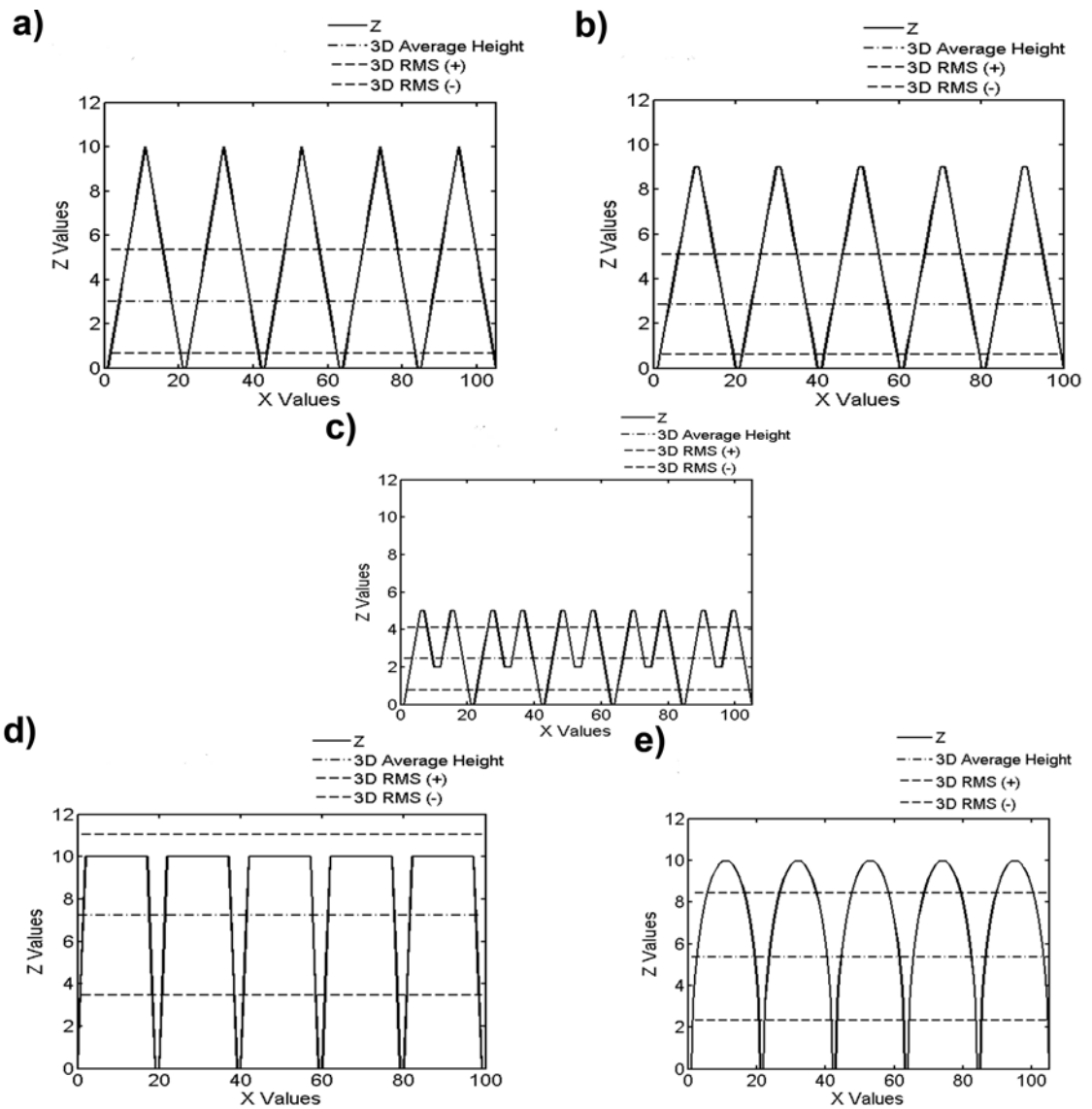


Figure 4.2 Two dimensional profiles of simulated surface morphologies. a) Tipped Pyramid, b) Pyramid, c) Inverse Pyramid, d) Plateau, e) Hills.

4.4.1.1 Effect of RMS and aspect ratio on Haze

Figure 4.3 represents the effect of aspect ratio on RMS for simulated surface morphologies. The RMS values were estimated using 20 nm dimensions for the base of each structure, setting the aspect ratio, and computing the RMS value of the resulting three-dimensional surface. Each structure shows a linear increase in the RMS as the aspect ratio increases.. The slopes of the linear models shown in Figure 4.3 align in the order of the RMS values reported above. This order roughly corresponds to the area normal to the surface available for light reflection. If we think of a wear event that would cause the structure to be modified in the sequence, /tipped pyramid/pyramid/inverse pyramid/plateau, the worn structure would lie on different RMS vs aspect ratio lines as the process progressed. However, the absolute aspect ratio would be reduced as well.

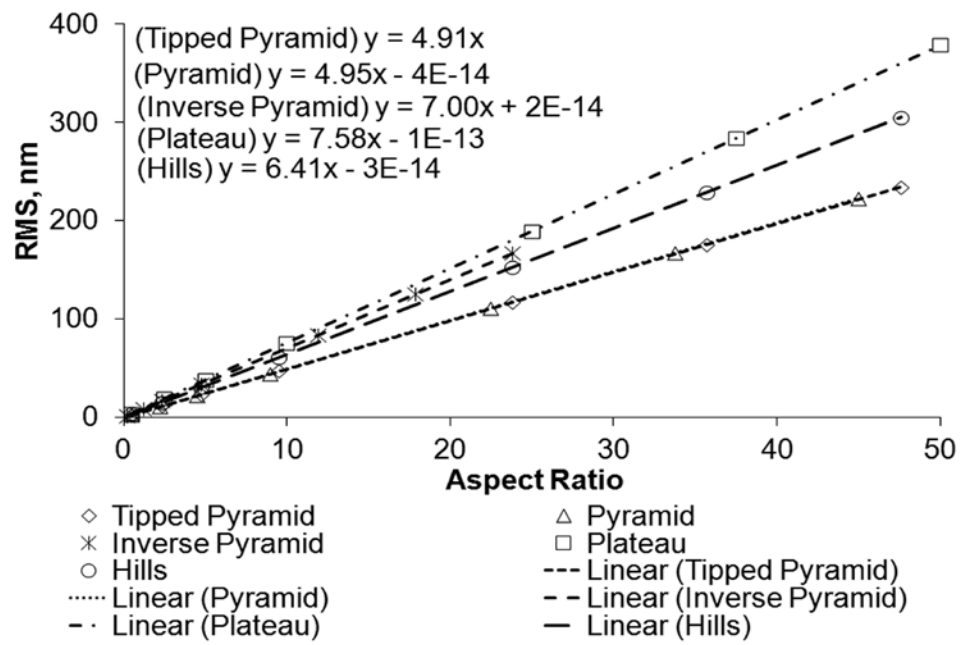


Figure 4.3 Effect of simulated surface morphology aspect ratio on RMS.

Figure 4.4a shows the effect of RMS of simulated surface morphology on haze (wide angle scattering). Eq. 4.4 was used to estimate haze (transmission) for the structures in Figure 4.2, giving the data points in Figure 4.4a. Figure 4.4b shows haze (transmission) as a function of aspect ratio of the different simulated structures. An empirical equation has been generated to link the haze estimates with aspect ratios of the simulated surfaces. The haze estimates were correlated using an equation similar to Eq.4.4 as: $Haze_T = 1 - \exp(-AR \times \Delta)^2$, where AR refers to aspect ratio and Δ is the parameter estimate that varies for each surface profile. As before, the pyramid ($\Delta = 0.026$) and tipped pyramid ($\Delta = 0.0257$) curves are quite similar. A tipped pyramid had the lowest delta estimate of 0.0257 followed by pyramid (0.026), hills (0.0336), inverse pyramid (0.0367) and plateau (0.0397).

The simulated surface architectures would provide large RMS values, which would help achieve high values of the Wenzel contact angle (needed for superhydrophobicity properties). However, this characteristic would also result in high values of haze, which would negatively affect the transparency of the surface structures. Since we wanted to achieve low haze ultrathin optical films with improved hydrophobic/hydrophilic properties, we made experimental surfaces with comparatively lower RMS values as described in the following section.

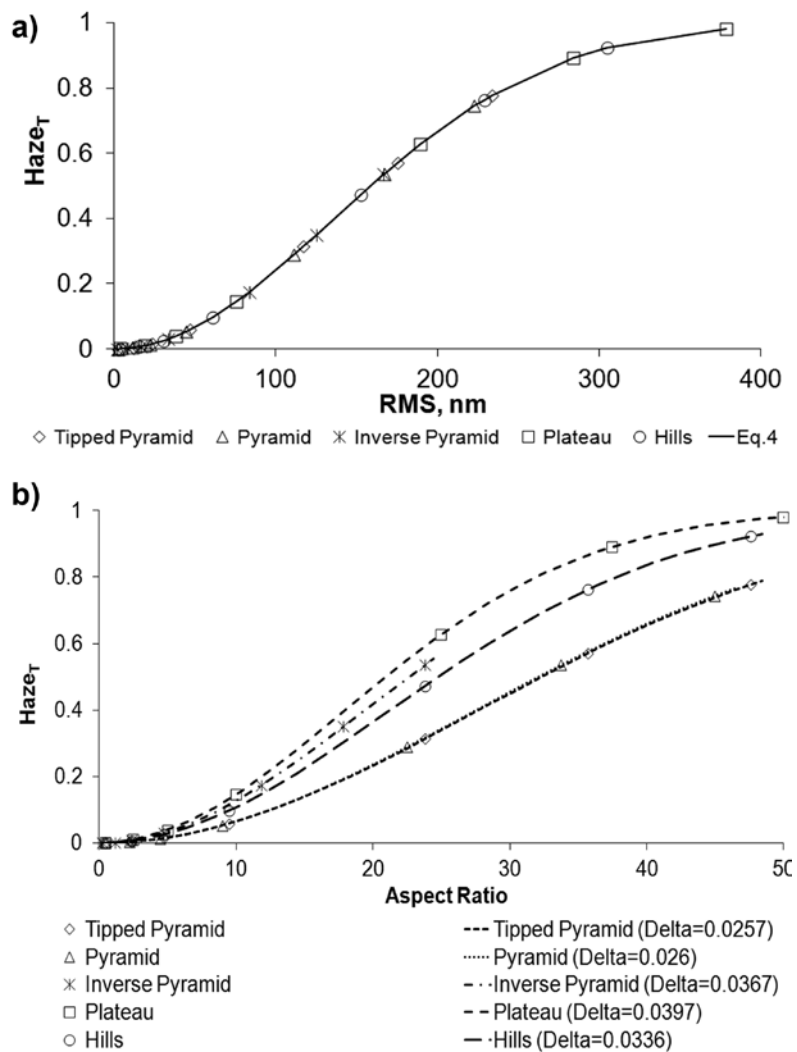


Figure 4.4 Effect of simulated surface morphology on Haze_T. a) Haze_T vs. RMS; b) Haze_T vs. aspect ratio.

4.4.2 Morphology of dual sized silica nanocomposite films.

4.4.2.1 Silica nanoparticles

The particle size distributions of the 100 nm and 10 nm silica nanoparticles are shown in Figure 4.5. Figure 4.5a shows the 100 nm silica particles (scale bar = 500 nm) whereas Fig. 4.5b shows the TEM image of 10 nm silica particles (scale bar = 20 nm). Figure 4.5c compares the TEM particle size distributions with DLS data. Data from both the sizing methods were fit to a log normal distribution. DLS results provide hydrodynamic size and TEM gives primary particle size details. Log normal distribution of 10 nm silica nanoparticles from TEM was comparatively wider because of size counting issues associated with overlapping observed in small sized particles. The particle size distribution of the SiO₂ nanoparticles showed near unimodal distribution and an averaged particle size as claimed by suppliers.

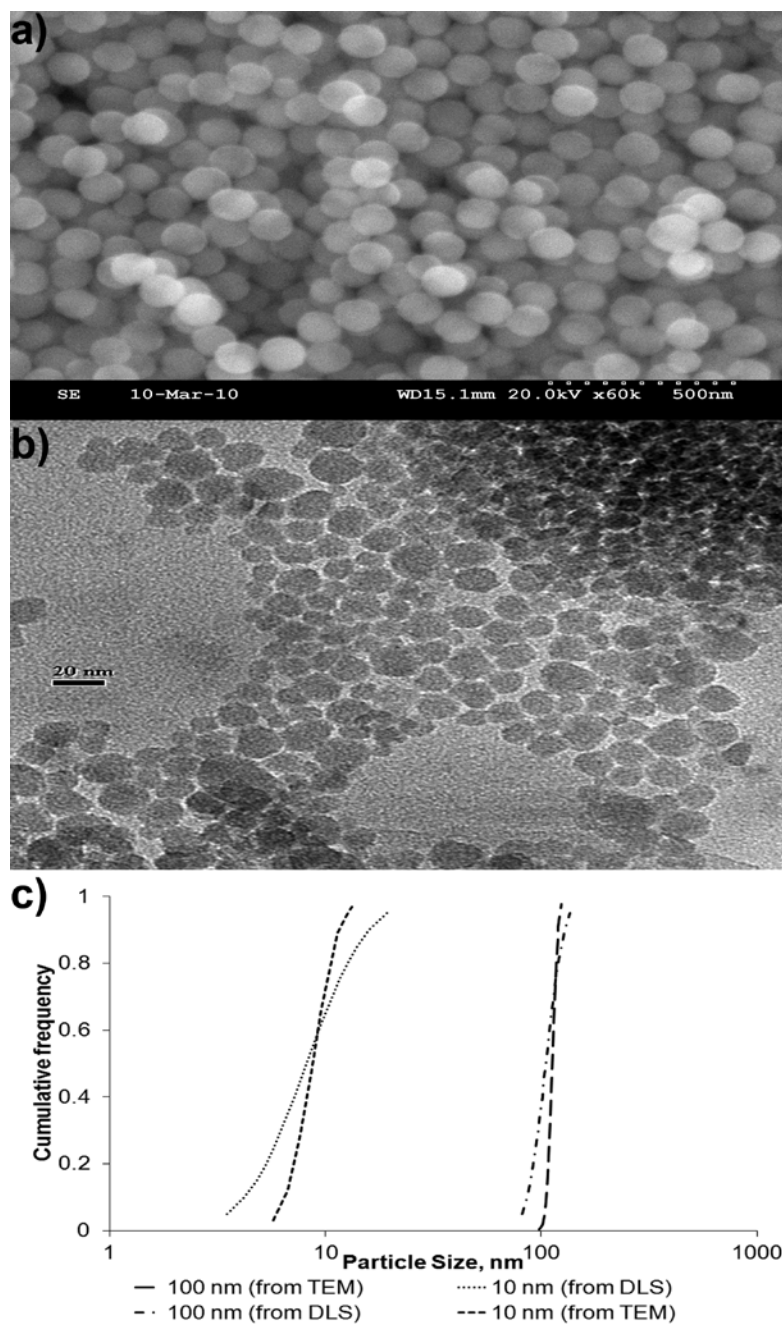


Figure 4.5 Primary particle size distributions of silica nanoparticles. a) TEM of 100 nm silica. b) TEM of 10 nm silica. c) Comparison of particle size distributions by TEM and DLS.

4.4.2.2 Film surface roughness

The average RMS and haze values for the experimental films prepared are shown in Figure 4.6. The RMS values for unimodal silica nanocomposites on both substrates are small: 4.4 nm for glass and 5.5 nm for polycarbonate surfaces. As the weight fraction of the 100 nm silica nanoparticles increased, the RMS values of the films increased. In general, the RMS values for films on the glass substrate were slightly less than those for films on the polycarbonate substrate. The haze (transmission) measurements showed trends similar to the RMS measurements: haze increased with increasing 100 nm silica weight fraction and the films on the polycarbonate substrate had slightly higher values than those on the glass substrate. The haze value of ~ 0.02 (0.5 wt fraction 100 nm silica) is probably on the higher end for acceptable high quality, high transmission films on an optical device and hence not shown in Fig 4.6.

AFM 3-dimensional roughness profiles of the nanocomposite films on hydrophilic substrate (glass) and hydrophobic substrates (polycarbonate) provide additional information about the surface morphologies (Figure 4.7). Both neat substrates had low RMS values. The nanocomposite films with 10 nm silica particles only (samples A for both substrates) had similar film heights spans (~ 40 nm and ~ 56 nm). The RMS value for this material on the hydrophilic substrate was slightly lower than that for the hydrophobic substrate. With the addition of 100 nm silica, the film height spans increased to the range of ~ 130 nm (samples B, C, and D; both substrates). Haze also increased for the dual sized nanocomposites. The nanocomposite films on the hydrophobic substrates had higher values of RMS and haze (transmission), suggesting that, for ultrathin nanocomposite films, the underlying surface may influence nanoparticle packing structure/morphology [33].

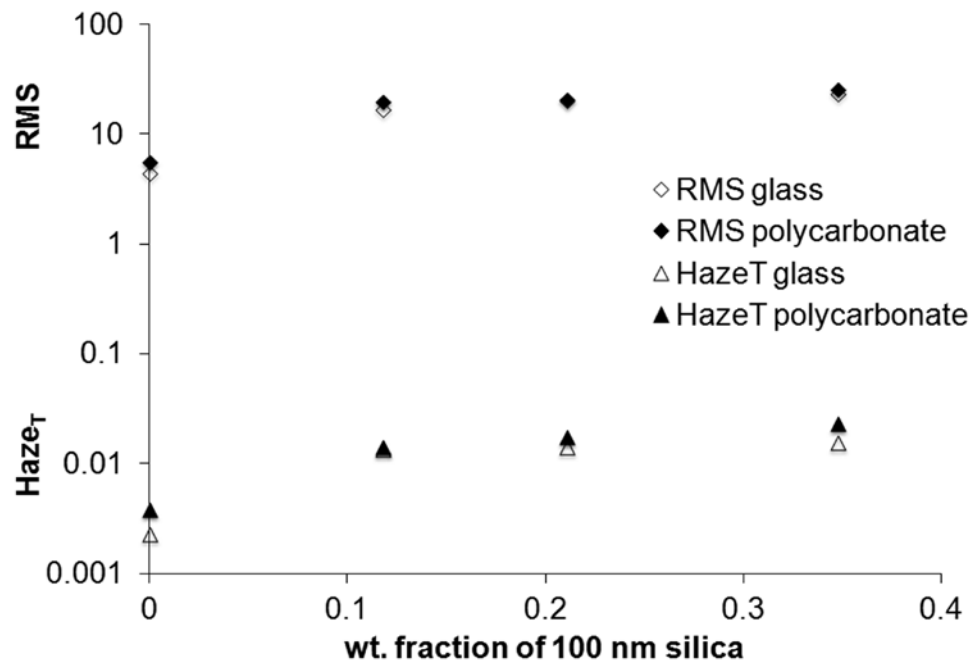


Figure 4.6 RMS and Haze_T vs. 100 nm silica weight fraction.

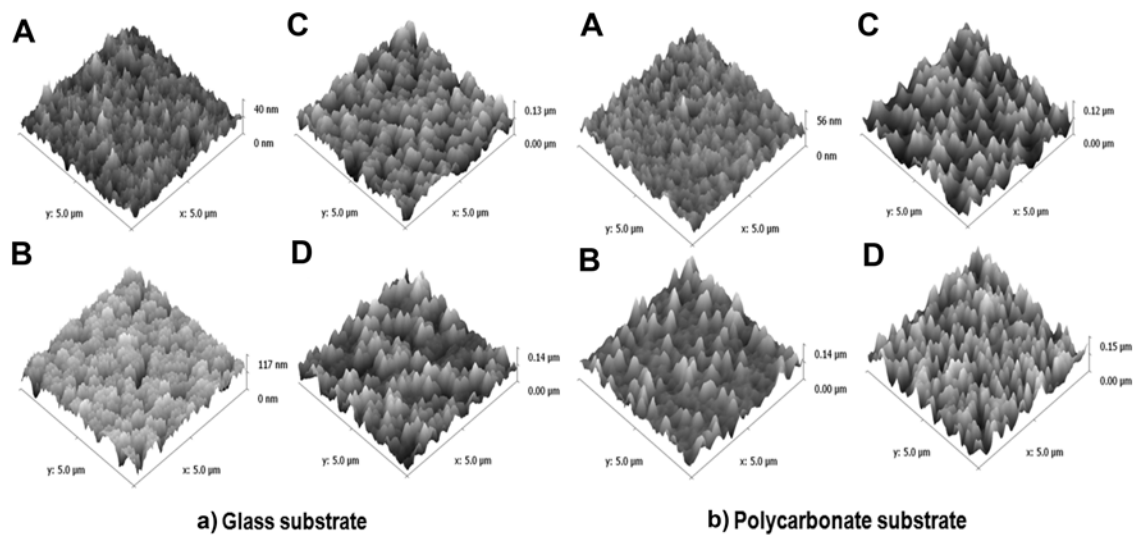


Figure 4.7 AFM 3-D roughness profiles of nanocomposite surfaces. a) Hydrophilic (glass) and b) hydrophobic (polycarbonate) substrates. Nanocomposite recipes (A-D) of Table 1.

4.4.2.3 Analysis of height distributions

Height distributions of surface A and B on glass and polycarbonate substrate are shown in Figure 4.8a and 4.8b. Each surface was deconvoluted for peak identification beneath the distribution; peak modes and size range, peak coefficients for Eq. 4.5 (area, center and width), R^2 , F-values and t-test values are shown in Table 4.2. The lower limit of peak heights was taken to be two standard deviations below smallest peak center; the upper limit was taken to be two standard deviations about the largest peak center. Deconvolution quality was good as indicated by $R^2 > 0.99$ and $F > 7000$ for all cases. The RMS values for the 10 nm silica nanocomposite films were factors of 3-4 greater than those of the substrates. In all cases, increasing the volume fraction of large silica nanoparticles increased the RMS values.

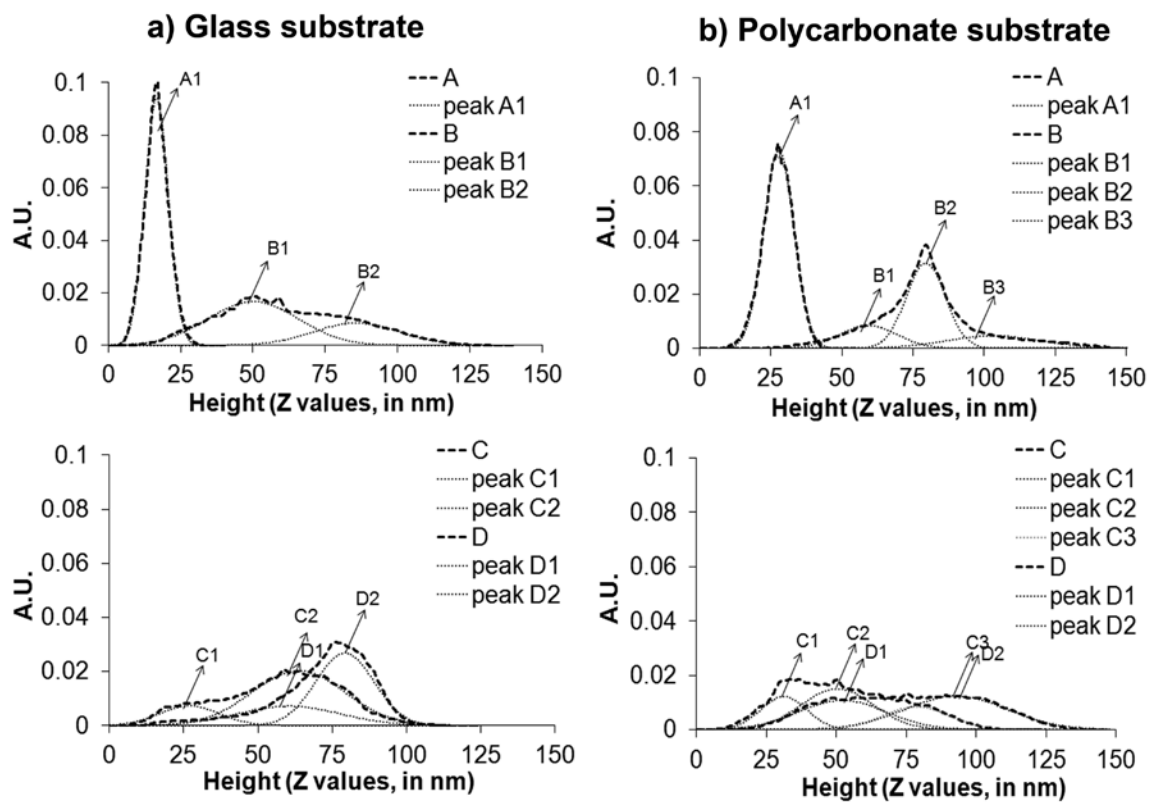


Figure 4.8 Peak deconvolution of AFM surface height distributions. a) Glass substrate, A-D. b) Polycarbonate substrate, A-D.

Table 4.2 Peak deconvolution of height distributions. Peak modes with size range.

Surfaces	Peak modes (range), nm	Peak area (A ₀)	Peak center (A ₁), nm	Peak width, (A ₂) nm	R ² accuracy	F value	Peak center's t-test values
Glass A	Unimodal (8 - 24)	0.96	16.7	4.1	0.99	58500	1240
Glass B	Bimodal (19 - 116)	0.65 0.31	50.1 85.7	15.6 15	0.99	8440	147 136
Glass C	Bimodal (8 - 96)	0.14 0.84	25.1 62.7	8.7 16.8	0.99	11300	129 645
Glass D	Bimodal (26 - 99)	0.31 0.65	60.3 79.2	17.3 9.8	0.99	17100	27.2 923
PC A	Unimodal (17 - 38)	0.98	27.7	5.35	0.99	194000	2800
PC B	Trimodal (39 -136)	0.22 0.52 0.21	59.6 79.5 102	10.3 6.7 17.2	0.99	7060	99.6 814 63.2
PC C	Trimodal (17 - 103)	0.16 0.61 0.2	31.1 49.1 80.1	7.2 15.4 11.3	0.99	11500	220 94.7 170
PC D	Bimodal (21 - 129)	0.42 0.56	52.1 92.7	15.7 18.2	0.99	9870	150 261

4.4.2.4 Nanocomposite films on glass and polycarbonate

The RMS value of the neat glass surface was 0.76 nm; the nanocomposite coating containing only 10 nm silica (A) had an RMS value of 4.4. The peak distribution showed one unimodal peak centered on a height of 16.7 nm, i.e. the average peak height, Z_{ave} , was about 1.7 times the nanoparticle diameter, D_{small} . The maximum peak heights observed, Z_{max} , were about 3 times D_{small} . Sample B still had a relatively flat surface with few sharp features, as shown in Fig. 4.7a, with a broad distribution of peaks (Fig. 4.8a). Sample C appears to have more distinct peaks than Sample B (Fig. 4.7a) and the distribution shifts toward a high fraction of tall peaks. Sample D appears to have the most distinct peaks (Fig. 4.7a) with a further shift toward a large fraction of tall peaks. The deconvolution of Samples B-D all showed bimodal peak distributions. For the bimodal mixtures, Z_{ave} varied from 0.35 D_{large} to 0.84 D_{large} while the maximum peak heights observed, Z_{max} , were about 1.25 times D_{large} .

The RMS value of the neat polycarbonate surface was 1.5 nm; the nanocomposite coating containing on 10 nm silica (A) had an RMS value of 5.59 nm with a unimodal peak centered at a height of 28 nm, i.e. the average peak height, Z_{ave} , was about 2.6 times the nanoparticle diameter, D_{small} . The maximum peak heights observed, Z_{max} , were about 4 times D_{small} . This surface is relatively flat with few features greater than 38 nm from its base. Sample B has a significant fraction of high peaks (Fig. 4.7b), with ~ 50% of these structures centered near 80 nm in height. Sample C appears to have a more even peak distribution than B (Fig. 4.7b and 4.8b). Sample D also has an even peak distribution with further broadening of the modes (Fig 4.8b). Samples B and C appear to have trimodal distributions while Sample D is best described by bimodal distributions. For the bimodal mixtures, Z_{ave} varied from 0.31 D_{large} to 1.0 D_{large} while the maximum peak heights observed, Z_{max} , were about 1.5 times D_{large} .

The surface morphologies of nanocomposite films on the two substrates appear to be different. In the case of the glass substrate, adding more large nanoparticles gives films with increasing fractions of tall structures. In the case of the polycarbonate substrate, the lower amount of large nanoparticles gave a distinct peak near 80 nm, but increasing the amount of large nanoparticles resulted in a broadening of the peak distribution. Since the RMS values of the two surfaces are about two orders of magnitude lower than the peak heights of the nanocomposite films, it does not

seem likely that the substrate surface differences contributed to the differences in nanocomposite surface morphologies. Rather, the differences in surface chemistry may be a controlling factor.

4.4.2.5 Wenzel's contact angle vs. r

The nanocomposite surfaces appeared similar to the tipped-pyramid morphology: these data are compared here. The relation between roughness factor, r , and aspect ratio of a tipped-pyramid simulated surface morphology is linear. For a tipped-pyramid surface, the estimated rough surface area is $4 \times 1/2 \times (\text{height} \times \text{base length})$ while the smooth surface area is $(\text{base} \times \text{length})^2$. Six aspect ratio surfaces were simulated and their corresponding roughness factors were determined. The roughness factor increases linearly with aspect ratio for tipped pyramid surfaces.

Since the volume fraction of polyacrylate in the nanocomposite film was larger than the volume fraction of nanoparticles, the surface of the film is polymer, and the surface energy of acrylate monomer ($\gamma_{SV}=39.1 \text{ mN/m}$) was used for Wenzel's contact angle determinations for both the experimental and simulated surfaces (tipped-pyramid). For the experimental surfaces made, the roughness factors were $1 < r < 1.07$, and the calculated Wenzel's contact angle varied from 98.9° to 99.5° . The cosine of Wenzel's contact angle is plotted versus roughness factor for the experimental surfaces and simulated tipped pyramid surfaces in Figure 4.9. The maximum contact angle possible for the tipped pyramid simulated surface was 179.2° ; at this condition, its r is 6.41 (plotted as a cross marker in Figure 4.9) and its aspect ratio is 4.76. The experimental surface data and the simulated tipped pyramid surface data are well-represented by the same line.

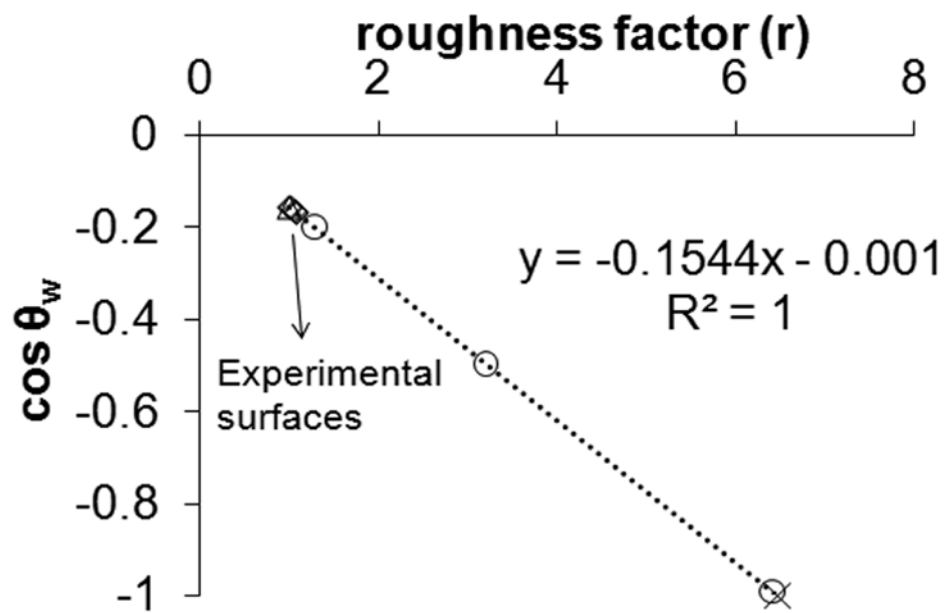


Figure 4.9 Effect of roughness parameter (r) on cosine of Wenzel's contact angle ($\text{Cos } \theta_w$) for tipped-pyramid simulated surface and experimental surfaces.

4.4.3 Comparison of nanocomposite and simulated surfaces.

Theoretical haze values computed from the measured RMS values are compared to the measured haze values in Figure 4.10. Eq. 4.4 (single Gaussian model) is presented as a continuous curve while the dual Gaussian model ($Haze_T = 1 - \exp[-(4\pi \times RMS \times C \times \Delta n / \lambda)^3]$) where C is the fitting parameter and Δn is the refractive index difference [117], is shown as a dashed curve. The data for both nanocomposite substrates are shown as points. In general, Eq. 4.4 represents the data well over this range of RMS values with the measured haze values usually being greater than the predicted values. Haze values for the films on polycarbonate substrates appear to increase consistently with the theoretical values. As shown in Fig. 4.7 and 4.8, these films were multimodal and broadened as more 100nm silica was added. Measured haze values for films on the glass substrate appear to scale differently from Eq. 4.4 as more large nanoparticles are added. The peak distributions of the films on glass broadened as well, but migrated toward larger peak heights as more 100nm silica was added. These differences suggest that subtle changes in nanocomposite surfaces may have measurable effects on their haze properties.

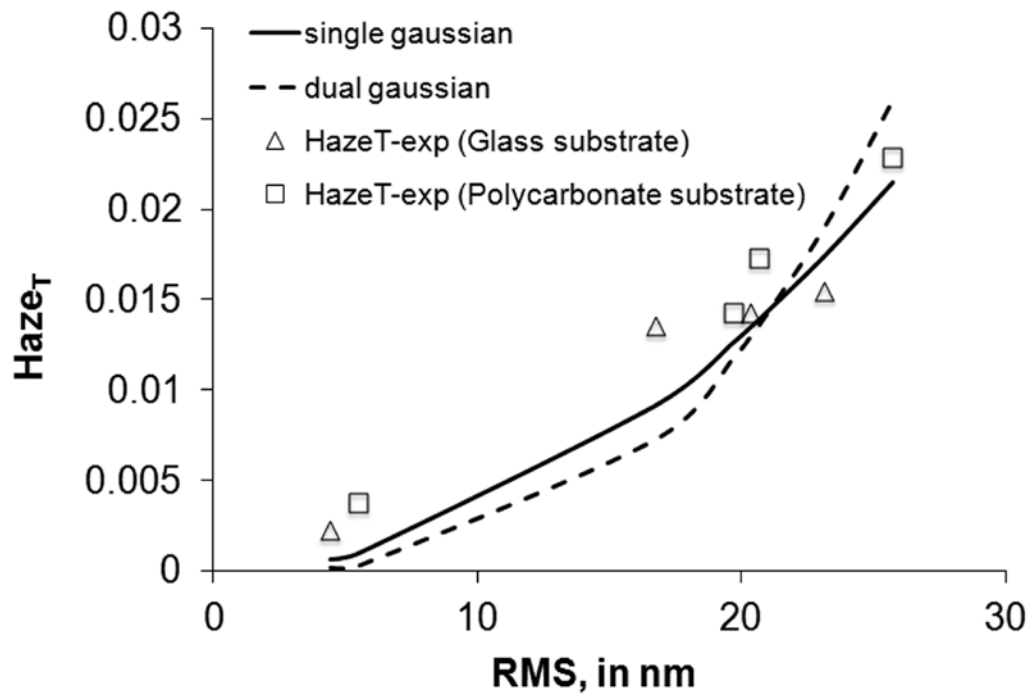


Figure 4.10 Comparison of experimental Haze_T to single and dual Gaussian models.

4.5 Conclusion

Self-assembled surface structures were developed for ultrathin films by using bidisperse nanoparticle size distributions, with the size ratio selected for dense random packing. These experimental nanocomposite surfaces for optical applications have haze properties linked to average surface roughness as estimated by simplified Rayleigh scattering theory, which appear similar to haze values of simulated tipped pyramid surfaces. While monodisperse discrete phases created unimodal structure distributions at the surface, bidisperse discrete phases created multimodal structure distributions. Over our variable range, the multimodal structures had maximum heights less than 1.5 times the diameter of the large spheres. For spin-cast ultrathin films, the substrates appear to affect surface peak height distributions, which are linked to haze. These results suggest that other parameters in addition to surface roughness can affect haze, including the surface chemistry of materials used.

4.6 Nomenclature

RMS	= Root Mean Squared roughness
n	= Sample size
z_i	= Height of each data point
Z_{ave}	= Average height of each data point
θ_y	= Young's contact angle
θ_w	= Wenzel's contact angle
r	= Roughness factor
Y_{sv}	= Solid-Vapor interfacial energy
Y_{sl}	= Solid-Liquid interfacial energy
Y_{lv}	= Liquid-Vapor interfacial energy
Haze _T	= Transmittance haze,
λ	= Wavelength
n_i, n_t	= Refractive index of incident and transmitted material
θ_i, θ_t	= Angle of incidence and transmission
C	= Correction factor
A_0, A_1 and A_2	= Area, Center and Width: 3 parameters of Gaussian distribution
A, B, C, D	= Samples with polymer-nanocomposite coated on substrate

AFM = Atomic Force Microscopy
DLS = Dynamic Light Scattering
SEM = Scanning Electron Microscopy
exp = Experimental

Chapter 5 Fractal analysis as a complimentary technique for characterizing nanoparticle size distributions

This chapter is based on work submitted as: *Vinod Kanniah*, Peng Wu, Natalia Mandzy, Eric A. Grukke, under review, Powder Technology (Copyright: Elsevier)

Keywords: Fractal dimension, Lacunarity, Box counting method, Particle size distribution, Electron microscopy, Dynamic light scattering.

5.1 Highlights

- Fractal coefficients are determined through 2-D image and particle size distributions .
- Ceria and titania nanoparticle products from commercial sources was evaluated along with in-lab synthesized material.
- The box counting method gives fractal coefficients within expected theoretical ranges.
- For some material, the box counting-based fractal coefficients correlated with the primary particle size.

5.2 Introduction

Nanoparticles, defined as having dimensions between 1 and 100 nm, can have exceptional chemical, physical and surface properties for commercial products in pharmaceuticals, cosmetics, ceramics, food, electronics, paints, pigments, and lubricants. The minimal information about nanoparticles (MIAN) needed for characterization is currently being debated, particularly for environmental health and safety issues [121] . Typical information includes measurement of size, shape, surface charge, surface area, surface porosity, composition and structure [8]. Morphology characterization (size, shape, and structure, including surface texture and internal pores) is most commonly done using electron microscopy for powders or dynamic light scattering for liquid dispersions. A complete evaluation of morphology for material science applications also can include phase distribution, which will not be considered here.

Primary particle size (the smallest identifiable subdivision in a particulate system [122]), primary particle size distribution, and aggregates (cohesive masses of primary particles [122]) are

important measurement objectives. There are two types of aggregates: hard-aggregates and agglomerates. Hard-aggregates have primary particles that have been chemically bonded or fused, and cannot be easily redispersed to their primary particle size distribution by the application of moderate mechanical agitation or mild chemical treatment [122]. Agglomerates are cohesive masses in a fluid dispersion that self-associate due to physical or electrostatic forces [122]. Distinguishing between agglomerates and hard-aggregates is often very important to the application; hard-aggregates will have dimensions much larger than those of the primary particles while agglomerates may re-disperse or grow in size. Considerable literature in the physical and life sciences does not adhere to these definitions, which can cause confusion during data interpretation. Figure 6.1a illustrates discrete primary particles, primary particles self-associating (agglomerating) in a fluid dispersion, and primary particles fused into hard-aggregates during synthesis.

Primary particle size distributions are normally measured using electron microscopy (powders) or dynamic light scattering (very dilute liquid dispersions). Agglomerates and hard-aggregates can be challenging to characterize; for example, some of the nanoparticles in this study have primary particles sizes of 20-50 nm, but have aggregate sizes of 25 μm in dimension. These different morphologies can affect nanoparticle performance in commercial applications or in hazard assessment studies. This chapter describes the use of fractal analysis to characterize nanoparticle size distributions; this method is considered complimentary to either electron microscopy or dynamic light scattering, and provides extra information about primary particle size distributions as well as their associations in various media. Fractal analysis can provide additional information useful for: 1) quality control of nanoparticle synthesis processes, 2) selecting conditions for dispersing nanoparticles into liquid and solid systems, and 3) characterizing nanoparticles for toxicological and environmental assessment studies. Our objective is to determine whether fractal coefficients can be correlated with primary particle size and hydrodynamic size information, thereby providing complementary data to conventional measurements for these three applications.

Primary particle size distributions themselves, whether determined in gas or liquid systems, can be considered self-similar fractals i.e., invariant under anisotropic scale transformations [123]. Fractal analyses of particles have been reported for static light scattering [124-125], small-angle x-ray

scattering [126], small-angle neutron scattering [127], dynamic rheological measurements [128], sedimentation [129], electron microscopy [124, 130] and dynamic light scattering [125, 131-133]. Fractal analyses are also being used in medicinal biology [134-136] and applied chemistry [126, 137-138]. Fractal coefficients of nanoparticle morphologies in this work are determined through analysis of particle size distribution and two-dimensional (2-D) images (Figure 6.1b). Particle size distributions can be analyzed using dynamic light scattering (DLS) and/or TEM. Dynamic light scattering experiments report particle size distributions that can be used to determine the fractal dimension and lacunarity of the sample. TEM photomicrographs (2-D images) can be analyzed to determine the fractal dimension of the sample and its lacunarity (the visual texture of the sample) by the box counting method.

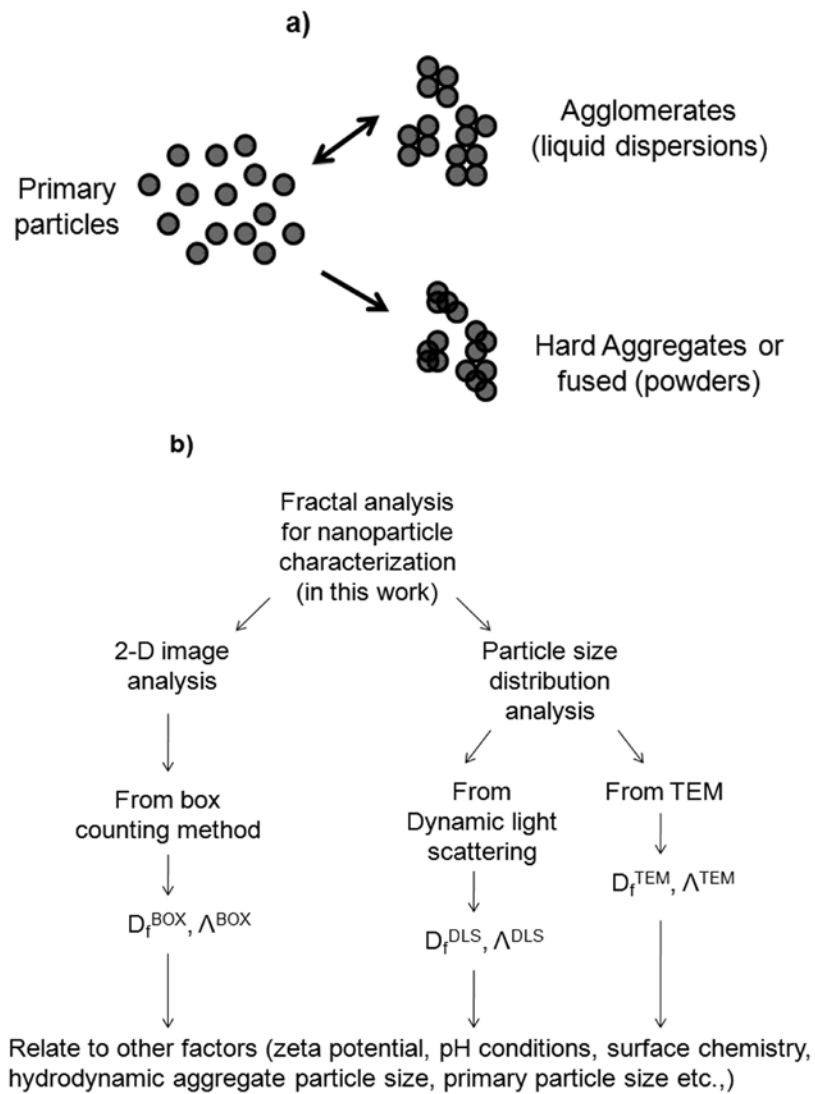


Figure 5.1 a) Aggregation and agglomeration of primary particles, b) Process diagram on fractal analysis for nanoparticle characterization.

5.2.1 Fractal analysis

Particle morphologies are complex patterns with self-similar fractal behavior following a simple general power law relation (Eq.5.1),

$$Y = \text{prefactor} \times X^{\text{exponent}} \quad \text{Eq. 5.1}$$

Where X and Y are variables based on the method chosen. The exponent corresponds to the repeatability of an object. The repeatability of these complex patterns cannot be described through simple Euclidean dimensions and hence is a fraction and not an integer [139]. The prefactor expresses how the space is being filled up by particle structure mass, independent of its size, and how the primary particles are packed [140]. Two simple yet effective methods to explore the power law relation of fractal structures are through two-dimensional image analysis and particle size distributions. An open source software package supported by the National Institutes of Health, ImageJ [141], was used to evaluate the fractal dimensions of nanoparticles via the box counting method. This method was verified using standard fractal images with known fractal dimensions.

5.2.1.1 2-D image analysis (box counting)

This method involves determining the exponent and prefactor through digital image processing of 2-D images. Box counting is the simplest statistical method to study the power law relation [142]. Y corresponds to the number of non-overlapping equal sized boxes of size X that would fill the projected surface area of an image. X is made smaller and Y is determined for each smaller X . The exponent is then derived from a least square linear fit of the plot $\ln Y$ versus $\ln (1/X)$. Thus mathematically, the exponent, box counting fractal dimension (D_f^{BOX}) by this method is:

$$D_f^{\text{BOX}} = \ln Y / \ln(1/X) \quad \text{Eq. 5.2}$$

The prefactor in Eq. 6.1, the box counting lacunarity (Λ^{BOX}), is determined based on the foreground pixel distribution (i.e., pixel mass) of an image obtained from scanning different box sizes within different grid positions chosen.

$$\Lambda^{\text{BOX}} = (\sigma/\mu)^2 \quad \text{Eq. 5.3}$$

Where σ is the standard deviation and μ is the mean for pixels per box. Different grid positions leads to more efficient coverage of an image and removes bias associated with a single starting point for both fractal dimension and lacunarity estimates. A completely homogeneous image will not vary in the pixels per box and hence the standard deviation will be 0, corresponding to rotational or translational invariance and no gaps. Lacunarity is used to classify fractals with same fractal dimension which appear visually different. It is defined as a measure of gappiness, visual texture, inhomogeneity, translational and rotational invariance [141] i.e., if a fractal image has large gaps or holes, it has high lacunarity; whereas, if a fractal is almost translationally invariant, it has low lacunarity.

In the box counting method, biased errors due to poor resolution could be minimized by using high resolution pixel image per primary particle diameter [130]. Fractal dimension is not precise number and is insignificant beyond the second decimal place since the projected images are not the actual object and variations in describing object boundaries may occur [134]. Also, most practical fractals are limited to an experimentally defined or measured scale range. Hence it is a relative measure of complexity i.e., two objects may have the same fractal dimension and still look quite different [136]. This is where lacunarity helps in defining these structures. An increase in the fractional part of fractal dimension suggests that the surface is becoming rougher at all length scales and hence approaches 3-D or mass fractal. Hence, fractal dimension provides a more detailed description across multiple length scales on the true roughness, both vertical and horizontal, of a surface [143].

5.2.1.2 Particle size distribution analyses

When particle size distributions are available, Y corresponds to the cumulative frequency of particles and X to the respective particle size. The exponent and prefactor is then derived from a least square linear fit of the plot $\ln Y$ versus $\ln X$ as in (Eq. 5.4) [144],

$$\ln Y = \ln \text{prefactor} + \text{exponent} \times \ln X \quad \text{Eq.5.4}$$

The exponent corresponds to fractal dimensions determined from dynamic light scattering (D_f^{DLS}) or electron microscopy image (D_f^{PSD}), and the prefactors to lacunarity, Λ^{DLS} and Λ^{PSD} . A low

exponent is suggestive of wider particle size distribution whereas a higher exponent to a narrow size distribution [144]. The exponent and prefactor determined by this method cannot be directly compared to the exponent and prefactor determined from the box counting method as the X, Y axis chosen are different for these two methods.

Dynamic light scattering or photon correlation spectroscopy (PCS) of quasi elastically scattered light (QELS) involves measuring the hydrodynamic radius of particles based on the scattered light caused by diffusive motion of particles. In electron microscopy techniques, primary particle-size distribution is obtained from digital image analysis with sufficient image contrast and spatial separation of the particles. Higher numbers of particles improve the reliability of fractal dimension estimates by this method.

5.3 Experimental

5.3.1 Materials

Titania and ceria nanoparticles were chosen for this study. Sample description of commercial and in-lab synthesized nanoparticles for fractal analysis is shown in Table 5.1, including the sample identification number, scale bar of 2-D images, sample source, primary particle size analysis through TEM and hydrodynamic size analysis via DLS. Samples 1-3 are titania from commercial suppliers, all of which are aggregated. Samples 4-6 are ceria nanoparticles produced by in-lab hydrothermal synthesis methods, all of which have unimodal primary particle size distributions that are not agglomerated. Samples 7-9 are commercial ceria samples of the same product, but with different lot numbers. Sample 10 is a commercial ceria with a multimodal primary particle size distribution. Samples 11-13 are commercial samples with small primary particles. Samples 7-13 are all aggregated.

Table 5.1 Sample descriptions of Ceria and Titania for fractal analysis.

Material	Sample ID	Source*	Scale bar of 2-D images	Primary particle size distribution D_{ave} (90% range), nm (TEM) Crystal structure; morphology; state of aggregation	DLS aggregate size, nm
Ceria	10a, 10b	II	10 nm	25 (6 – 60) multimodal primary PSD cubic; spheroidal (10-12 nm) and octahedral (~ 30 nm); aggregated	Multimodal; 140,480, 2400
	11a, 11b	VI	10 nm	6.3 (4 – 9) cubic; spheroidal; aggregated to 3 μ m	Multimodal; 80, 400 2700
	12a, 12b	I	20 nm	5 (4 – 12) cubic; spheroidal (5 nm) and nanorods (5:1); aggregated	Multimodal; 220, > 5000
	13a, 13b	V	5 nm	5.4 (4 – 8) cubic; spheroidal; aggregated > 10 μ m	Multimodal; 70, 750, 1200
	7a, 7b	I One product code, 3 lots	50 nm	86 (37-111) cubic; spheroidal, octagon and nanorods; aggregated to 3 μ m	Multimodal; 80, 900
	8a, 8b		50 nm	44 (26 – 87) cubic; spheroidal, octagon and nanorods; aggregated to 5 μ m	Multimodal; 70, 300
	9a, 9b		200 nm	59 (36 – 99)	Multimodal;

				bimodal spheroidal aggregates	400, > 1000
	4a, 4b	In-lab synthesized	10 nm	4.6 (3.5 – 7) cubic; discrete primary particles	7.3
	5a, 5b		20 nm	12.4 (9 – 22) cubic; discrete primary particles	30
	6a, 6b		20 nm	31 (15- 70) cubic; discrete primary particles	35
Titania	3a, 3b	I	50 nm	25 (6-47) anatase; spheroidal and short nanorods; aggregated to 25 μ m	Multimodal; 100, 650
	1a,1b	III	50 nm	31 (17-68) anatase; spheroidal; aggregated to 3 μ m	Multimodal; 70, 350, 1400
	2a, 2b	IV	50 nm	57 (36-97) anatase/rutile mixture; spheroidal; aggregated to 15 μ m	Multimodal; 144, 500

* I= Alfa Aesar; II= Aldrich; III=Degussa ; IV= Nano Amor; V= Nano Oxide; VI= Nano Scale.

5.3.2 Electron microscopy

Samples for TEM analysis were prepared by dipping copper lacey carbon grids into 0.01 wt% dispersions of the sample and drying them overnight at room temperature. Ethanol was used as a solvent for all the samples except Samples 4-6, for which deionized ultra filtered water were used. The dried nanoparticle film was then investigated using a JEOL 2010 F Transmission Electron Microscopy (Japan). Scale bar lengths for all images are shown in Table 5.1. Two images were taken at the same magnification for each sample (a, b). Primary particle sizes of the particles were determined by using Digital Micrograph software from Gatan (USA). Only clearly visible and non-overlapping particle were considered for this method. Each randomly qualified particle was outlined manually with a freehand selection tool and analyzed by the software. Primary particle size distributions obtained from electron microscopy images for each sample were fitted to log normal distributions. The D_{ave} reported is the mean of the lognormal distribution and the range reported starts at 5 % of the cumulative number distribution and ends at 95% of the cumulative number distribution.

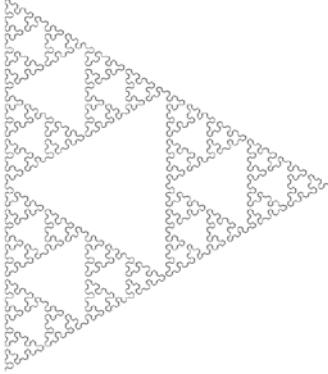
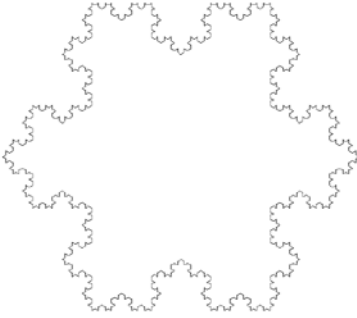
An open source (freely available at <http://rsb.info.nih.gov/ij/>) software package, Image J with added FracLac plugin was used to analyze the pictures taken from electron microscopy. The two-dimensional images were converted to binary images (black=foreground particles; white=background) before analyzed by the FracLac plugin. FracLac fills a series of grids of decreasing box sizes over an image, and for each grid, records the number of boxes that fall on the image and the number of pixels per box for each box size. FracLac scans an image multiple times over different grid positions to minimize grid-based bias associated with the location of the scanning grid and hence reports an average fractal dimension with a standard error. In our analysis, we used the FracLac plugin with no smoothing filter, a minimum box size of 2 pixels and a maximum box size of 45% of the pixilated part of each image. Since the sample was mounted on a surface, only the ceria particle image was selected with care through free hand selection tool. Six grids were selected and automatically analyzed by the software.

5.3.2.1 Control test for box counting method

The Sierpinski arrowhead is a deterministic fractal with a theoretical fractal dimension of 1.585 ($\log_3/\log(1/(1/2))$) [134] and the Von Koch snowflake curve is a random fractal with a theoretical

fractal dimension of 1.262 ($\log_4/\log(1/(1/3))$) [145]. To validate the projected image analysis method we determine the fractal dimension of these complex patterns and report in Table 5.2. The projected image method gave a fractal dimension of 1.561 ± 0.028 (for Sierpinski arrowhead) and 1.246 ± 0.029 (for Von Koch snowflake curve) using the Image J software package.

Table 5.2 Control test for 2-D image analysis (box counting method).

Fractal patterns	Theoretical fractal dimension	Projected Image Method D_f^{box}
Seirpinski Arrowhead 	1.585 $(\log 3 / \log(1/(1/2)))$	1.561 ± 0.028
Von Koch snowflake curve 	1.262 $(\log 4 / \log(1/(1/3)))$	1.246 ± 0.029

5.3.3 Dynamic light scattering

Hydrodynamic particle size distributions were determined using a dynamic light scattering apparatus (Model name: 90 Plus/BI-MAS Particle size analyzer, Brookhaven Instruments Corporation, USA). It is based on photon correlation spectroscopy of quasi-elastic light scattering. About 1 mg/ml of nanoparticle suspension was prepared. Ethanol was used as a solvent for all the samples except Samples 4-6 for which deionized ultra filtered water were used. Then the samples were ultrasonicated for 10 min with a bath sonicator. If the dispersions were too hazy for analysis, the dispersions were diluted further with the solvent until they reached desired level of transparency. Three runs were performed for each sample. The number based hydrodynamic particle size distribution obtained was then fit to a log normal distribution.

5.3.4 Zeta potential

Zeta potential of nanoparticle suspension in water was determined through a Zetasizer 2000 (Malvern instruments, Worchestershire, UK). Sodium hydroxide and hydrochloric acid were used to obtain 6 different pH of nanoparticle suspension in water. The concentration of each dispersion was about 0.15 mg/ml. For each pH, 4 data points were recorded. Zeta potential of nanoparticle suspension in water of varying pH is then fitted with Carreau equation (Eq.5.5), which assumes limiting values at low and high pH, and power law relationship in between these values.

$$\frac{Z - Z^{\infty}}{Z^0 - Z^{\infty}} = (1 + (a * pH)^2)^{(b-1)/2} \quad \text{Eq. 5.5}$$

Z^0, Z^{∞}, a, b are the four parameters to fit zeta potential variations of nanoparticle suspensions with pH. A statistical analysis tool, Systat V 12 was used to perform this non linear regression.

5.4 Results & Discussion

5.4.1 Titania nanoparticles

Figure 5.2 corresponds to the 2-D images of titania nanoparticles (Samples 1-3). Two images (a, b) are shown for each sample for which box counting and TEM particle size distribution method was used for fractal coefficient determinations.

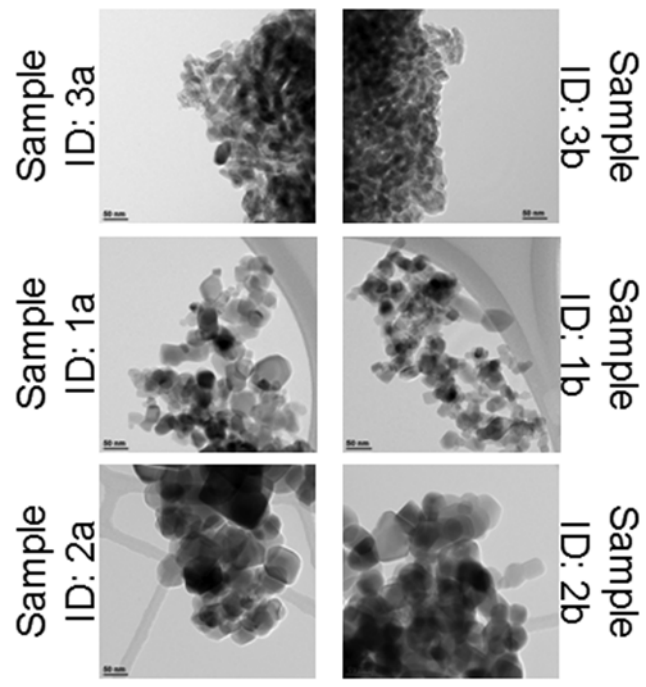


Figure 5.2 2-D TEM images of Titania nanoparticle samples (Sample ID: 1-3).

Average primary particle size of titania nanoparticle samples (from TEM) were 25 nm (Sample 3), 31 nm (Sample 1), and 57 nm (Sample 2) respectively. Figure 5.3(a) and Figure 5.3(b) describes the effect of average fractal dimension and lacunarity determined from 2-D images (box counting). The box counting coefficients, fractal dimension and lacunarity, appear to have power law dependency on the average primary particle size, with both models having R^2 values greater than 0.9. Figure 5.3(c) and Figure 5.3(d) correspond to the fractal dimension and lacunarity determined from particle size number distribution generated from the Digital Micrograph software. The fitting coefficients for Eq. 5.4 do not appear to correlate as well with D_{ave} . Notice that the 'fractal dimension' is not less than 3 (the maximum theoretical value) and that the 'lacunarity' values are very small.

Fractal analysis was not performed on the DLS data for samples 1-3 (Table 5.1). These titania are aggregated, as observed with TEM data. SEM evaluation showed that aggregates as large as 25 μm were present in one sample. Zeta potential measurements showed that, for $\text{pH} > 6$, the zeta potential of all these samples was less than -30 mV, so they should be electrostatically stable and non-agglomerating in water dispersions. There are four complicating factors for interpreting DLS particle size distributions for these samples. Ultrasonication, which is often used to aid dispersion of nanoparticles in liquids, fractures aggregates, so the sample preparation process affects the results. Despite the zeta potential measurements indicating electrostatic stability, agglomeration might occur for some samples. Differential distribution data for multimodal samples reported from DLS instruments can be sparse depending on the location and size of the peaks, increasing sample-to-sample variations. The apparent density of the aggregates is usually not known, which will affect the estimates for the hydrodynamic diameter. Apparent peaks in the dispersion size distribution are noted in Table 6.1, but further evaluation of these would be quite complex.

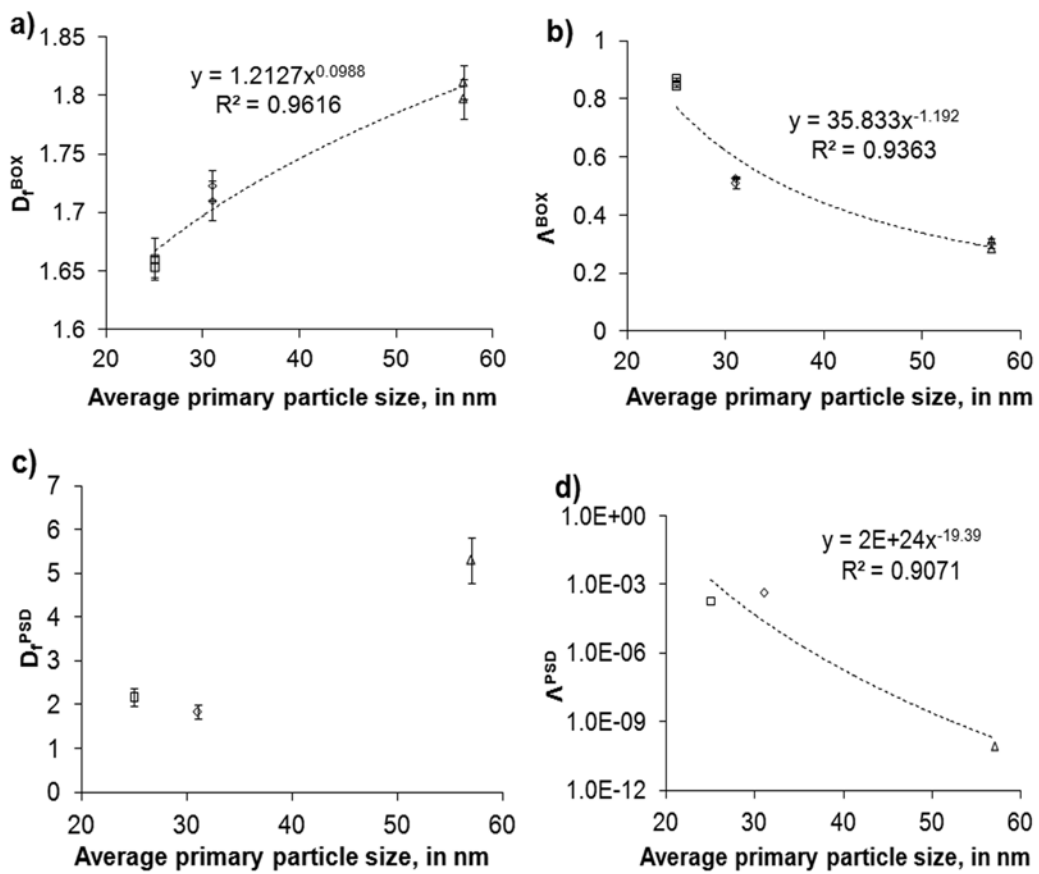


Figure 5.3 Effect of average primary particle size (from TEM) on: a) D_f^{BOX} =box counting fractal dimension, b) Λ^{BOX} =box counting lacunarity, c) D_f^{TEM} =TEM fractal dimension and d) Λ^{TEM} =TEM lacunarity of commercial Titania nanoparticle samples.

5.4.2 Ceria nanoparticles

Figure 5.4 shows the 2-D images of Ceria nanoparticles (Samples 4-13). Two images (a, b) are shown for each sample. Samples 4-6 was synthesized in our lab whereas Samples 7-9, 10, 11-13 are commercial ceria samples obtained from different vendors. The aggregated commercial samples were suitable for fractal analysis by the box counting and particle size distribution methods (TEM). The unimodal samples (4-6) were suitable for fractal analysis by all three methods, as they are known not to be aggregated; particle sizes measured by DLS larger than those measured by TEM would be due to agglomeration.

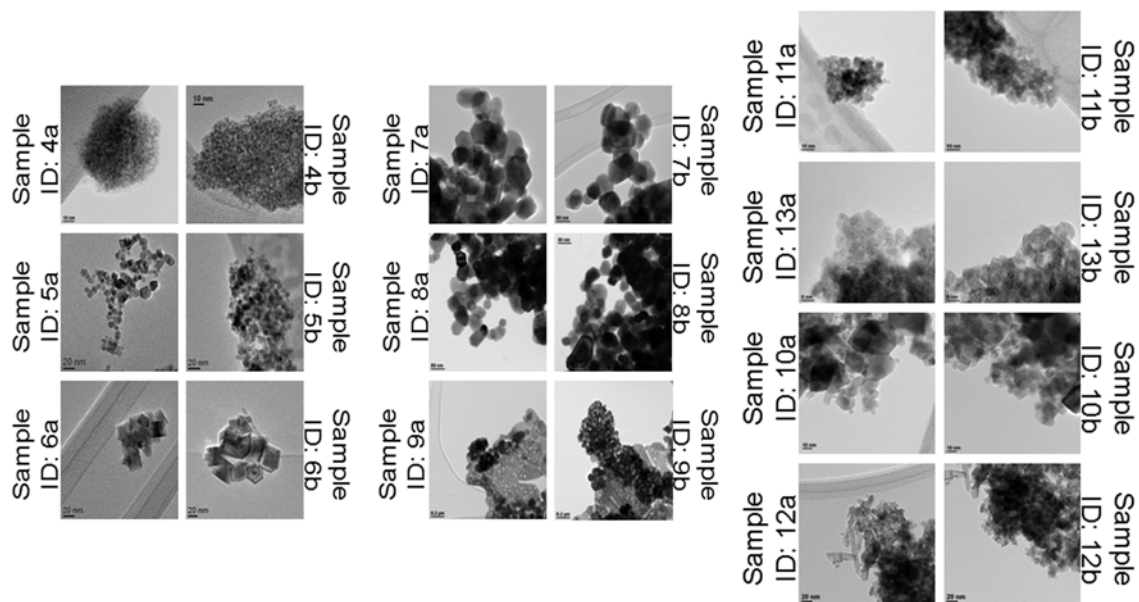


Figure 5.4 2-D TEM images of ceria nanoparticle samples (Sample ID: 4-6, 7-9, and 10-13).

Figure 5.5 (a) and Figure 6.5(b) describes the effect of average fractal dimension and lacunarity determined from box counting method on the average primary particle size (from TEM) of commercial ceria nanoparticle samples. Sample 7-9 were obtained from one vendor from three different lots having an average primary particle size (from TEM) of 44 nm (Sample 8), 59 nm (Sample 9), and 86 nm (Sample 7) respectively. Sample 10 had an average primary particle size of 25nm. Samples 11-13 were obtained from different manufacturers with average primary particle size ~ 5nm (different from the manufacturer's claimed particle sizes). The fractal dimension from the box counting method did not correlate with the average primary particle size. Except for Sample 8, all of the samples had D_p^{box} values that were similar. There is an apparent trend for the lacunarity, but the power law correlation did not meet our metric of $R^2 > 0.9$. The coefficients for Eq. 5.4 also did not correlate strongly with the average primary particle size (Fig. 6.5(c) and 6.5(d)).

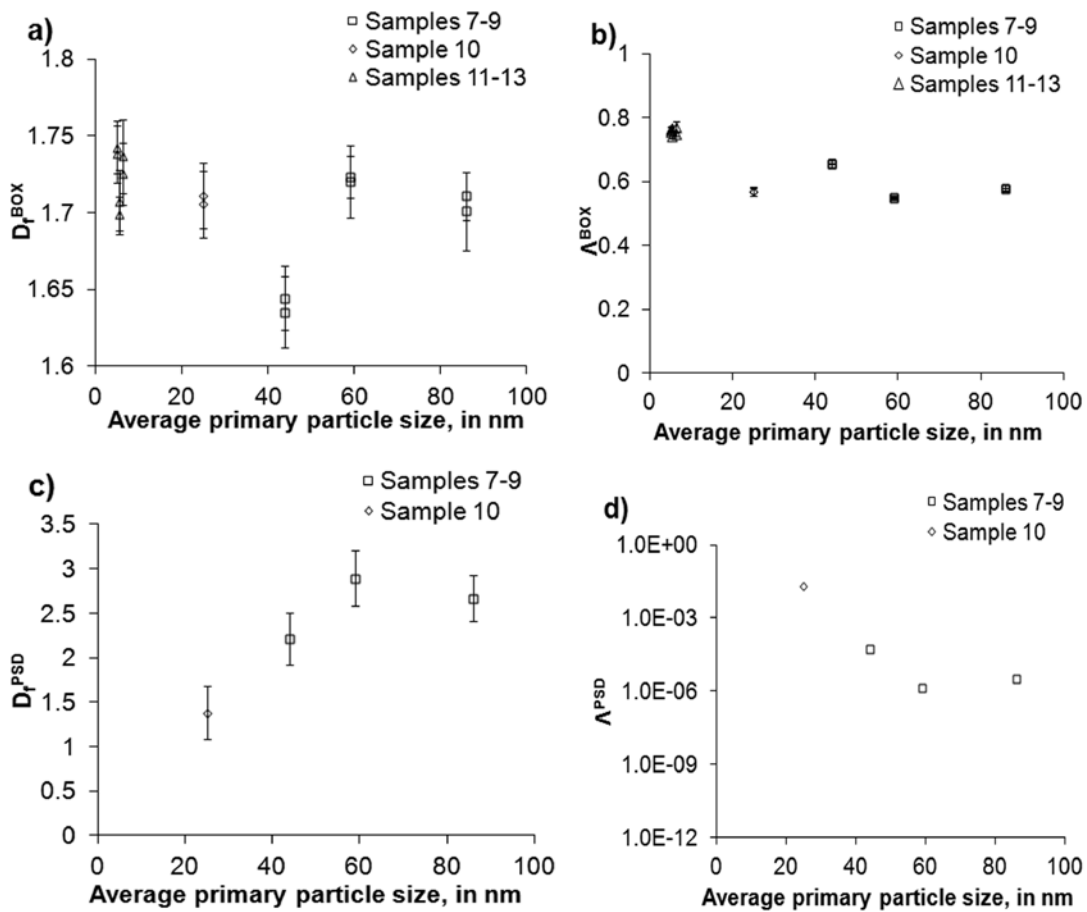


Figure 5.5 Effect of average primary particle size (from TEM) on: a) D_f^{BOX} =box counting fractal dimension, b) Λ^{BOX} =box counting lacunarity, c) D_f^{PSD} =TEM fractal dimension and d) Λ^{PSD} =TEM lacunarity of commercial Ceria nanoparticle samples.

Figure 5.6(a) and Figure 5.6(b) correspond to the average fractal dimension (from box counting) and average lacunarity estimates (from box counting) of unimodal ceria samples. The fractal dimensions did not correlate with primary particle size. However, the lacunarity showed a good power law correlation with D_{ave} . Figure 5.6(c) and Figure 5.6(d) compare fractal analyses for the unimodal samples using the TEM primary particle size distributions and the DLS apparent hydrodynamic diameters. The ratio of the DLS hydrodynamic size to D_{ave} (Table 5.1) can be used to assess agglomeration. For samples 4-6, these ratios are 1.2, 7.5 and 4.1, respectively. The 5 nm sample has essentially no agglomerates, while the 12 nm and 30 nm samples have agglomerated, but with low numbers of particles in the average 'assembly'. The fractal dimension estimated from the primary particle size distribution data, D_f^{PSD} , followed a power law correlation with the primary particle size. The fractal dimension estimated from DLS data, D_f^{DLS} , did not correlate with D_{ave} . Both sets of lacunarity values correlated with the average primary particle size, but their power law coefficients had different signs. In addition, the lacunarity values obtained from this analysis are very low.

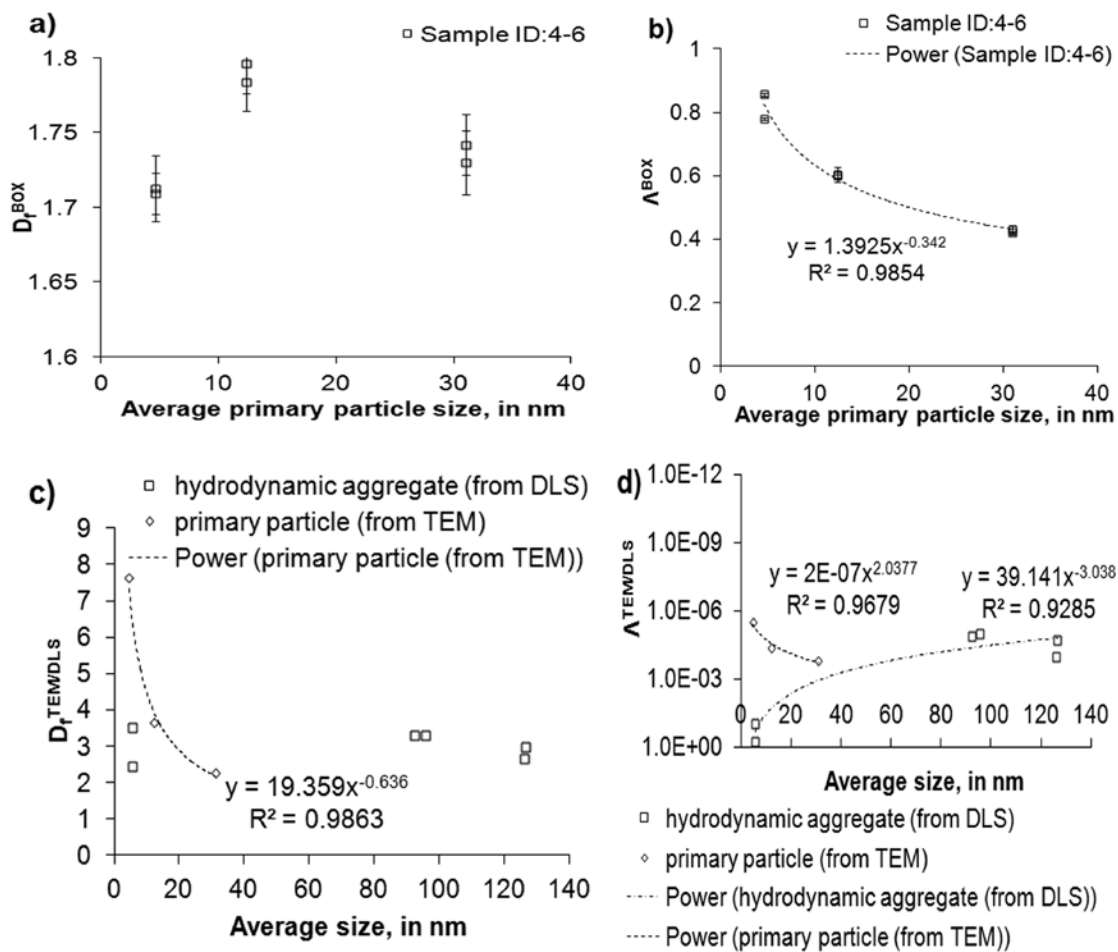


Figure 5.6 Effect of average primary particle size (from TEM) on: a) D_f^{BOX} =box counting fractal dimension and b) Λ^{BOX} =box counting lacunarity of in-lab synthesized Ceria nanoparticles. Effect of average primary particle size (from TEM) and average hydrodynamic aggregate size (from DLS) on c) $D_f^{TEM/DLS}$ =TEM/DLS fractal dimension and d) $\Lambda^{TEM/DLS}$ =TEM/DLS lacunarity of the same samples.

5.4.3 Effect of different surfaces on fractal parameters

Figures 5.7(a) correspond to the particle stability (zeta potential) variation with change in pH of selected ceria samples (Samples 4-6, Sample 10) whereas Figure 6.7(b) describes the same for Samples 1-3. Samples 10, 4, and 6 were fitted via Carreau (4 parameter) model as described before; since all the samples have zeta potentials less than -30 mV at pH ~ 7, they should be electrostatically stable at the conditions of the DLS experiments. Sample 5 required more data to evaluate with a Carreau model as Z^0 tends to infinity for these cases. The titania had zeta potential values less than -30 mV, indicating that they should be electrostatically stable at the DLS measurement conditions of pH ~ 7.

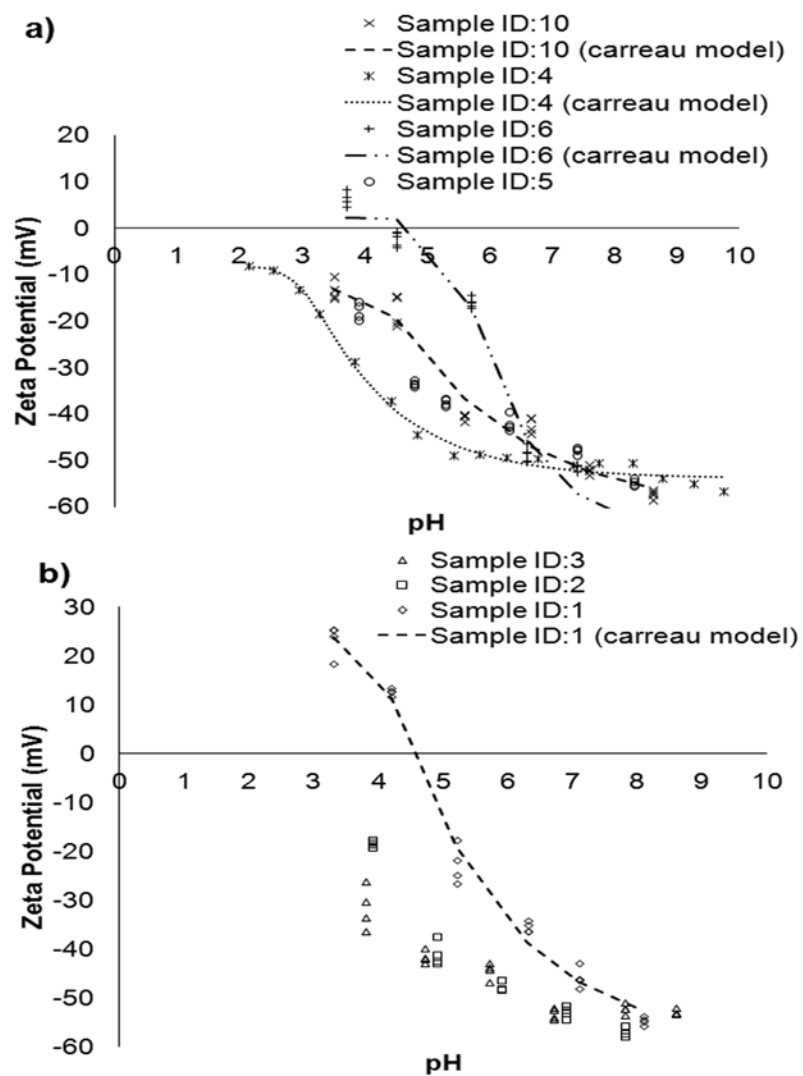


Figure 5.7 Effect of pH on Zeta potential of selected Ceria and Titania nanoparticle samples.

To study the effect of surface property changes on fractal parameters, the surface of the in-lab synthesized ceria (Sample 5) was modified with citric acid and silane [146]. Fractal dimension (from DLS) and lacunarity (from DLS) measured for the different surfaces created on Sample 5 are shown in Figure 5.8(a) and Figure 5.8(b). There is not a strong correlation between D_f^{DLS} and D_{ave} ; the fractal dimension is relatively insensitive to the average hydrodynamic size. There is an exponential fit for Λ^{DLS} as a function of D_{ave} , however, it may not be useful for quality control since the values of the 'lacunarity' coefficient are very low.

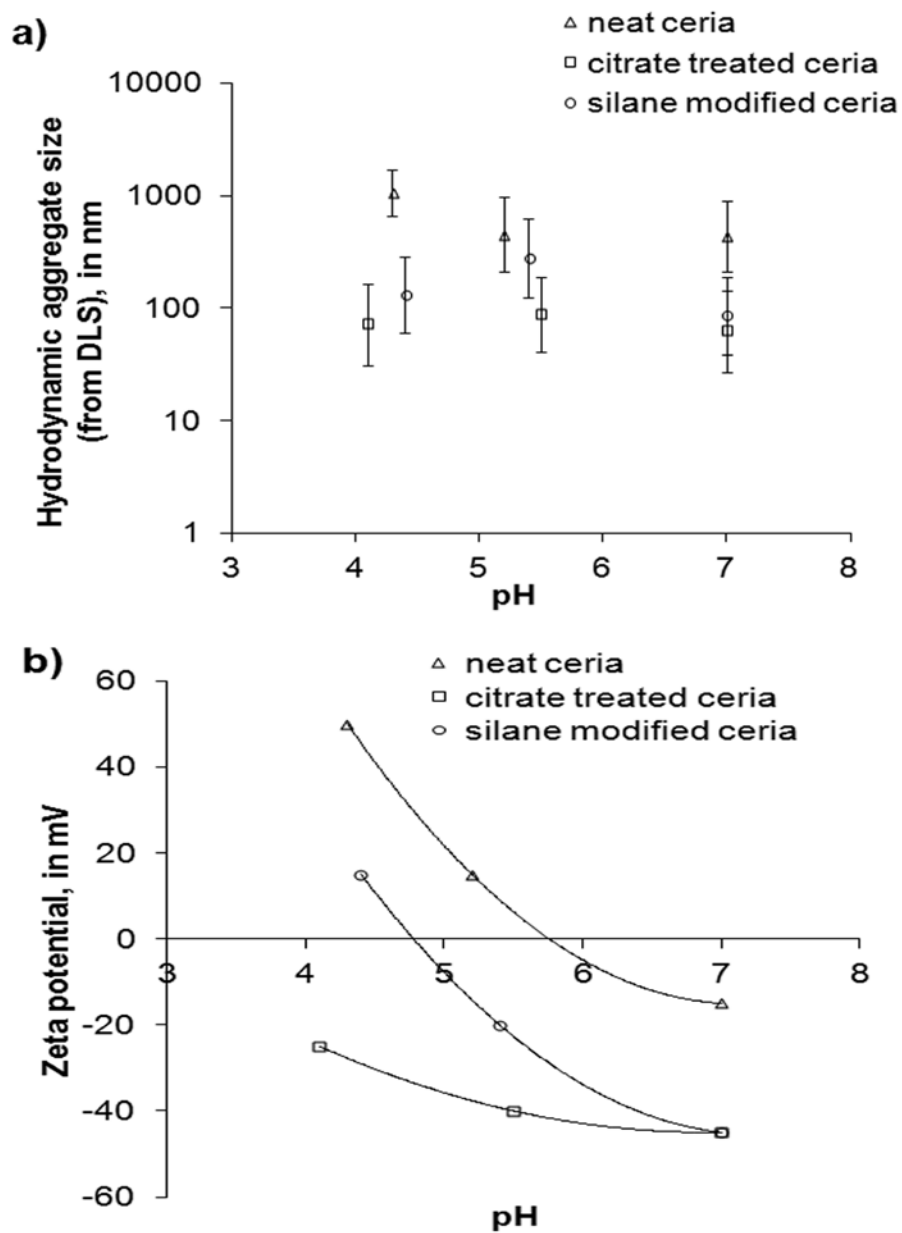


Figure 5.8 Effect of pH on a) Hydrodynamic aggregate size (from DLS) and b) Zeta potential of different surface chemistries on a particular in-lab synthesized Ceria nanoparticle sample (Sample ID: 5).

5.4.4 Comparison of fractal analysis methods

The theoretical maximum for D_f values is 3, and values for lacunarity range between 0 and 1. Aggregation and agglomeration processes depend on particles diffusing toward each other. At some characteristic distance apart, there is a certain probability that the particles will stick together. When the sticking probability is high in comparison to the particle diffusion, the process is known as diffusion-limited aggregation (DLA). If, on the other hand, the diffusion rate is high in comparison to the sticking reaction rate, the process is known as reaction-limited aggregation (RLA) [132]. For diffusion-limited aggregation (DLA) or fast aggregation, every time a primary particle or cluster encounters another cluster, it sticks and the resulting agglomerate tends to have an open, tenuous architecture with low fractal dimension ($D_f^{\text{BOX}}=1.75-1.8$). On the other hand, for reaction-limited aggregation (RLA) or slow aggregation, particles tend to stick in only those regions that represent the lowest potential energy sites and dense compact agglomerates form with higher fractal dimensions ($D_f^{\text{BOX}}=2-2.1$). [147-148] The aggregated ceria and titania of this study have been produced in the gas phase, where 'sticking' results in fused particles. The agglomeration of unimodal ceria could follow one of the mechanisms above.

5.4.4.1 Box counting method

The fractal dimensions, D_f^{BOX} , for the titania samples range between 1.65 and 1.82 (Fig. 5.3(a)), a range consistent with diffusion-limited aggregation. The fractal dimensions, D_f^{BOX} , for the ceria samples range between 1.62 to 1.74 (Fig. 5.5(a)), also fairly consistent with the range expected for diffusion-limited aggregation. The unimodal ceria samples undergo an agglomeration process in the solvent used to disperse them on the carbon grid used for TEM analysis, i.e., they prefer to self-associate rather than associate with the sample grid. D_f^{BOX} for these samples are in the range, 1.71 to 1.80, also consistent with the DLA mechanism. The lacunarity values for these samples all decrease with increasing particle size (Figs. 5.3(b), 5.5(b) and 5.6(b)).

5.4.4.2 Primary particle size distribution method

The best correlations between D_f^{PSD} and Λ^{PSD} to D_{ave} were for the unimodal ceria samples. These data relate to how these samples agglomerated during their sample preparation for TEM analysis. A low shape factor, D_f^{PSD} , is suggestive of wider particle size distribution whereas a higher shape

factor to a narrow size distribution [141]. 'Lacunarity' coefficients, Λ^{PSD} and Λ^{DLS} , are very low compared to the numbers generated from the box counting method measurement; it is not clear how these two methods are related or whether such coefficients are viable.

5.4.4.3 Hydrodynamic size method

When unimodal particles are analyzed by DLS, the fractal coefficients should relate to agglomeration, or the lack of it. In this case, it seems likely that the fractal dimensions might correlate with zeta potential or other measures of surface chemistry, which is likely to control the agglomeration process and steady-state agglomerate size distribution. Table 3 summarizes the findings of this study on fractal analysis as a complimentary analysis for primary particle size distributions of nanoparticles.

Table 5.3 Correlations and trends between D_{ave} , D_{hyd} and fractal coefficients.

Samples	Morphology	Box counting method	Particle size distribution, TEM	Hydrodynamic size distribution, DLS
1-3 (titania)	Aggregated	D_f^{BOX} values within expected range for diffusion-limited aggregation; fractal dimension and lacunarity correlated with D_{ave} for these samples.	D_f^{PSD} trended with D_{ave} . Λ^{PSD} correlated with D_{ave} .	N.A.
4-6 (ceria)	Unimodal	D_f^{BOX} values within expected range for diffusion-limited agglomeration lacunarity correlated with D_{ave} for these samples.	D_f^{PSD} and Λ^{PSD} correlated with D_{ave} .	D_f^{DLS} may correlate with zeta potential D_f^{DLS} was not sensitive to D_{hyd} ; Λ^{PSD} had a power law correlation with D_{hyd} ; the power law model for Λ^{PSD} has the opposite sign as that for Λ^{DLS} .
7-10(ceria)	Aggregated	D_f^{BOX} values within expected range for diffusion-limited aggregation; fractal dimension trended with D_{ave} ; lacunarity correlated with D_{ave} for these samples.	D_f^{PSD} trended with D_{ave} ; and Λ^{PSD} correlated with D_{ave} .	N.A

5.5 Conclusion

The box counting method gives values of fractal dimension and lacunarity within the theoretical range expected for primary particles in aggregated and unaggregated samples. For some arbitrary collections of aggregated nanoparticle materials (for example, titania), D_f^{BOX} and Λ^{BOX} correlated to the average primary particle size. Such correlations would be useful for quality control applications. The two alternative fractal methods based on particle size distributions gave fractal dimensions for some samples that were outside of the expected theoretical range. The lacunarity values from these methods correlated with primary particle size averages, but the values themselves were several orders of magnitude lower than those of the box counting methods. It may be possible to develop quality control applications based on these methods as well, but their connection with the box counting method is uncertain. Based on these findings, it appears possible to use fractal analysis to differentiate between sample populations with both aggregated and unaggregated particles, as a complimentary technique to conventional particle sizing methods.

5.6 Nomenclature

X, Y	= Variables
BOX	= Box counting method
DLS	= Dynamic light scattering
TEM	= Transmission electron microscopy
PSD	= Particle size distribution
D_{ave}	= Average primary particle size, from TEM particle counting
D_{hyd}	= Average hydrodynamic size, evaluated from DLS experiment
D_f^{BOX}	= Box counting fractal dimension
Λ^{BOX}	= Box counting lacunarity
D_f^{DLS}	= Dynamic light scattering fractal dimension
Λ^{DLS}	= Dynamic light scattering lacunarity
D_f^{PSD}	= Particle size distribution (TEM) fractal dimension
Λ^{PSD}	= Particle size distribution (TEM) lacunarity
Z^0, Z^∞, a, b	= Parameters of Carreau model
pH	= Hydrogen ion Activity in solution
Z	= Zeta potential

Chapter 6 Conclusions

This dissertation was focused on interdisciplinary projects dealing with nanoparticle additives in multiphase systems: liquid (nanofluid) and polymer (nanocomposite) matrix along with nanoparticle size characterization by fractal theory. A summary of research done and future work that could be done on each project are shown below.

6.1 Nanofluid additives for Nanofluids

6.1.1 Summary

Base fluid phase equilibria. Universal base oils that remain pourable over wide temperature ranges would have important advantages for lubrication applications. The model system used in this project was a poly(α -olefin) synthetic base oil modified with poly(dimethylsiloxane) to lower the pour point temperature. While the blend was miscible at room temperature, phase separation occurred at temperatures less than -15 °C. Partition coefficients of such non-ideal oligomer mixtures can: 1) help define operating temperature ranges and 2) provide a basis for designing molecular weight distributions of each lubricant that control or prevent phase separation. The poly(α -olefin) base oil family is branched oligomers of 1-decene with two to five n-mers at levels greater than 1 wt% while poly(dimethylsiloxane) additives are linear oligomers of condensed dimethylsiloxane having between 10 to 50 sequential n-mers at levels greater than 0.5 wt%. FT-IR measurements of the poly(α -olefin) and poly(dimethylsiloxane) compositions in each phase provided an overall material balance. Poly(α -olefin) oligomers were detected using size exclusion chromatography with a differential refractive index detector and poly(dimethylsiloxane) oligomers were detected using MALDI-TOFMS. The best sets of measurements for the individual oligomers in each phase were selected by minimizing the overall material balance errors. For both oligomers, components with high molecular weights were preferentially excluded from the phase rich in the other polymer and were relatively independent of temperature. Partition coefficients of poly(α -olefin) components increased with increasing oligomer length while partition coefficients of poly(dimethylsiloxane) components decreased with increasing oligomer length.

Graphite based 'Universal base oil' nanofluids. Fluids with thermally conductive nanoparticles can provide improved heat transfer. Practical nanofluids will be likely based on lubricating oils with

extended service temperature ranges. A model system based on poly(α -olefin) synthetic base oil modified with poly(dimethylsiloxane) to lower the mixture's pour point with graphite as a conductive additive was studied. Phase separation of the oligomer mixture occurred at temperatures less than -15 °C. Graphite particles were etched using citric acid pretreatment to create hydroxyl and carboxyl groups on their surfaces. A coupling reaction between the hydroxyl groups on graphite and chloro groups on silanes gave rise to poly(α -olefin)-philic graphite particles. Similarly, a coupling reaction between the carboxyl groups on graphite surface and amine groups on silanes gave rise to poly(dimethylsiloxane)-philic graphite particles. SEM, FT-IR, and TG-MS measurements were used to verify the presence of coupling agents on the surface and to estimate the thickness of the coatings. Upon separation of the mixture, each functionalized graphite type migrated exclusively to its preferred phase.

6.1.2 Future research

The work on polymer deconvolution used as a tool to identify the n-mers responsible in (poly(α -olefin)-poly(dimethylsiloxane) mixture could be used in characterizing other phase separating oligomer mixtures. Alternative choices for poly(dimethylsiloxane) which have low temperature viscometrics and doesn't decompose to an unwanted solid could be studied to develop other model 'universal base oils'. Systematic study on surface group analysis and surface modification of graphite to poly(α -olefin)-philic and poly(dimethylsiloxane)-philic phase could be extended to other nanoparticle additives in continuous phase systems. Proposed range of (poly(α -olefin)-poly(dimethylsiloxane) oligomer n-mers from partitioning estimates could be tested for phase separation and studied for tribological properties.

6.2 Nanoparticle additives for Polymer Nanocomposites

6.2.1 Summary

In optical applications, control of surface roughness can have a large impact on haze and the optical quality of the system. This work compares surface roughness and haze for self-assembled experimental surface structures to simulated surface structures of ultrathin nanocomposite films. Ultrathin nanocomposite films were synthesized from an acrylate monomer as the continuous phase and monodisperse or bidisperse mixtures of silica nanoparticles as the dispersed phase. An in-house spin coating deposition technique was used to make thin nanocomposite films on

hydrophilic (glass) and hydrophobic (polycarbonate) substrates. Manipulating the size ratios of the silica nanoparticle mixtures varied the average surface roughness as well as the height distributions. Surface property measurements included Wenzel's contact angle, root mean squared roughness, and transmittance haze. For the simulated surfaces, roughness was estimated from their morphologies, and haze was calculated using simplified Rayleigh scattering theory. Experimental data for haze and morphologies of nanocomposite films corresponded well to these properties for simulated tipped pyramid surfaces. Mixtures of large and small nanoparticles produced multimodal surface structures.

6.2.2 Future research

Multimodal surface distributions provide important benefits: increased roughness for better surface adhesion and shear strength. Experimental surfaces created provide an acceptable limit of roughness/haze for practical applications. Other nanoparticles, monodisperse TiO_2 , which has a much higher refractive index, could be studied. New surfaces could be developed of close packed system with the proper volume ratio of small to large (since we only controlled diameter ratio in this project). Based on the understanding of multimodal surface distributions, acceptable range of roughness/haze (chapter 4) and a simple nanoparticle functionalization protocol (from chapter3), ultrathin film antireflective coatings could be developed (*Vinod Kanniah*, Binghui Wang, Thad Druffel, Eric A. Grulke, manuscript in preparation, Thin Solid Films).

6.3 Nanoparticle size distribution characterization

6.3.1 Summary

Fractal analysis of nanoparticles in wet and dry systems can be a simple yet effective complimentary method to assessing primary particle size distributions and aggregation/agglomeration phenomena in process applications where not much is known about the system's surface chemistry/properties. A set of well-characterized ceria and titania nanoparticle products from commercial sources was evaluated along with in-lab synthesized material. The analyses included determining fractal dimension and lacunarity through two-dimensional images from electron microscopy as well as particle size distributions obtained through electron microscopy and dynamic light scattering. The box counting method gives values of fractal dimension and lacunarity within the theoretical range expected for primary particles in aggregated

and unaggregated samples. For some arbitrary collections of aggregated nanoparticle materials (for example, titania), the box counting-based fractal dimensions and the lacunarity correlated to the average primary particle size. Such correlations would be useful for quality control applications, such as nanoparticle production, nanocomposites formulation for coatings, and nanoparticle dosage for toxicological effects.

6.3.2 Future research

Fractal theory based characterization could be explored to other nanoparticle systems to find a link between fractal coefficients and other parameters like zeta potential, pH of system etc., Fractal theory could be explored in the field of medical imaging to identify meaningful patterns. Example – muscle cells w/ and w/o cancer.

Appendix

Chapter 1: Supplementary information

Table 1.1 Heilmeier's matrix: Developing 'universal base oil'.

What are you trying to do?	Develop a model 'universal base oil' for vehicle engine lubrication that could be used over a wide temperature ranges (particularly low temperatures upto - 80 °C (193 K).
How is it done today?	Mixtures of Alpha-olefin oligomers, often called poly(α -olefins), which are commonly used as synthetic lubricant base stocks.
What's new in your approach?	<ul style="list-style-type: none"> • Add a modest fraction of a lubricant oligomer, poly(dimethylsiloxane) with the needed low temperature viscometrics (low pour point and high viscosity index), extend the temperature range of the mixture. • Add two graphite nanoparticle systems that disperse in each phase when phase separation occurs.
Who cares?	US Army (TARDEC) which uses lubricating oils for their vehicles wants to reduce their logistics cost in transporting different grade oils to cold and hot regions across the world. If successful, other lubricant manufacturers would want this technology.
What difference will a successful project make?	A product would solve TARDEC logistic issues and might be transferred to the public sector.
What are the risks/payoffs?	<ul style="list-style-type: none"> • Using poly(dimethylsiloxane) as base oil is likely to affect engine performance. • Poly(dimethylsiloxane) and poly(α-olefins) oligomer mixtures phase separate at low temperatures.
How much (cost)/long will it take?	N/A. Valvoline was responsible for pricing.
What are the milestones to check for success?	<ul style="list-style-type: none"> • Characterizing and predicting phase separation behavior of oligomer mixtures. • Nanoparticle (graphite) surface modification that enable it to partition to either phase (two chemistries are required).

Table 1.2 Heilmeier's matrix: Developing 'low haze ultrathin nanocomposite films'.

What are you trying to do?	Develop 'low haze ultrathin nanocomposite films' for optical product applications. Applications include but not limited to hydrophobic coatings.
How is it done today?	Nanoparticle-acrylate monomer nanocomposite system.
What's new in your approach?	Model nanocomposite (bidispersed mixtures of silica-acrylate monomer) to control surface roughness (improved hydrophobicity).
Who cares?	VDL (funding sponsor) who develops optical products with desired specifications. Other Specialty coatings manufacturers.
What difference will a successful project make?	Develop new performance coatings (hydrophobic) for optical product applications.
What are the risks/payoffs?	Increasing surface roughness with low haze is a challenge in ultrathin films.
How much (cost)/long will it take?	N/A. VDL was responsible for pricing.
What are the milestones to check for success?	Effect of surface roughness on haze of bidispersed mixture of silica based polymer nanocomposite.

Table 1.3 Heilmeier's matrix: Developing 'complimentary characterization technique'.

What are you trying to do?	Develop 'complimentary characterization technique' for nanoparticle size distributions.
How is it done today?	Electron microscopy (for powders) and light scattering (for liquid dispersions).
What's new in your approach?	Fractal theory based size distribution characterization (for both powders and liquid dispersions).
Who cares?	EPA (funding sponsor) for quality control of nanoparticle production. Other Nanoparticle manufacturers.
What difference will a successful project make?	<ul style="list-style-type: none"> • Describe aggregation/agglomeration phenomenon when system's surface chemistry/property is unknown. • Relate fractal coefficients determined to other surface based parameters (zeta potential, surface group, pH of medium etc.).
What are the risks/payoffs?	New technique development may require even more detailed analysis (like considering different materials, different conditions etc.).
How much (cost)/long will it take?	N/A. College of Pharmacy, UKY was responsible for pricing.
What are the milestones to check for success?	Relating fractal coefficients to aggregation/agglomeration of nanoparticles in powder and liquid states.

Chapter 4: Supplementary information

MATLAB code for RMS determination of a 3-dimensional surface (% corresponds to comments)

```
a = mean(mean(z));           % Z is the height values given by a 100 x
                             100matrix.
b = ones(100,100);         % Creates a 100 x 100 matrix with each value
                             being 1.
c = b*a;                   % Multiplies the average height by the ones,
                             thus creating a 100 x 100 matrix of the
                             average height.
u = z-c;                   %Subtracts the average height from the height
                             at each point i.e. deviations.
y = sqrt(sum(u.*conj(u))/size(u,1)); % RMS equation (the input is deviations).
rms = mean(y)              %Averages the RMS of each line to give
                             a single RMS value for the surface.
```

Determining RMS for a 3-dimensional surface

The RMS equation requires an input quantity known as deviation. Deviation is defined as the difference between a specific value (in our case a point) and the mean of a dataset (a surface). The RMS equation, in this sense, was designed for 2-dimensional data (a single line of heights). When seeking a value for 3-dimensional data, problems occur in that there is more than one feasible way to bring together multiple lines. One way (which we decided not to use) is to use the mean height of each line individually in the calculation of deviation, so that the RMS of one line was determined with a different mean height than the one before. This was discredited because it seemed to us that it did not properly account for a change between two lines. For instance, one could imagine a surface with one line of zeros and the next line having a values of tens - it would have obvious variability, yet with this method the RMS would read zero, as there is no deviation along each line individually and the average of zero RMS from two lines is zero. To solve this problem we needed the deviation value to account for variability across the lines as well. Our solution was to average all of the average heights from each of the individual lines. This creates a single value denoted as "a" in our code and it will be used to calculate deviation ("u"). For

subtraction, the matrices must be the same dimensions. We therefore created a matrix of the value one with the same dimensions as the surface (100 x 100) called "b". When multiplied by the mean height, the resulting matrix "c" is ready to be subtracted from the individual heights "z". The result of this subtraction is the deviation of each point from the average height of the whole surface. Once plugged into the RMS equation the 100 x 100 matrix of deviations is transformed into a 100 x 1 matrix "y" (really a vector) of the RMS of each line. Then, to provide a single value for comparison between surfaces, we averaged the 100 RMS values.

Example MATLAB code for Haze determination

```
HazeT = 1-exp(-((2.*pi.*rms./lambda)*abs(1.458*cos(0)-1*cos(2.5.*pi/180))).^2)
```

```
Lambda = 550;
```

```
% Haze equation (uses RMS values of different simulated surface morphologies).
```

References

- [1] M. Alexandre, P. Dubois, *Materials Science and Engineering R* 28 (2000) 1.
- [2] S.S. Ray, M. Okamoto, *Progress in Polymer Science* 28 (2003) 1539.
- [3] F. Chivrac, E. Pollet, L. Averous, *Materials Science and Engineering R* 67 (2009) 1.
- [4] S. Bredeau, S. Peeterbroeck, D. Bonduel, M. Alexandre, P. Dubois, *Polymer International* 57 (2008) 547.
- [5] B. Fiedler, F.H. Gojny, M.H.G. Wichmann, M.C.M. Nolte, K. Schulte, *Composites Science and Technology* 66 (2006) 3115.
- [6] H. Althues, J. Henle, S. Kaskel, *Chemical Society Reviews* 36 (2007) 1454.
- [7] S.U.S. Choi, *Journal of Heat Transfer* 131 (2009) 0331061.
- [8] A.W. Salamon, P. Courtney, I. Shuttler, Perkin Elmer, Online article.
- [9] Y. Yang, Dissertation Chemical & Materials Engineering University of Kentucky, Lexington, 2006.
- [10] G.H. Heilmair, Founders Award Lecture, National Academy of Engineering, Washington, D.C., 1992.
- [11] S. Chen, W. Liu, *Materials Research Bulletin* 36 (2001) 137.
- [12] S. Tarasov, A. Kolubaev, S. Belyaev, M. Lerner, F. Tepper, *Wear* 252 (2002) 63.
- [13] W. Yu, H. Xie, *Journal of Nanomaterials*, DOI:10.1155/2012/435873, 2012.
- [14] F.E. Lockwood, Z.G. Zhang, T.R. Forbus, S.U.S. Choi, Y. Yang, E.A. Grulke, SAE Paper 2005-01-1929 (2005).
- [15] Y. Hwang, H.S. Park, J.K. Lee, W.H. Jung, *Current Applied Physics* 6/Supplement 1 (2006) e67.
- [16] Y. Li, J. Zhou, S. Tung, E. Schneider, S. Xi, *Powder Technology* 196/2 (2009) 89.
- [17] L. Bergstrom, *Advances in Colloid and Interface Science* 70 (1997) 125.
- [18] L. Chen, H. Xie, Y. Li, W. Yu, *Thermochemica Acta* 477/1-2 (2008) 21.
- [19] J.A. Eastman, S.U.S. Choi, S. Li, W. Yu, L.J. Thompson, *Applied Physics Letters* 78/6 (2001) 718.
- [20] C.H. Lo, T.T. Tsung, L.C. Chen, *Journal of Crystal Growth* 277/1-4 (2005) 636.
- [21] H.T. Zhu, Y.S. Lin, Y.S. Yin, *Journal of Colloid and Interface Science* 277/1 (2004) 100.
- [22] H. Bonnemant, S.S. Botha, B. Bladergroen, V.M. Linkov, *Applied Organometallic Chemistry* 19/6 (2005) 768.

- [23] W. Yu, H. Xie, X. Wang, X. Wang, *Nanoscale Research Letters* 6 (2011) 47.
- [24] X. Yang, Z.H. Liu, *Nanoscale Research Letters* 5/8 (2010) 1324.
- [25] I.M. Joni, A. Purwanto, F. Iskandar, K. Okuyama, *Industrial & Engineering Chemistry Research* 48/15 (2009) 6916.
- [26] E. Tang, G. Cheng, X. Ma, X. Pang, Q. Zhao, *Applied Surface Science* 252/14 (2006) 5227.
- [27] L. Chen, H. Xie, *Thermochemica Acta* 497/1-2 (2010) 67.
- [28] X. Li, D. Zhu, X. Wang, *Journal of Colloid and Interface Science* 310/2 (2007) 456.
- [29] A.K. Singh, V.S. Raykar, *Colloid and Polymer Science* 286/14-15 (2008) 1667.
- [30] X.J. Wang, X. Li, S. Yang, *Energy and Fuels* 23/5 (2009) 2684.
- [31] D. Zhu, X. Li, N. Wang, J. Gao, H. Li, *Current Applied Physics* 9/1 (2009) 131.
- [32] Y. Hwang, J.K. Lee, C.H. Lee, *Thermochemica Acta* 455/1-2 (2007) 70.
- [33] K. Geng, Doctoral dissertation, Chemical & Materials Engineering, University of Kentucky, Lexington, 2006.
- [34] T. Druffel, K. Geng, E. Grulke, *Nanotechnology* 17/14 (2006) 3584.
- [35] T. Druffel, N. Mandzy, M. Sunkara, E. Grulke, *Small* 4/4 (2008) 459.
- [36] H.J. Glasel, E. Hartmann, *Nuclear Instruments & Methods in Physics Research, Section B* 151/1-4 (1999).
- [37] Y.-H. Yu, J.-M. Yeh, *Journal of Applied Polymer Science* 92/6 (2004) 3573.
- [38] G.S. Lyn, S.H. Park, *Kongop Hwahak* 16/2 (2005) 212.
- [39] H. Cox, T. Dear, *Proceedings of 4th World Congress: Nanocomposites* (San Francisco, CA) (2004).
- [40] J.R. Schneider, D.D. Ragan, U.S. Pat. Appl. Publ. (USA) (2002) 13 pp.
- [41] K. Gall, M.L. Dunn, *Acta Materialia* 50/20 (2002) 5115.
- [42] Y. Wei, D. Jin, *Journal of Applied Polymer Science* 70/9 (1998) 1689.
- [43] M. Menning, P.W. Oliveira, *Thin Solid Films* 351/1-2 (1999) 99.
- [44] N. Kambe, Y.D. Blum, *Proceeding of SPIE-The International Society for Engineering* 4905 (2002) 1.
- [45] D.M. Pirro, A.A. Wessol, *Lubrication Fundamentals*, Marcel Dekker, New York, 2001.
- [46] A. Voelkel, J. Fall, *Journal of synthetic lubrication* 24 (2007) 91.
- [47] J. Hashizume, A. Teramoto, H. Fujita, *J. Polym. Sci., Polym. Phys. Ed.* 19 (1981).

- [48] G.V. Schulz, B.Z. Jirgensons, *Phys. Chem.* B46 (1940).
- [49] M. Kurata, *Thermodynamics of Polymer Solutions: Chapter 2*, Harwood Academic Publishers, New York, 1982.
- [50] L.A. Kleintjens, R. Koningsveld, W.H. Stockmayer, *Polym. J.* 8 (1976).
- [51] R. Spahl, G. Luft, *Angew. Makromol. Chem.* 115 (1982).
- [52] S.K. Kumar, S.P. Chhabria, R.C. Reidland, U.W. Suter, *Macromolecules* 20 (1987) 2550.
- [53] G.V. Schulz, B.Z. Jirgensons, *Phys Chem B* 46 (1940) 105.
- [54] R. Koningsveld, W.H. Stockmayer, J.W. Kennedy, L.A. Kleintjens, *Macromolecules* 7 (1974) 73.
- [55] J.A.P. Coutinho, Daridon, J.L., *Petroleum Science and Technology* 23 (2005) 1113.
- [56] R. Koningsveld, A.J. Staverman, *Journal of Polymer Science: Part A-2: Polymer Physics* 6/2 (1967) 305.
- [57] A.R. Imre, *Polymer Science* 21/2 (2003) 241.
- [58] W. Borchard, S. Frahn, V. Fischer, *Macromolecular Chem. Phys.* 195 (1994) 3311.
- [59] W. Yan, J.A. Gardella, T.D. Wood, *J Am Soc Mass Spectrom* 13 (2002) 914.
- [60] V. Narasimhan, D.R. Lloyd, C.M. Burns, *Journal of Applied Polymer Science* 23/3 (1979) 749
- [61] J. Chen, J.A. Gardella, *Applied Spectroscopy* 52/3 (1998) 361.
- [62] R.L. Shubkin, *Polyalphaolefins*, CRC: London, 1994.
- [63] R.L. Shubkin, M.S. Baylerian, A.R. Maler, *Ind. Eng. Chem. Prod. Res. Dev.* 19/1 (1980) 15.
- [64] Y. Wang, I. Teraoka, F.Y. Hansen, G.H. Peters, O. Hassager, *Macromolecules* 43 (2010).
- [65] R.H. Boyd, R.R. Chance, G. Ver Strate, *Macromolecules* 29 (1996) 1182.
- [66] A. Helminen, H. Korhonen, J.V. Seppala, *Polymer* 42 (2001) 3345.
- [67] J. Chmelik, P. Konecny, J. Planeta, Z. Zdrahal, J. Vegrosta, *Journal of High Resolution Chromatography* 23 (2000) 502.
- [68] J. Chmelik, J. Planeta, P. Rehulka, *Journal of Mass Spectrom* 36 (2001) 760.
- [69] X. Dong, A. Proctor, D.M. Hercules, *Macromolecules* 30 (1997) 63.
- [70] A.R. Chercoles, A.M.M. San, d.I.R. Jose Manuel, M. Gomez, *Analytical and Bioanalytical Chemistry* 395 (2009) 2081.
- [71] A. Tiwary, A.K. Nema, C.K. Das, S.K. Nema, *Thermochimica Acta* 417 (2004) 133.

- [72] N. Wright, M.J. Hunter, *Journal of American Chemical Society* 69 (1947) 803.
- [73] B. Bonavoglia, G. Storti, M. Morbidelli, *Macromolecules* 38 (2005) 5593.
- [74] B. Bonavoglia, G. Storti, M. Morbidelli, *Industrial & Engineering Chemistry Research* 45 (2006) 3335.
- [75] A. Van Heukelum, G.T. Barkema, M.W. Edelman, E. Van der Linder, E.H.A. De Hoog, R.H. Tromp, *Macromolecules* 36 (2003) 6662.
- [76] Y. Rao, *Particuology* 8/6 (2010) 549.
- [77] V. Kanniah, T.R. Forbus, S. Parker, E.A. Grulke, *Journal of Applied Polymer Science* 122 (2011) 2915.
- [78] E.J. Garboczi, K.A. Snyder, J.F. Douglas, M.F. Thorpe, *Physical Review E Statistical Physics: Plasmas, Fluids and related interdisciplinary topics* 52 (1995) 819.
- [79] G.I. Titelman, V. Gelman, S. Bron, R.L. Khalfin, Y. Cohen, H. Bianco-Peled, *Carbon* 43/3 (2005) 641.
- [80] C.K. Poh, S.H. Lim, H. Pan, J. Lin, J.Y. Lee, *Journal of Power Sources* 176 (2008) 70.
- [81] L. Jiang, L. Gao, *Carbon* 41 (2003) 2923.
- [82] O. Sneh, S.M. George, *Journal of Physical Chemistry* 99 (1995) 4639.
- [83] C. Beck, W. Hartl, R. Hempelmann, *Angewandte Chemie International Edition* 38 (1999) 1297.
- [84] T. Shimada, K. Aoki, Y. Shinoda, T. Nakamura, N. Tokunaga, S. Inagaki, T. Hayashi, *Journal of American Chemical Society* 125 (2003) 4688.
- [85] N. Huesing, U. Schubert, R. Bernhard, W. Kiefer, *Materials Research Society Symposium Proceedings*, vol. 435, 1996, p. 339.
- [86] C.A. Garcia-Gonzalez, J. Fraile, A. Lopez-Periago, C. Domingo, *Journal of Colloid and Interface Science* 338 (2009) 491.
- [87] Y. Li, F. Yang, X. Yang, *Analyst* 134 (2009) 2100.
- [88] G.K. Raghuraman, R. Dhamodharan, *MACRO 2004, International Conference on Polymers for Advanced Technologies*, 2004.
- [89] T. Masui, H. Hirai, N. Imanaka, G. Adachi, T. Sakata, H. Mori, *Journal of Material Science Letters* 21 (2002) 489.

- [90] C. Kotsmar, K.Y. Yoon, H. Yu, Y. Ryoo, J. Barth, S. Shao, M. Prodanovic, T.E. Milner, S.L. Bryant, C. Huh, K.P. Johnston, *Industrial & Engineering Chemistry Research* 49 (2010) 12435.
- [91] P.C. Hidber, T.J. Graule, L.J. Gauckler, *Journal of American Ceramic Society* 79 (1996) 1857.
- [92] S.H. Brewer, Glomm, W.R., M.C. Johnson, M.K. Knag, S. Franzen, *Langmuir* 21 (2005) 9303.
- [93] T.D. Shen, W.Q. Ge, K.Y. Wang, M.X. Quan, J.T. Wang, W.D. Wei, C.C. Koch, *Nanostructures Materials* 7 (1996) 393.
- [94] H.Q. Li, X.R. Zeng, H.P. Deng, *Journal of Applied Polymer Science* 118 (2010) 63.
- [95] T. Oh, *Japanese Journal of Applied Physics: Part 1* 45 (2006) 264.
- [96] B. Erdem, R.A. Hunsicker, G.W. Simmons, E.D. Sudol, V.L. Dimonie, M.S. El-Aasser, *Langmuir* 17 (2001) 2664.
- [97] G. Camino, S.M. Lokamin, M. Lazzari, *Polymer* 42 (2000) 2395.
- [98] M.A. van Drunen, R. Finsy, H.G. Merkus, B. Scarlett, G.M. van Rosmalen, *Journal of Crystal Growth* 134 (1993) 196.
- [99] A.N. Parikh, M.A. Schivley, E. Koo, K. Seshadri, D. Aurentz, K. Mueller, D.L. Allara, *Journal of American Chemical Society* 119 (1997) 3135.
- [100] H.M. Shang, Y. Wang, S.J. Limmer, T.P. Chou, K. Takahashi, G.Z. Cao, *Thin Solid Films* 472 (2005) 37.
- [101] S. Shibuichi, T. Yamamoto, T. Onda, K. Tsujii, *Journal of Colloid and Interface Science* 208/1 (1998) 287.
- [102] K. Tadanaga, J. Morinaga, A. Matsuda, T. Minami, *Chemistry of Materials* 12/3 (2000) 590.
- [103] A. Nakajima, *Journal of Ceramic Society of Japan* 112/10 (2004) 533.
- [104] T. Onda, S. Shibuichi, N. Satoh, K. Tsujii, *Langmuir* 12/9 (1996) 2125.
- [105] W. Huang, H. Huang, *Guangdong Huangong* 35/10 (2008) 46.
- [106] J. Kijlstra, K. Reihls, A. Klamt, *Colloids and Surfaces A: Physicochemical and Engineering Aspects* 206 (2002) 521.
- [107] P. Gould, *Materials Today - Elsevier* 6 (2003) 44.
- [108] S.H. Wu, *Polymer interface and adhesion*, Marcel Dekker, New York, 1982.
- [109] T.W. Kim, B. Bhushan, *Tribology Transactions* 50 (2007) 165.

- [110] H.J.H. Brouwers, *Physical review E* 74/3 (2006).
- [111] R.K. McGeary, *Journal of American Ceramic Society* 44 (1961) 513.
- [112] T. Young, *Phil. Trans. I* (1805) 84.
- [113] R.N. Wenzel, *J. Phys. Colloid Chem.* 53 (1949) 1466.
- [114] H.J. Lee, S. Michielsen, *Journal of Polymer Science: Part B: Polymer Physics* 45 (2007) 253.
- [115] T.S. Chow, *J. Phys.: Condens. Matter* 10 (1998) L445.
- [116] W.A. Zisman, *Advances in Chemistry Series, No 43* (1964).
- [117] C.-C. Lin, W.-L. Liu, C.-Y. Hsieh, *Journal of Applied Physics* 109 (2011) 014508.
- [118] H.M. Shang, Y. Wang, K. Takahashi, G.Z. Cao, *Journal of Material Science* 40 (2005) 3587.
- [119] C.C. Furnas, *Journal of Industrial Engineering Chemistry (Washington D.C.)* 23 (1931) 1052.
- [120] E.K.H. Li, P.D. Funkenbusch, *Materials Science and Engineering A157* (1992) 217.
- [121] H. Bouwmeester, I. Lynch, H.J.P. Marvin, K.A. Dawson, M. Berges, D. Braguer, *Nanotoxicology* 5/1 (2011) 1.
- [122] V.A. Hackley, Ferraris, C.F.,, *NIST Recommended Practice Guide: Special Publication 960-3, Washington, DC, 2001.*
- [123] A.L. Barabasi, H.E. Stanley, *Fractal concepts in surface growth, Cambridge University Press, 1995.*
- [124] N. Isabeta, B. Biscans, *Powder Technology* 203 (2010) 206.
- [125] U. Katznel, R. Bedrich, M. Stintz, R. Ketzmerick, T. Gottschalk-Gaudig, H. Barthel, *Part. Part. Syst. Charact.* 25 (2008) 9.
- [126] J. Hyeon-Lee, G. Beaucage, S.E. Pratsinis, S. Vemury, *Langmuir* 14/20 (1998) 5751.
- [127] E. Bugnicourt, J. Galy, J.F. Gerard, F. Boue, H. Barthel, *Polymer* 48/4 (2007) 949.
- [128] S.A. Khan, N.J. Zoeller, *J. Rheol.* 37/6 (1993) 1225.
- [129] L. Gmachowski, *Coll. Surf. A* 255 (2005) 105.
- [130] P. Gwaze, O. Schmid, H.J. Annegarn, M.O. Andreae, J. Huth, G. Helas, *Aerosol Science* 37 (2006) 820.
- [131] M.M. Huber, H. Klein, L. Ratke, *Part. Part. Syst. Charact.* 20 (2003) 379.
- [132] D.J. Hemker, C.W. Frank, *Macromolecules* 23/20 (1990) 4404.

- [133] Z. Zhou, B. Chu, *Journal of colloid and interface science* 143/2 (1991) 356.
- [134] H.F. Jelinek, E. Fernandez, *Journal of Neuroscience Methods* 81 (1998) 9.
- [135] T.G. Smith Jr, G.D. Lange, W.B. Marks, *Journal of Neuroscience Methods* 69 (1996) 123.
- [136] O. Heymans, J. Fissette, V. Pico, S. Blacher, D. Masset, F. Brouers, *Medical hypotheses* 54/3 (2000) 360.
- [137] T. Sungkaworn, W. Triampo, P. Nalakarn, D. Triampo, I.M. Tang, Y. Lenbury, P. Picha, *International journal of biological and life sciences* 2/1 (2007) 67.
- [138] V.K. Ivanov, O.S. Polezhaeva, G.P. Kopitsa, A.E. Baranchikov, Y. Tretyakov, D., *Inorganic materials* 44/3 (2007) 272.
- [139] B.B. Mandelbrot, *The fractal geometry of nature.*, Freeman, New york, 1983.
- [140] M. Lapuerta, F.J. Martos, G. Martin-Gonzalez, *Journal of colloid and interface science* 346/1 (2010) 23.
- [141] A. Karperien, *FracLac for Image J*, version 2.5, <http://rsb.info.nih.gov/ij/plugins/fraclac/FLHelp/Introduction.htm>, 1999.
- [142] T. Vicsek, *Fractal growth phenomena*, 2nd edition, World Scientific Publishing Co. Pvt. Ltd., 1992.
- [143] K.L. Cho, I.I. Liaw, A.H.-F. Wu, R.N. Lamb, *J. Phys. Chem. C* 114/25 (2010) 11228.
- [144] K.N. Ramakrishnan, *Journal of Material Science Letters* 19 (2000) 1077.
- [145] K. Foroutan-pour, P. Dutilleul, D.L. Smith, *Applied mathematics and computation* 105 (1999) 195.
- [146] B. Wang, P. Wu, R. Yokel, E. Grulke, (2011 (submitted)).
- [147] E. Allen, J. Henshaw, P. Smith, US DOE report (2001).
- [148] J.P. La Femina, *Pacific national laboratories report* 10763 (1995).

Vita

Name	Vinod Kanniah
Date of Birth	10 th November, 1982
Place of Birth	Madurai, TN, INDIA
B.Tech in Chemical Engineering	University of Madras, INDIA, 2004
M.S. in Chemical Engineering	Oklahoma State University, USA, 2006
Certification in Business Data Mining	Oklahoma State University, USA, 2006
Process Engineer Intern	Orchid Chem. & Pharm. Ltd. INDIA
Catalysis Research Intern	CSIR, INDIA
Research/ Teaching Assistant	Oklahoma State University, USA
Coatings Development Intern	Valvoline, Ashland, KY, USA
Research Assistant	University of Kentucky, USA

Peer reviewed journal publications (Ph.D. work)

1. 'Nanoparticle segregation in a single deposition polymer nanocomposite', *Vinod Kanniah*, Binghui Wang, Thad Druffel, Eric A. Grulke, manuscript, Thin Solid Films.
2. 'The effects of surface roughness on the haze for polymer nanocomposite films', *Vinod Kanniah*, Thad Druffel, Eric A. Grulke, under review, Thin Solid Films.
3. 'Fractal analysis as a complimentary technique for characterizing nanoparticle size distributions', *Vinod Kanniah*, Peng Wu, Natalia Mandzy, Eric A. Grulke, under review, Powder Technology.
4. 'Graphite functionalization for dispersion in two phase lubricant oligomer mixture', *Vinod Kanniah*, Binghui Wang, Ying Yang, Eric A. Grulke, Journal of Applied Polymer Science DOI:10.1002/app.35574.
5. 'Partition coefficients for a mixture of two lubricant oligomers', *Vinod Kanniah*, Reg T. Forbus, S. M. Parker, Eric A. Grulke, Journal of Applied Polymer Science, 2011, Vol. 122, No.5, pp. 2915-2925